POLITECNICO DI TORINO

DOCTORAL THESIS

Study of the characteristics of the NUMEN Project targets to optimize the energy resolution in the measurements of the Double Charge Exchange reactions cross section

---

Author:
Vittoria CAPIROSSI

Supervisor:
Prof. Felice IAZZI

No one believes a theory, except the theorist. Everyone believes an experiment -except the experimenter.

W. Beveridge

It is impossible to travel faster than light, and certainly not desirable, as one's hat keeps blowing off.

W. Allen

Abstract

One of the most interesting and still unknown topic of the modern Nuclear Physics is the neutrino's nature: this particle is the most elusive of the standard model, being the hardest one to detect because of its neutral charge and very light mass. For this reason, many experiments of the last decade have been designed to get information on the neutrinos masse and their intrinsic nature of Dirac or Majorana particles. Often these experiments join their efforts together in order to get complementary results. In this exciting context, the study of the Neutrinoless Double Beta Decay (NDBD) could shed light on the neutrino's nature: if neutrino is a Majorana particle, it is a particle and at the same time its own anti-particle. In this case, the two neutrinos produced in the double decay would annihilate, being not visible in the final state. This discovery could lead to a re-definition of one of the most important law of the Nuclear and Particle Physics, the conservation of the leptonic number.
Several underground experiments are setting upper limits to the NDBD decay rate, but the rarity of this decay calls for complementary researches. The Double Charge Exchange (DCE) reactions are good candidates, since they have many similarities with the NDBD: experimental measurements of DCE cross-sections could help in the determination of the Nuclear Matrix elements involved in the NDBD theory.
However, DCE reactions, even if surely more frequent than NDBD, are quite rare and, when studied by fixed-target experiments, require very intense ion beams.
The NUMEN project fits precisely in this context: using ion beams of tens of μA impinging on very special targets, the experiment can detect a large variety of DCE reactions. These targets must satisfy two strong constraints: on one side, they must be very thin, to fulfil the energy resolution requirements of the experiment, on the other side, they must be also heat resistant, to avoid the damaging due to the energy released by the intense beams.
These two main features make the NUMEN targets very innovative: a few hundreds of nanometers of the isotopic material, required to get a DCE reaction, are deposited on a substrate made of Highly Oriented Pyrolytic Graphite a few micrometers thick. Thanks to the high in-plane thermal conductivity of this special graphite, the heat produced by the beam crossing the target deposition can be quickly transferred through the substrate to a cooling system. The substrate and the target deposition have to be accurately characterized in thickness and uniformity, since these knowledges are crucial in the evaluation of the NUMEN overall energy resolution. Different analysis techniques can be used in a complementary manner, to get a 360° characterization of these very special targets.
The design, the production and the precise characterization of the first prototypes of these targets, together with the study of their energy resolution features, are the main topics of this Thesis.

Contents

List of Abbreviations

AFM	**A**tomic **F**orce **M**icroscopy
APT	**A**lpha **P**article **T**ransmission
DBD	**D**ouble **B**eta **D**ecay
DCE	**D**ouble **C**harge **E**xchange
DISAT	**Di**partimento di **S**cienza **A**pplicata e **T**ecnologia
DWBA	**D**istorded **W**ave **B**orn **A**pproximation
EDX	**E**nergy **D**ispersive **X**-ray
FESEM	**F**ield **E**mission **S**canning **E**lectron **M**icroscopy
FPD	**F**ocal **P**lane **D**etector
FRAISE	**FRA**gment **I**on **SE**parator
FWHM	**F**ull **W**idth **H**alf **M**aximum
HOPG	**H**ighly **O**riented **P**yrolytic **G**raphite
IBM	**I**nteracting **B**oson **M**odel
INFN	**I**stituto **N**azionale di **F**isica **N**ucleare
ISM	**I**nteracting **S**hell **M**odel
LNL	**L**aboratori **N**azionali di **L**egnaro
LNS	**L**aboratori **N**azionali del **S**ud
MAESTRO	**M**ultichannel **A**nalyzer **E**mulation **S**oftware
NDBD	**N**eutrinoless **D**ouble **B**eta **D**ecay
NME	**N**uclear **M**atrix **E**lement
NUMEN	**NU**clear **M**atrix **E**elements for **N**eutrinoless double beta decay
PON	**P**rogramma **O**perativo **N**azionale
PVD	**P**hysical **V**apor **D**eposition
QRPA	**Q**uasiparticle **R**andom **P**hase **A**pproximation
RBS	**R**utherford **B**acks**c**attering
SC	**S**uperconducting **C**yclotron
SCE	**S**ingle **C**harge **E**xchange
SEM	**S**canning **E**lectron **M**icroscopy
SRIM	**S**topping and **R**ange of **I**ons in **M**atter
TRIM	**T**ransport of **I**on in **M**atter

Chapter 1

Neutrinoless Double Beta Decay and Double Charge Exchanges

1.1 Neutrinoless Double Beta Decay: searching for the neutrino's nature

Neutrinos are the most elusive particles of the Standard Model. They have no electrical charge, so they are not subject to electromagnetic interaction; moreover, they are leptons, fact that excludes them from the strong nuclear interaction.
There are three different kinds of neutrinos, strictly related to the leptons of the Standard Model (e, μ and τ): the electronic neutrino ν_e, the muonic neutrino ν_μ and the tauonic neutrino ν_τ. [1]
Neutrinos detection is challenging also because of their very light mass. This is so small that for a moment it seemed (erroneously!) that they could reach speeds higher than the speed of light[1]. Today we know that they must have a non-zero mass to explain another very strange feature, the mass-oscillation, that was predicted by Bruno Pontecorvo [3] and experimentally verified in 1998 by the experiment Super-Kamiokande [4]. However, experimental direct mass measurements are far away to come: actually neutrino's scientific community is struggling to lower the upper mass limit.
For all these reasons neutrinos probably are the most fascinating and mysterious particles, and a large portion of the Particle Physics community is focusing on them. In the wide research aimed to study neutrinos, undoubdetly Neutrinoless Double Beta Decay ($0\nu\beta\beta$, from here shortened in NDBD) plays a crucial role.

1.1.1 The Neutrinoless Double Beta Decay

A Beta (β) decay is a type of radioactive decay where a nucleon changes its charge by one unity, with the emission of a *Beta particle* (electron or positron) and an (anti)neutrino. After a β-decay, the nucleus charge results changed and so also the atomic number, but the mass number remains unvaried.
There are two possible types of β-decay: in a β^+-decay one proton of a nucleus becomes a neutron, with the emission of a positron and a neutrino, while in a β^--decay one neutron of a nucleus becomes a proton, with the emission of an electron and an anti-neutrino. Formula 1.1 shows a β^+-decay, while formula 1.2 shows a β^--decay.

$$ {}^A_Z X \rightarrow {}^A_{Z-1} Y + e^+ + \nu_e \tag{1.1} $$

[1] See [2]: in an interview for the journal Il Giornale of the 22 September 2011, professor A. Zichichi, involved in the OPERA experiment, explained the new groundbreaking neutrinos time-of-flight measurements.

$$ {}^{A}_{Z}X \rightarrow {}^{A}_{Z+1}Y + e^- + \bar{\nu}_e \tag{1.2} $$

For some isotopes a single β-decay is not possible, being energetically forbidden, but two simultaneous beta decays are allowed.
A Double Beta Decay (DBD) is a process made of two simultaneous beta decays of the same type, each giving a (anti) neutrino, resulting in two (anti)neutrinos in the final state.

$$ {}^{A}_{Z}X \rightarrow {}^{A}_{Z-2}Y + 2e^+ + 2\nu_e \tag{1.3} $$

$$ {}^{A}_{Z}X \rightarrow {}^{A}_{Z+2}Y + 2e^- + 2\bar{\nu}_e \tag{1.4} $$

This event, represented in the two versions by the formulas 1.3 and 1.4, has been detected in 11 nuclei with half-lives between $10^{18} - 10^{24}$ years.
The theoretical extension of the Standard Model predicts that also the Neutrinoless Double Beta Decay is possible: it should consist of two simultaneous β-decays, whose complessive final state does not show any (anti)neutrinos. The two versions of NDBD are reported in formula 1.5 and 1.6.

$$ {}^{A}_{Z}X \rightarrow {}^{A}_{Z-2}Y + 2e^+ \tag{1.5} $$

$$ {}^{A}_{Z}X \rightarrow {}^{A}_{Z+2}Y + 2e^- \tag{1.6} $$

First of all, the most evident strangeness in these processes is that the leptonic number is not conserved. Taking into the account, for example, formula 1.5, we can see that in the initial state the leptonic number is 0, while in the final state is -2 because of the presence of the two positrons (and the absence of the two neutrinos, that would contribute with a $+2$ resulting in a total leptonic number equal to 0 as in the initial state).
The only way to make this final state possible is that the two (anti)neutrinos, each one coming as result of one of the two beta decays, can annihilate. It means that one of the two (anti)neutrinos acted as a (particle)anti-particle: if confirmed, neutrino would be particle and anti-particle at the same time, leading to the violation of the leptonic number conservation law. This feature, so far unseen in any particle of the Standard Model, would make neutrino a so-called *Majorana particle*.
The main obstacle in this groundbreaking research is that the final state of the NDBD is very hard to experimentally detect with certainty. Since neutrinos are very elusive particles, a failure to detect them can mean that no neutrinos are actually present, but also that the detector is not sensitive enough.

According to the NDBD theory, the half-life $T_{1/2}^{NDBD}$ of this decay can be factorized in three contributions:

$$ [T_{1/2}^{NDBD}]^{-1} = G_{NDBD}|M^{NDBD}|^2 f(m_i, U_{ei}) \tag{1.7} $$

where G_{NDBD} is the phase-space factor of the decay, M^{NDBD} is the nuclear matrix element and $f(m_i, U_{ei})$ is the squared modulus of the effective Majorana mass of the electron neutrino. It can be calculated in the framework of light Majorana neutrino exchange, using the Pontecorvo-Maki-Nakagawa-Sakata matrix elements, through the relation:

$$ f(m_i, U_{e,i}) \equiv \left| \sum_i m_i U_{e,i} \right|^2 \tag{1.8} $$

The most interesting and unknown factor is $f(m_i, U_{ei})$, that contains the neutrino masses m_i and their mixing coefficients U_{ei}. The goal of the NDBD research is to access to the neutrinos masses (contained in $f(m_i, U_{ei})$) through the precise evaluation of the other three terms present in the equation ($T_{1/2}^{NDBD}$, G_{NDBD} and $|M^{NDBD}|^2$).
These other terms can be, in principle, experimentally and theoretically evaluated. $[T_{1/2}^{NDBD}]^{-1}$ and G_{NDBD} are the most approachable ones. The measurements of the NDBD decay rate can supply the value of the half-life, while the factor G_{NDBD} is calculated with high precision, taking into account several effects, as distortion of the final wave function by the Coulomb field of the daughter nucleus, calculation of the electron wave function with the relativistic quantum number $(l-j)(2j+1)$, screening of the atomic electrons and distortion due to the influence of the nuclear structure [5].
The term $|M^{NDBD}|$ represents the Nuclear Matrix Elements (NME) and can be calculated as:

$$|M^{NDBD}|^2 = | < \phi_f | O^{0\nu\beta\beta} | \phi_i > |^2 \tag{1.9}$$

where ϕ_i represents the initial state wavefunction, ϕ_f is the final state wavefunction and $O^{0\nu\beta\beta}$ is the NDBD operator. The determination of $|M^{NDBD}|$ nowadays is based on different theoretical models, as Interacting Shell Model (ISM), Interacting Boson Model (IBM) [6] or Quasiparticle Random Phase Approximation (QRPA) [7]. This large abundance of models, however, does not give a unique answer, mostly because of a lack of experimental constraints.
Despite all the difficulties, if observed, this decay not only would allow a precise mass measurement, but it also would prove that neutrinos are their own anti-particles, feature unseen in any other particle of the Standard Model. The Majorana nature of neutrinos would allow the violation of the conservation of the leptonic number, that is one of the fundamental laws of Nuclear and Particle Physics so far. It's clear that the removal of this milestone would bring to a re-definition of the Standard Model as we know it, falling in the so-called *Physics beyond the Standard Model*.

1.1.2 The NDBD experimental research

The difficulty in the neutrino detection and the crucial importance of the NDBD led many international collaborations of scientists to design a large variety of experiments, most of them based underground to be shielded against all the other particles from cosmic radiation (less penetrating than neutrinos[2]). Their experimental apparatuses are based on large containers filled with tons of sensitive material, that acts like active target where neutrinos are supposed to (sooner or later) interact and give some signals. These containers are surrounded by wide sets of detectors, ready to measure these rare neutrinos' signals.
A typical example of underground experiment aimed to study neutrinos is Super-Kamiokande, in Japan [8]. Kamiokande first proved the neutrino oscillation: based underground in the Mozumi Mine, is made of a tank full of 50000 tons of ultrapure water, ready to be crossed by atmosferic neutrinos. When a neutrino enters in the tank, interacts with electrons and nuclei of the material. These charged and fast particles undergo the Cherenkov effect: the light is then measured by a system of 13000 photomultiplier tubes that surround the water tank.
There is also a large portion of the neutrino experiments that is focused on the NDBD

[2]Since neutrinos do not interact easily with the matter, they do not lose much energy. For this reason, they are very penetrating particles.

research. Among many others, this is the case of two of the underground experiments in Gran-Sasso laboratories of Istituto Nazionale di Fisica Nucleare (INFN), GERDA [9] and CUORE [10].
GERDA is the acronym for GERmanium Detector Array: the heart of the experiment is a set of ultrapure Germanium detectors, enriched with the isotope ^{76}Ge, that acts as NDBD "generator" and detector at the same time. To be shielded by cosmic radiations, the Germanium detectors are immersed in a 6m$\times$4m cryostat full of liquid Argon, further contained in a bigger water cistern. According to the theory, the time necessary to halve the initial amount of ^{76}Ge by NDBD is one billion of millions of the age of the Universe. This means that the collected statistics is meant to be very low: the estimated number of detected NDBD events is less than one for year for kg of the detector material [11].
The Cryogenic Underground Observatory for Rare Events experiment, shortened to CUORE, is based on the same idea of NDBD generator/detector of GERDA, but the ^{130}Te enriched Tellurium detectors are inserted in the largest cryostat ever built, 10 tons heavy. The Tellurium detectors are kept at 10 mK by a very complex system of gradual cooling. When a NDBD happens, it results in a small temperature increasing of the Tellurium crystal, promptly detected. The detectors are moreover shielded from the environment radiation by a big covering made of Lead. CUORE is supposed to achieve an exclusion sensitivity of the order of 10^{26} years for the half-life of $0\nu\beta\beta$ decay (lower limit), corresponding to a sensitivity to the Majorana mass of neutrino around $40 - 100$ meV [12].
From all these examples it's clear that a neutrino experiment is very ambitious in terms of experimental complexity, peculiar requirements for the surrounding environment and time duration to get a large enough statistics. The difficulty in this type of research is intrinsic in the ambitious direct neutrino detection, and pushes to search for other complementary measurements to get information on the two main unknowns, the neutrino mass and the nuclear transition matrix elements. Other alternative roads have been explored with the study of other types of reactions that do not necessarily involve direct neutrino detection.
For example, many experiments are aimed to help in the NDBD research through the evaluation of the terms of factorization of the NDBD half-life. This is the case of the NUMEN (NUclear Matrix Elements for Neutrinoless) Project that, experimentally measuring cross-sections of Double Charge Exchange reactions, gives useful information for the determination of the NDBD NME.

1.2 Charge Exchange reactions

Charge Exchange reactions are off-shell processes[3], ruled by strong force [13]. This type of reaction requires two particles, one as charge-exchange sink and the other as charge-exchange source. The charge is passed through virtual mesons as rho mesons or pions.
A Double Charge Exchange (DCE) reaction is a beam-target process where two protons (neutrons) of the target nucleus are converted in two neutrons (protons), resulting in a final charge change of the target nucleus equal to ∓ 2. For the charge

[3] An *off-shell process* is a reaction mediated by a *virtual* (or *off-shell*) particle. While a *on-shell particle* has a real, constant and non-zero mass, according to the energy-impulse relativistic relation $E_1^2 = \sqrt{p_i^2 + m_i^2}$, an off-shell particle does not answer to this law. Indeed its mass is not a-priori defined and constant since it is a temporary manifestation of the quantistic field of which the particle is the quantum.

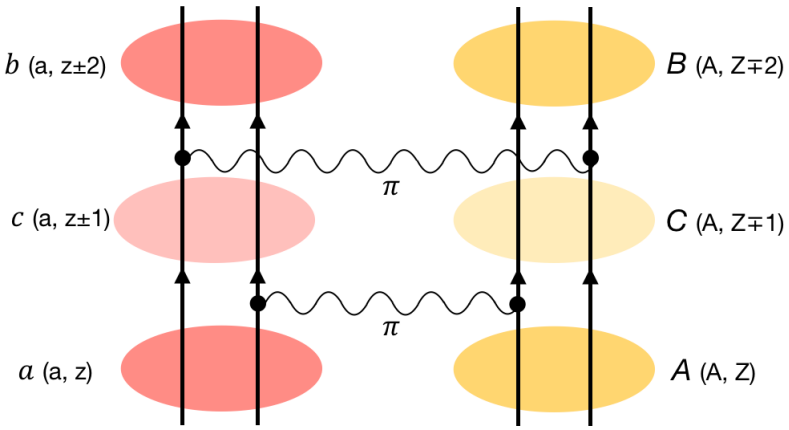

FIGURE 1.1: Graphical representation of a two-step Double Charge Exchange reaction, made of two consecutive SCE. The wavy lines represent the exchanged mesons (pions) between the two nucleons. c and C represent the intermediate charge states of the two nucleons.

conservation, the projectile nucleus has the opposite charge change, equal to ± 2.
Focusing on the process of charge exchange, a DCE reaction can be assumed, at its leading order, as a two-steps process, as a Double Beta Decay. It means that the main process, the DCE, is composed of two consecutive, equal and independent processes, each one responsible of a charge change equal to one unity. This "simpler" process is called Single Charge Exchange (SCE).
Each of the two SCE processes is induced by one-body operators on the two involved nuclei. Two consecutive SCE contribute to the DCE, resulting in a final charge exchange equal to two unities; this process can be considered a two-steps one-body DCE reaction. In this prospective, the DCE is similar to a DBD, where two consecutive and independent beta decays occur one by one.
Figure 1.1 shows a schematic view of a DCE process: two nucleons of the projectile nucleus (the left one) exchange two consecutive pions with two nucleons of the target nucleus (the right one). According to the charge of the two pions, that must be equal to get a double charge exchange, the final charge of the projectile nucleus is changed by two units, keeping the mass number unchanged.
According to another theoretical point of view, the DCE mechanism can be considered as the result of two dependent charge exchanges. The two SCE, mediated by the neutral mesons exchanged between the two pairs of nucleons of target and projectile, are now dependent from each other. In this scenario, the DCE proceeds as a one-step reaction, where a correlated pair of nucleons of the first nucleus changes its total charge of two units through the emission of a pair of virtual charged mesons. These two mesons are captured by the second nucleus, that undergoes a charge exchange of two units too.
This theory has never been considered so far, but it would open a brand new prospective. Indeed, this eventuality would strictly connect DCE reactions and NDBD: in the latter, the two nucleons undergoing beta decay are linked through the pair of Majorana's (anti)neutrinos, being dependent from each other.
To exhaustively study the DCE reaction mechanism, so far not yet completely understood, the SCE reactions, ruled by a well established theory, will be considered in the next section.

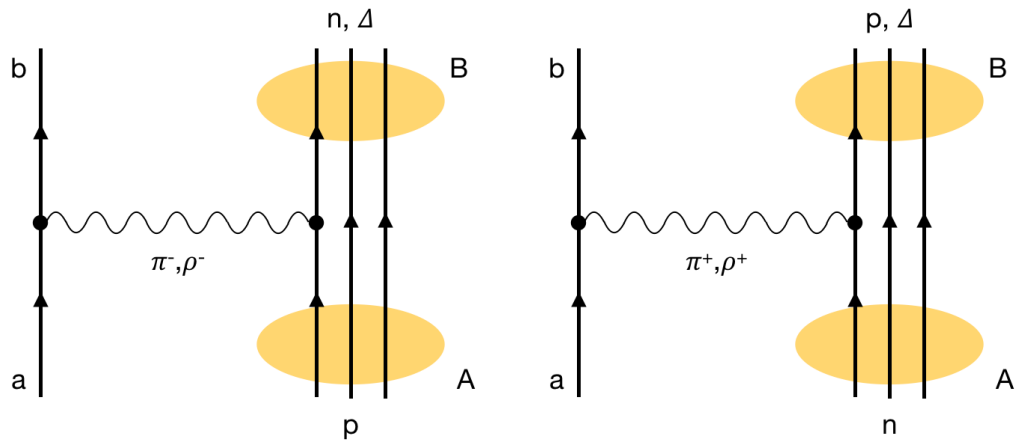

FIGURE 1.2: Graphical representation of Single Charge Exchange reactions (p,n)type (left) and (n,p)type (right). The wavy line represents the exchanged meson between the two nucleons, while the straight ones represent the nucleons.

1.2.1 Single Charge Exchange reactions

A Single Charge Exchange reaction is a beam-target process where a proton(neutron) of the target nucleus is converted in a neutron(proton), resulting in a final charge change of the target nucleus equal to ∓ 1. For the charge conservation, the projectile nucleus has the opposite charge change, equal to ± 1. Since the number of nucleons in the projectile nucleus and in the target one remains unchanged, the mass number is unvaried by the reaction.
Equations 1.10 show the scheme of the two possible SCE processes. A_P and Z_P are the mass number and the atomic number of the projectile nucleus, while A_T and Z_T are the same quantities but related to the target nucleus.

$$\begin{aligned}(A_P, Z_P) + (A_T, Z_T) &\rightarrow (A_P, Z_P - 1) + (A_T, Z_T + 1) \\ (A_P, Z_P) + (A_T, Z_T) &\rightarrow (A_P, Z_P + 1) + (A_T, Z_T - 1)\end{aligned} \tag{1.10}$$

The charge is exchanged by means of virtual charged mesons as pions (π) and rho mesons (ρ). Figure 1.2 is a graphical representation of the two types of SCE corresponding to hadronic interactions. From the theoretical point of view, SCE reactions are usually evaluated by the Distorted-Wave Born Approximation (DWBA) methods together with inputs from microscopic nuclear structure theory. Also calculations based on ISM and QRPA are largely used.
As previously mentioned, the SCE event is the key ingredient to get a DCE process.

Competing reaction channels (SCE)

A *direct* SCE is a collisional process, mediated by the exchange of a meson, resulting in a final charge change equal to ± 1. The meson exchange is a one-step process, ruled by the isovector nucleon-nucleon interaction. This is the interesting type of reaction, since it can give information on NME of the beta decay.
Direct SCE is the most probable cause for trasferring charge between colliding nuclei at energies above Coulomb barrier [20], but SCE can also occur at higher order.
Indeed, the same final result can be obtained also by two sequential and independent exchanges of nucleons, in a second-order charge exchange reaction. For example, the projectile nucleus can give a neutron to the target nucleus, and then it can receive a

proton. This is a sequential proton(neutron)-pickup neutron(proton)-stripping process. Obviously this is not a direct SCE reaction, but it is a *multi-nucleon transfer* mechanism made of two steps, each one ruled by the theory of a one-nucleon transfer
The two-step mechanism depends on the nucleon-nucleus mean field potential, instead of the nucleon-nucleon interaction which is the basis of the direct SCE.
The direct SCE, that is a competing channel, is more important in a collision between heavy ions, and must be accurately taken into account. By choosing a proper combination of projectile-target nuclei and an energy range in which the direct process dominates, this parasite branch can be minimized [21]. This tuning of the experimental conditions has been largely investigated in the past, coming to the general conclusion that the multi-nucleon transfer channel can be minimized increasing the energy far above the Coulomb barrier [22] [23] [24].
Moreover, as any other direct nuclear reaction, the cross section of DCE reactions depends on nuclear structure dynamics: also this topic requires a specific evaluation.
There is a key difference between an SCE reaction involving light nuclei and an SCE reaction involving heavy ions. When moving to heavier nuclei, their complex many-bodies nature must be carefully considered; the SCE reactions will be localized in the nuclear surfaces of the colliding systems, because of the strong overlapping of the nuclei wave functions when the two nuclei collide.

1.2.2 Double Charge Exchange reactions

A DCE reaction is a beam-target process where two protons(neutrons) of the target nucleus are converted in two neutrons(protons), resulting in a final charge change of the target nucleus equal to ∓ 2. For the charge conservation, the projectile nucleus has the opposite charge change, equal to ± 2. Since the number of nucleons in the projectile nucleus and in the target one remains unchanged, the mass number is unvaried by the reaction.
Equations 1.11 show the schematic DCE processes of charge exchange, where A_P and Z_P are mass number and atomic number of the projectile nucleus, while A_T and Z_T are the same quantities but related to the target nucleus.

$$\begin{aligned}(A_P, Z_P) + (A_T, Z_T) &\rightarrow (A_P, Z_P - 2) + (A_T, Z_T + 2)\\ (A_P, Z_P) + (A_T, Z_T) &\rightarrow (A_P, Z_P + 2) + (A_T, Z_T - 2)\end{aligned} \tag{1.11}$$

DCE and NDBD similarities

To study the parallelism between the charge exchange processes and the Neutrinoless Double β-decay, equations 1.12 show the schematic view of NDBD with β^+ and β^- decays. Now A_P and Z_P are respectively mass number and atomic number of the parent nucleus, and A_D, Z_D mass number and atomic number of the daughter nucleus.

$$\begin{aligned}(A_P, Z_P) &\rightarrow (A_D, Z_D - 2) + 2e^+\\ (A_P, Z_P) &\rightarrow (A_D, Z_D + 2) + 2e^-\end{aligned} \tag{1.12}$$

These equations point out the main contact point of the two processes: both of them are responsible of a charge change equal to ± 2 in the final target/daughter nucleus. Indeed the two processes, even if mediated by different interactions (DCE reactions are triggered by strong interaction, NDBD by the weak one), have a change of two units in the nuclear charge, leaving the mass number unvaried. The charge exchange is mediated by off-shell propagations of virtual states. This is not the only similarity:

many other common features led to the idea that a parallel study between the two processes can be done.
The most crucial feature is the coincidence of the wavefunctions of initial/final states of DCE and NDBD: the parent state of the NDBD is the same as the initial target nucleus state of DCE, while the daughter state of NDBD is the same as the DCE residual target nucleus state.
Another key aspect is the similarity between the transition operators of the two processes: indeed in both transition operators, short-range Fermi, Gamow-Teller and rank-2 tensor components are present [14].
Moreover, in both NDBD and DCE processes a large linear momentum is available in the virtual intermediate channel. This feature is unseen in other similar processes as DBD and SCE [15].
In addition, both NDBD and DCE events take place in the nuclear medium: it means that in medium effects will affect both, causing similar "quenching" effects.
All these aspects led to the founded hypothesis that the Nuclear Matrix elements of the DCE process could be similar to the Nuclear Matrix elements of NDBD.
It is of essential importance to understand how DCE's NMEs are connected to the NDBD's NMEs, investigating if they follow a smooth and thus controllable function of the projectile energy and of the mass of the system. In this context, the development of a complete and exhaustive theory of DCE reactions, factorized in a reaction part and a nuclear structure part, can significantly help the neutrino community: the physics description is complex for both, but DCE is, of course, experimentally more easily accessible.

Detecting a DCE

The scientific interest in the study of nuclear charge exchange reactions started with the discovery of the giant Gamow-Teller resonance[4] [16] and has continued until today.
In the '80s, intensive pion beams have been exploited to induce DCE reactions, not necessarily in the DBD context, to investigate different features of nuclear structure by studying the interaction of two nucleons [17] [18]. However, when the mesons research (main goal of the pion beams accelerators) declined, also the parallel DCE studies have been abandoned [19].
The possibility to use projectiles different from pions to get DCE reactions has been accurately evaluated, coming to the conclusion that also ions were suitable.
A large amount of data has been collected over the years, by using light ions (as ^3H or ^3He, using protons or neutrons as target) in the first instance. Nevertheless, these experiments are complex and for this reason many scientific collaborations started to use heavy ions to study charge exchange reactions. Indeed it was recognised that peripheral collisions between heavy ions could led to direct reactions, allowing spectroscopic studies as interesting as the ones obtained with light ions experiments.
Therefore, in the '80s and first years of '90s first pioneering experiments using heavy projectiles were performed with $(^{18}O,^{18}Ne)$, $(^{18}O,^{18}C)$ and $(^{14}C,^{14}O)$ at Los Alamos

[4]The Gamow-Teller resonance was identified in the '60s, by studying the neutrons energy spectra coming from (p,n) reactions on ^{51}V, ^{56}Fe, ^{59}Co nuclei. The peaks appearing in these plots led the scientists to the conclusion that a new type of nuclear excitations were discovered. The investigation in this type of resonances went on, since they allowed the deepening of problems of fundamental physics and astrophysics, such as properties of nuclear interactions, features of the beta decays of neutron-rich super-heavy nuclei, nucleosynthesis in the star explosions and solar and extragalactic neutrinos.

laboratories, ANU-Pelletron, Berkeley, NSCL-MSU and IPN-Orsay [25] [26] [27]. Because of the rarity of the DCE event, the small collected statistics was daunting and this type of research was abandoned.
In recent years, new experimental apparatuses allowed to start again the DCE research, relying on the capability to collect a larger statistics. This is the case of the experiments run at RIKEN and RCNP laboratories, that measured the cross-sections of different DCE reactions using a ^{8}He beam to study tetra-neutron systems [28] and ^{11}B and ^{12}C beams to explore the Double Gamow Teller resonance [29].
As previously described, the study of DCE reactions can be a useful tool to access to quantitative information on the NMEs of the NDBDs. For this reason, a particular propulsive thrust to the DCE research has been given by the increasing interest for the neutrino investigation and in the last years DCE reactions have been considered again interesting for the analogies with NDBD.
The laboratories of the Istituto Nazionale di Fisica Nucleare (INFN) based in Catania falls within this latter context. This very innovative facility, called Laboratori Nazionali del Sud (LNS), offers an optimal experimental apparatus to measure DCE cross-sections with high energy, angular and mass resolution, even at very forward angles, as explained in Chapter 2.
In 2015, the first pioneering measurements of cross-section of the DCE reaction $^{40}Ca(^{18}O,^{18}Ne)^{40}Ar$ using ^{18}O beam at 15 MeV/u, performed by the INFN-LNS community, were the starting point of a wide future research [30]. They showed the possibility to distinguish among different energy levels of the DCE products with good energy resolution: this new capability opened a window to the parallelism between DCE reactions and NDBD.

Competing reaction channels (DCE)

As for SCE reactions, also to interpret the DCE cross-section measurements the evaluation of the competing channels is necessary. The main role is played again by multi-nucleon transfer reactions, as in the SCE study, whose contribution appears developing the nucleon-nucleon potential until its 4^{th} order.
This two-steps process has the same final state as the DCE reaction, but it is made by two consecutive and independent charge exchanges. These double-SCE reactions recall DBD, where the two beta decays have not relations from one another. Equations 1.13 and 1.14 show two possible paths through which two consecutive multi-nucleon exchange processes can simulate the DCE $^{116}Cd(^{20}Ne,^{20}O)^{116}Sn$; the first one is a $(2p+2n)$ exchange, while the second is a $(2n+2p)$ exchange.

$$^{20}Ne +^{116} Cd \rightarrow^{18} O +^{118} Sn \rightarrow^{20} O +^{116} Sn \tag{1.13}$$

$$^{20}Ne +^{116} Cd \rightarrow^{22} Ne +^{114} Cd \rightarrow^{20} O +^{116} Sn \tag{1.14}$$

The evaluation of the multi-nucleon transfer reaction cross sections is paramount: they can be calculated within the DWBA approach, together with channel calculations performed thanks to the FRESCO code [31]. Different models, as microscopic IBM and ISM, can be used for these calculations and compared, giving a quite complete and coherent evaluation [32] [33].
Recent calculations of the transition matrix elements for heavy and medium nuclei performed with microscopic IBM have been also exploited for the nuclear matrix elements of NDBD [34]. From these studies, the multi-nucleon transfer cross sections result to be around $10^{-4} - 10^{-3}$nb [35], far from saturating the measured total cross

section, that is of the order of nb. This points out that the direct DCE represents the main contribution.
In the experimental conditions of the INFN-LNS experiments, the contribution of these reactions is less than 1%, as shown in [30].
The NUMEN Project, based at INFN-LNS laboratories, is aimed to measure with high accuracy the DCE reactions cross-sections. The following chapter will describe in details the Experiment.

Chapter 2

The NUclear Matrix Elements for Neutrinoless double-β decay Project

The NUclear Matrix Elements for Neutrinoless (NUMEN) double-β decay Project is conceived as a long-range time research to study many candidate systems for NDBD. It aims to put experimental constraints to the Nuclear Matrix Elements involved in the Neutrinoless Double Beta Decay by measuring the Double Charge Exchange reactions cross-sections with high energy and angular resolution. In particular, the most ambitious goal is to understand if the DCE matrix elements are connected to NDBD matrix elements as a smooth (and therefore that can be easily investigated) function of the projectile energy and of the system mass.
The experiments foreseen by the Project will be performed in the Laboratori Nazionali del Sud of the Istituto Nazionale di Fisica Nucleare. The LNS-INFN laboratories provide accelerated heavy-ion beams by using the K800 Superconducting Cyclotron; the MAGNEX large acceptance magnetic spectrometer is tasked with the ejectile detection.
The following section will describe the actual facility.

2.1 The actual NUMEN experimental apparatus

The experimental facilities installed in INFN-LNS are mainly constituted by the the K800 Superconducting Cyclotron and the MAGNEX magnetic spectrometer.
The K800 Superconducting Cyclotron (SC) is a particles accelerator designed to accelerate charged nuclei of ^{18}O and ^{20}Ne up to energies in the range 10-80 MeV/u. It guarantees a high energy resolution (estimated at $\sim$1/1000 of the nominal energy) and low emittance ($\sim 2\pi$ mm mr[1])[36]. The main limit of the present SC is the low beam intensity that it can reach: to get a large enough statistics, very intense ion beams are required for the NUMEN future studies.
MAGNEX is a large acceptance magnetic spectrometer, with a vertical focusing quadrupole lens followed by a magnet that horizontally bends the crossing particles [37]. A rotating platform, appreciable in figure 2.1, allows the spectrometer to rotate in a range $(-20°, +90°)$ around the target axis. The scattering chamber, together with the quadrupole and the dipole, is located on the platform, as well as the whole detection system. The maximum accepted magnetic rigidity[2] is around 1.8 Tm: it corresponds

[1] The emittance of a beam is a feature of a beam that represents its average spread in the position-and-momentum phase space.

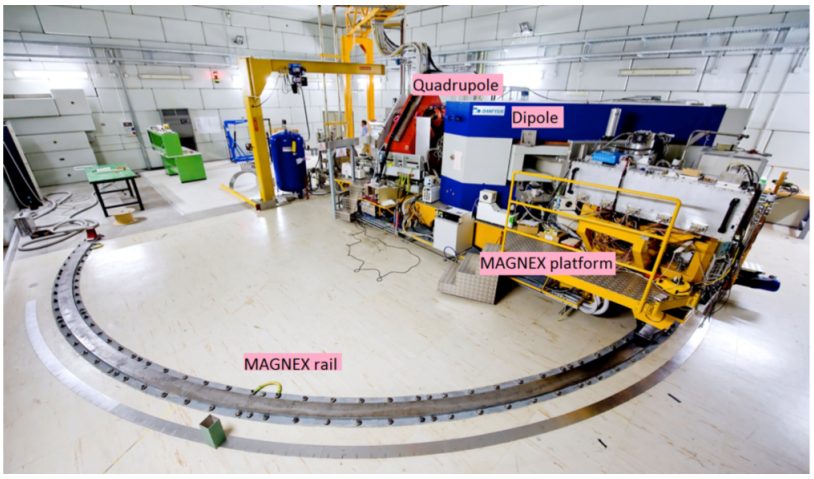

FIGURE 2.1: The present MAGNEX spectrometer moves on a circular rail; the quadrupole and the dipole are also visible.

to a maximum accepted energy of 46 MeV/u for the ^{18}O beam experiments and of 24 MeV/u for the ^{20}Ne beam experiments.
The most interesting and innovative feature of this spectrometer, in addition to the capability to measure at zero degrees, is the technique of trajectory reconstruction. It is able to solve with good precision the equations of motion of each crossing particle, correcting the aberrations induced by the large acceptance [38]. This complex technique allows to identify heavy ions with good mass resolution ($\Delta A/A \sim 1/160$), angle resolution ($\Delta\theta \sim 0.2°$) and energy resolution ($\Delta E/E \sim 1/1000$). The resolution on the momentum measurement is in the range $-14\% < \Delta p/p < +10\%$.
The detection of the reaction ejectiles is the task of the MAGNEX Focal Plane Detector (FPD). It is composed by two main detectors: a Gas Tracker and a Silicon Wall.
The gas detector consists of a set of wire-based drift chambers, with a pads segmentation to collect the induced signal. It measures the horizontal and vertical positions of the reaction ejectiles, together with the θ and ϕ angles of their trajectories. The whole gas detector covers an active volume of 1360 mm $\times$ 200 mm $\times$ 96 mm.
The Silicon Wall is made of 60 silicon pad detectors; it measures the residual energy of the reaction ejectiles. Each detector has an active area of 70mm $\times$ 50mm and is 500 μm thick. The pads are arranged in 20 columns and 3 rows.
The design and performances of the present FPD are exhaustively described in [44].
The mass and charge identification is performed by combining position and energy informations, reaching a 0.6% resolution in the mass and charge determination and a 2% resolution in the atomic number measurement. The resolution on the horizontal and vertical coordinates is 0.6 nm, while the resolution in the angular determination is around 5 mr. The overall energy resolution is 0.1%.
Even considering the good performances of the actual acceleration facility and of the MAGNEX FPD, an overall upgrade is necessary.
The FPD has limitations both in the gas tracker and in the silicons wall. The gas detectors have an intrinsic limitation in the tolerable rate of kHz of incident ions (and this will be a problem when the beam intensity will be increased), while the silicon detectors have a radiation tolerance of 10^9 particle/cm^2, that would be not suitable

[2]The magnetic rigidity R is a quantity that represents the bending of a charged particle in the magnetic field B. It is calculated as $R = B \times \rho$ where ρ is the curvature radius of the trajectory. It can be also evaluated through the formula $R = \frac{p}{q}$ where p is the relativistic momentum of the particle and q is its charge.

for the increased beam intensity phase. For all these reasons (and more), an overall upgrade of the LNS laboratories is foreseen.
The upcoming renewal of the LNS laboratories infrastructure, allowed by a wide Italian institutional finance in the context of the PON program, will promote an intense R&D activity on detectors and electronics hardware, on the system of the beam acceleration and in general on all the laboratories instrumentation. The NUMEN Project will profit and strongly contribute to this challenging overall upgrade.
The Project is divided in four phases, two of those being already completed.

2.2 The NUMEN four phases

Phase 1

This Phase run out in 2013, with the pilot experiment. During this year, the $^{40}Ca(^{18}O,^{18}Ne)^{40}Ar$ DCE reaction was measured at the LNS laboratories, together with the competing processes (two-proton and two-neutron transfers) and the SCE reactions. [30]
In this pioneering experiment, for the first time the DCE cross-sections have been measured in a wide range of transferred momenta, with high energy and angular resolution. The trend of the obtained angular cross-section showed an oscillating pattern, that has been successfully fitted by a n= 0 Bessel function[3]: this fact was encouraging, suggesting that a simple mechanism is dominant in the DCE reaction. The hypothesis of a two-step DCE, made of two independent SCE processes, has been considered to extract the DCE NMEs from the experimental cross-sections. Despite all the approximations of the model, the obtained results resulted comparable with the literature.
This first result was encouraging for the following researches, but some experimental constraints in the present set-up put limits to the extension of the pilot study to the so-called "hot cases", i.e. the nuclei candidate for the NDBD. To mention just two of the many difficulties, the NDBD candidate isotopes are heavier than ^{40}Ca, so the DCE cross-section will be reduced (due to an absorptive environment in the nucleus-nucleus collision). Moreover, the achieved energy resolution with the present set-up, typically about half MeV, is not always enough to separate the ground state from the excited ones in the ejectile nucleus[4]. These two reasons, added to many other considerations (see [35] for more details), led to the conclusion that the beam current has to be increased from some nA (intensity so far achievable with the present LNS cyclotron) to some tens of μA. The beam intensity increase involves not only an upgrade of the beam extraction and acceleration system, but also appropriate detectors

[3] The Bessel Functions, also noted as Cylinder Functions, are a set of mathematical functions derived around 1817 by the German astronomer Friedrich Wilhelm Bessel while studying the solutions of the Kepler's equations of planets motions. A Bessel function is the solution of the equation $x^2\frac{d^2y}{dx^2} + x\frac{dy}{dx} + (x^2 - n^2)y = 0$, where n is an integer number. The solutions have the form $J_n(x) = \frac{x^n}{2^n n!}\left[1 - \frac{x^2}{2(2n+2)} + \frac{x^4}{2\cdot4(2n+2)(2n+4)} - ...\right]$ and follow a damped periodic function. After Bessel's theoretical formulation, other scientists found out that many other physical phenomena can be described by Bessel functions. [39]

[4] DCE reaction products can exit the reaction in different energy levels, excited or ground state. For this reason, the energy spectrum of the DCE ejectile shows different peaks, each one resulted from a different combination of ejectile and target daughter energy levels. To study the cross-section of each DCE reaction, each peak must be clearly distinguished from the others: if the peaks are not enough separated in the energy spectrum, complementary measurements of the DCE reactions are required (as explained later).

and electronics able to face high particles rates. Moreover, the high irradiation of the experimental hall will ask for more stringent security procedures in the whole management of the experiments. Last but not least, also the entire target system has to be re-designed: this topic is the focus of this thesis and it will be described into the details later.

Phase 2

During the Phase 2 of the NUMEN Project, all the R&D studies for the necessary upgrades of the LNS laboratories infrastructures have been done, keeping the "old" facility still available to go on with the experiments. In this phase, experiments on a selected set of systems have been performed. This phase has been completed in the summer of 2020 and consisted of two classes of experiments, one measuring the $(^{18}O,^{18}Ne)$ DCE transition (corresponding to $\beta^+\beta^+$ decay) and one measuring the $(^{20}Ne,^{20}O)$ DCE transition (corresponding to $\beta^-\beta^-$ decay). Together with the DCE cross-sections, that here represent the more interesting physics, also the other reaction channels involving same beam and target have been studied.
The exploratory results obtained with the not-still-upgraded facility showed the challenging aspects of this type of experiments and established the best working conditions, even if the collected statistics was poor due to the low beam intensity. Among all the possible DCE candidate isotopes, the ones whose ejectile energy spectra show a good energy separation among the ground state and the other excited levels have been preferred. To facilitate these pioneering measurements, also the availability of thin uniform targets of isotope enriched materials has been taken into the account. The main features of these measurements with both ^{18}O and ^{20}Ne are briefly summarized in the following. The results are reported in references [40] and [41] respectively.

The ^{18}O experiments
In the context of the study of the DCE cross-sections of reactions obtained with the ^{18}O beam, also the reaction channels other than DCEs have been taken into the account. They are elastic and inelastic scattering $(^{18}O,^{18}O)$, two-proton pick-up reaction $(^{18}O,^{20}Ne)$, one-proton pick-up reaction $(^{18}O,^{19}F)$, two-neutron stripping reaction $(^{18}O,^{16}O)$ and one neutron stripping reaction $(^{18}O,^{17}O)$. These measurements have been performed in a wide angular range, thanks to the MAGNEX large angular acceptance. Moving the MAGNEX spectrometer in such a way that its optical axis is at $+3^\circ$ with respect to the beam axis, the detectable range was $-2^\circ < \theta_{lab} < +9^\circ$[5]. During the measurements foreseen for the NUMEN Phase 2, the beam was collected in a Faraday Cup, placed besides the FPD, to measure its total charge[6]. During the Phase 4 instead, when the beam intensity will be increased, due to radioprotection needs the beam will be transported outside the experimental hall and directed to a special beam dump.
Targets made of ^{116}Sn, ^{76}Se, ^{12}C and ^{48}Ti have been used with the ^{16}O beam at 16 AMeV to study $^{116}Sn(^{18}O,^{18}Ne)^{116}Cd$, $^{76}Se(^{18}O,^{18}Ne)^{76}Ge$, $^{12}C(^{18}O,^{18}Ne)^{12}Be$ and $^{48}Ti(^{18}O,^{18}Ne)^{48}Ca$ DCE transitions (and competing channels).

[5] θ_{lab} is the angle in the horizontal plane containing the beam axis; $\theta_{lab} = 0$ represents the beam axis.

[6] A Faraday cup is a conductive cup made of metal. When it is crossed by a charged particles beam, collects the charges and measures the beam current [42].

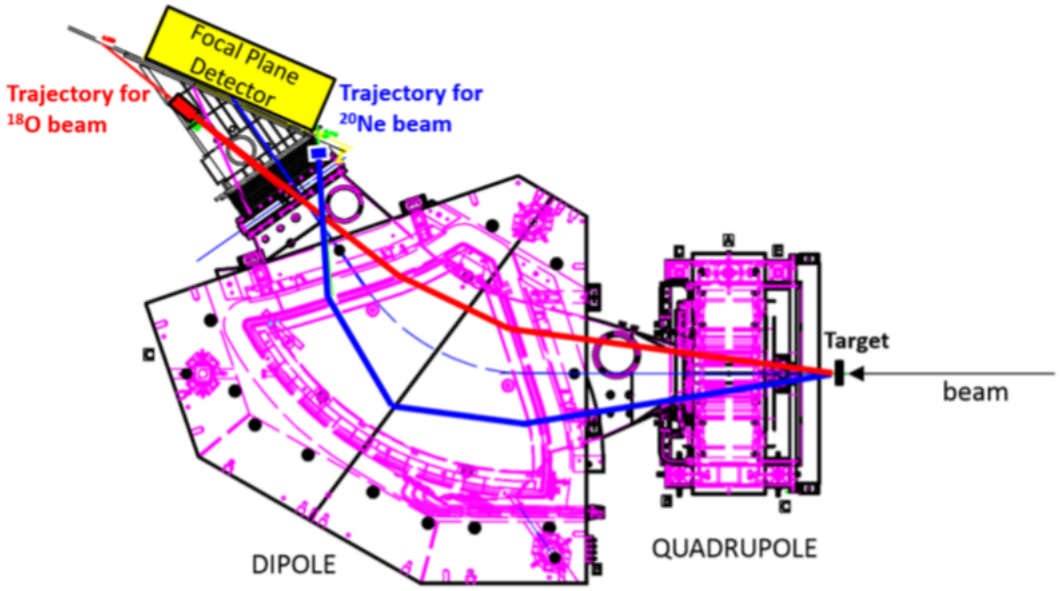

FIGURE 2.2: Drawing of the MAGNEX spectrometer with the typical trajectories of ^{18}O and ^{20}Ne beams .

The ^{20}Ne experiments

Concerning the measurements performed with the ^{20}Ne beam, the reaction channels of interest, in addition to the one related to charge exchange reactions, are elastic and inelastic scattering $(^{20}Ne,^{20}Ne)$, two-proton stripping reaction $(^{20}Ne,^{18}O)$, one-proton stripping reaction $(^{20}Ne,^{19}F)$, two-neutron pickup reaction $(^{20}Ne,^{22}Ne)$ and one-neutron pick-up reaction $(^{20}Ne,^{21}Ne)$.

Figure 2.2 shows the layout of the experimental hall with the MAGNEX spectrometer and the two main magnets. The red line represents the trajectory of the ^{18}O beam, while the blue one is the ^{20}Ne typical trajectory. Here magnetic rigidity of the incident beam is lower than the one of ^{18}O, so the beam will be more bent than the oxygen ejectiles. Placing the MAGNEX optical axis at $-3°$, the covered angular range is $-8° < \theta_{lab} < +3°$. The placing of the Faraday Cup in Phase 2 and the beam dump in Phase 4 are the same as in ^{18}O experiments.

The reactions explored with a 15 AMeV ^{20}Ne beam are $^{116}Cd(^{20}Ne,^{20}O)^{116}Sn$, $^{130}Te(^{20}Ne,^{20}O)^{130}Xe$ and $^{76}Ge(^{20}Ne,^{20}O)^{76}Se$.

Phase 3

This phase is foreseen for the disassembling of the old experimental set-up and the assembling of all the new upgraded hardware. Obviously, all the tests of the new detectors will be done in this phase, together with first trials of data taking. Phase 3 is expected to take a little more than 2 years to be completed.

During this phase, all the analysis of the previously collected data will go on.

Phase 4

Once the beam extraction and acceleration system will be upgraded, the beam current will reach some μA. The maximum beam intensity on the target will be around 10^{13} particle per second (pps) for both ^{18}O and ^{20}Ne.

Thanks to the increased beam intensity, the measurements can count on a larger

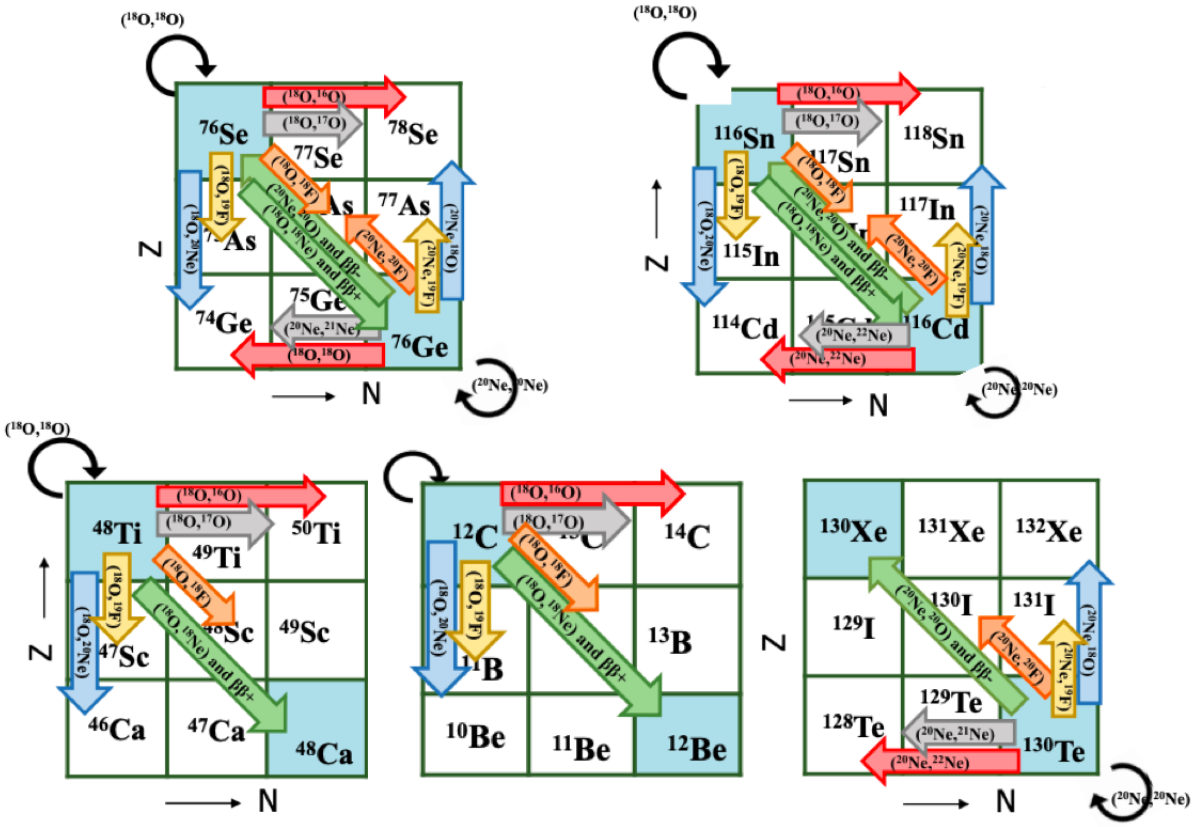

FIGURE 2.3: Scheme of the reaction channels studied during the NUMEN Phases 1 and 2.

statistics collected in a shorter time window. To have an example, let's consider the DCE transition $^{116}Cd(^{20}Ne,^{20}O)^{116}Sn$, that has been already explored during the Phase 2, collecting around 20 events of ground state-to-ground state DCE transitions in about 20 days of acquisition time (corresponding to a rate of around 1.5 events for day). The same reaction will be subject of study during the Phase 4, but with a higher beam intensity: in 2 days of data taking, it is reasonable to expect 10^4 DCE events, a statistics considerably larger than the one so far reachable.
Experimental campaigns after the facility upgrade will collect an integrate charge of hundreds of mC up to C. A large variety of $0\nu\beta\beta$ candidate isotopes will be used as targets, as ^{48}Ca, ^{76}Ge, ^{76}Se, ^{82}Se, ^{96}Zr, ^{100}Mo, ^{106}Cd, ^{110}Pd, ^{116}Cd, ^{110}Sn, ^{124}Sn, ^{128}Te, ^{130}Te, ^{136}Xe, ^{130}Xe, ^{148}Nd, ^{150}Nd, ^{154}Sm, ^{160}Gd and ^{198}Pt.
Figure 2.3 shows an overall scheme of the reaction channels studied during the NUMEN Phase 2: they will be re-measured with higher statistics in Phase 4.

Among all these possible reactions, precedence will be given to the ground state-to-ground state transitions where the ground state peak is well distinguishable from the ones related to excited states. In some DCE cases, the energy of the ground state peak is close to the energies related to the excited states peaks. In these cases, the sensitivity of the MAGNEX spectrometer is not sufficient to clearly distinguish the different peaks. For this reason, during the upgrade of Phase 3, a gamma detector surrounding the target will be added to the experimental apparatus [43]. This detector will measure the energy of the gamma rays coming from the de-excitation of the target daughter, when it is in an excited state after the DCE transition. This information will be helpful to distinguish different energy peaks in the spectra of the DCE reaction.

The experiments will be performed at different incident energies, to investigate the energy dependence of the DCE cross-sections.

2.3 The upgrades

As previously described, in correspondence of the NUMEN Phase 3, a comprehensive upgrade of the LNS facility is foreseen.
The main subject of this renewal is the superconducting cyclotron, but also the NUMEN detectors system will be improved.
The scattering chamber too will be changed with a more complex one, that will host the new target system.

2.3.1 Superconducting Cyclotron

The main change in the acceleration technology will involve the beam extraction system.
The actual SC can accelerate a large range of ions, from Hydrogen to Uranium, in an energy range spanning from 10 to 80 AMeV. Due to the SC compact geometry, the beam extraction efficiency is around $50 - 60$ %. Most of the beam particles hit the septum of the first electrostatic deflector, causing serious thermal issues. When the beam intensity will be increased, this beam extraction technique won't be workable. For this reason, the SC will be upgraded with a new beam line for the extraction by stripping[7]. By using a stripper foil, the trajectory of the beam in the magnetic field escapes from the cyclotron magnetic poles: the power lost inside the cyclotron will be at least one order of magnitude lower. [45]
The expected intensity of the extracted beam is around 50 μA, depending on the beam ion.
The new beam transport line will include the FRAgment Ion SEparator (FRAISE) line. FRAISE allows the production and separation of the radioactive ion beams, providing for a re-shape of the beam by cutting the beam halo. It can also reduce the energy spread (see [35] for more exhaustive explanations). Figure 2.4 shows a schematic view of the new layout of the LNS accelerator and beam lines.
The NUMEN-dedicated new beam line will consists of the three present quadrupoles, combined with two new dipoles and three new quadrupoles. Figure 2.5 shows the new MAGNEX experimental hall.
The new SC will deliver to the NUMEN scattering chamber a beam with a energy spread of 0.1%. This new line will fulfil the stringent NUMEN beam requirements, reaching a beam spot on the target with dimensions 1 mm on the x direction and 2.5 mm in y direction. The beam radial divergence will be 4 mrad.
Also the beam dump is object of R&D during the Phase 2. It has to handle a power up to 10 kW, released by a beam that can come from two different directions (according to each experiment and to the magnetic rigidity of the ejectile). For this reason, the MAGNEX room will be enlarged, to host the bigger new beam dump.

[7] In the stripping extraction, the beam is accelerated with a charge state between $(Z-5)$ and $(Z-2)$ and then it is fully stripped by crossing a stripper foil (e.g. a carbon foil).

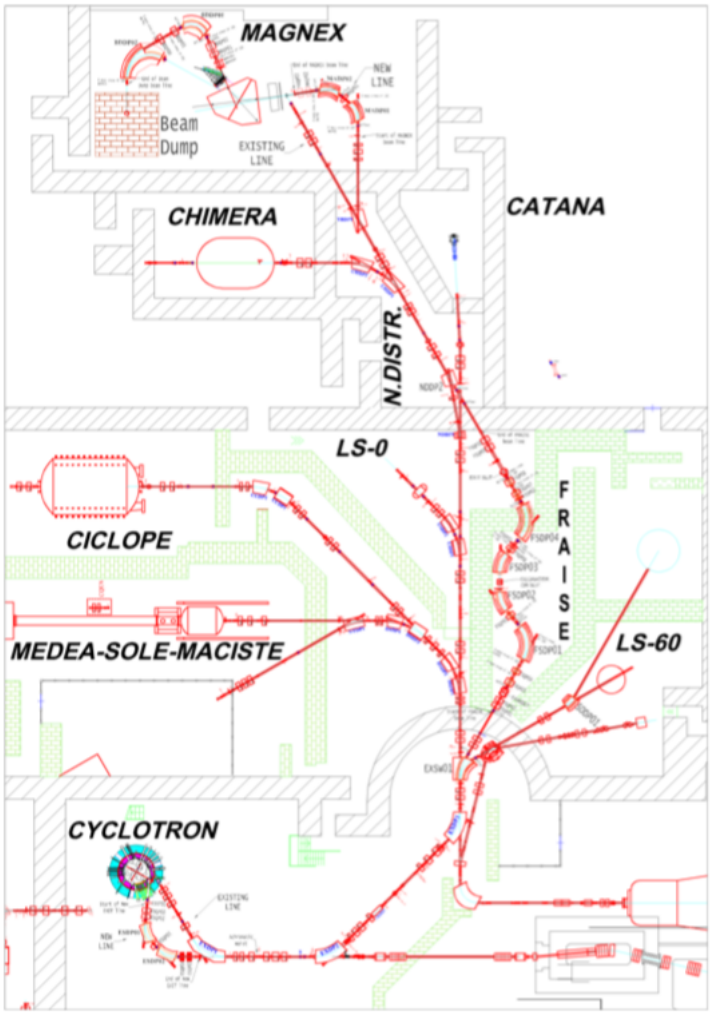

FIGURE 2.4: New layout of the LNS accelerator facility. The beam coming out from the cyclotron reaches the FRAISE line and then the MAGNEX experimental hall.

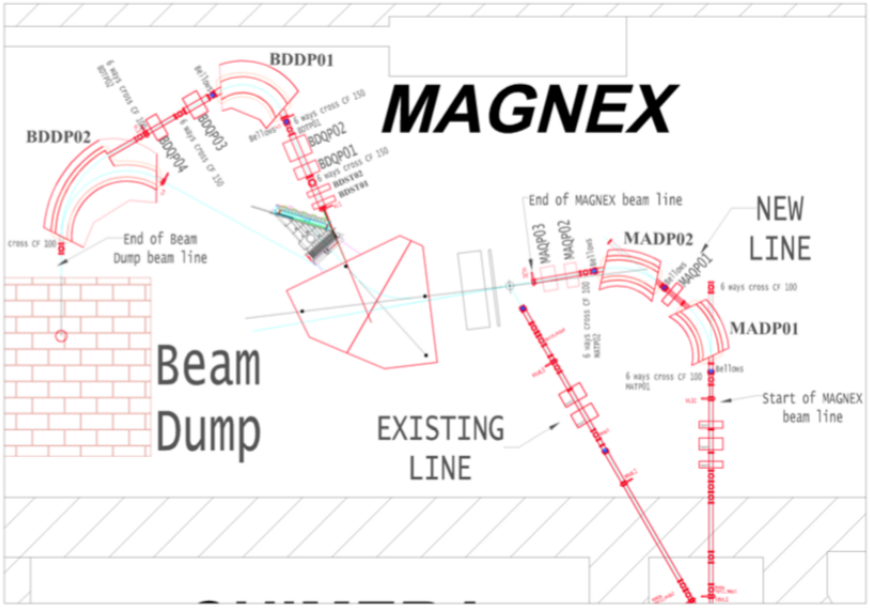

FIGURE 2.5: New layout of the MAGNEX experimental hall.

2.3.2 Integration of Mechanical Devices

Together with the enlargement of the MAGNEX experimental hall, all the new and upgraded components of the NUMEN apparatus will be integrated with the old ones.
The actual platform will be used also for the NUMEN Phase 4, thanks to a deep maintenance intervention. Also the quadrupole and the dipole on the platform can be used again, even if with an upgrade in the power supply and cooling system.
The scattering chamber will be changed with a more complex one, for two main reasons. The first one is related to a new detector, called G-NUMEN, that will be inserted around the target, as explained in the following. The second reason is the new target system, crucially different from the present one, that will need a dedicated cooling system and a side storage for the target exchange[8]. A target manipulator will be necessary, as described in [46].
Also the vacuum chamber of the Focal Plane Detector will be changed to host the upgraded detectors.
Finally, a new beam dump has been designed, to stop more intense ion beams. [35]

2.3.3 Focal Plane Detector

Both the gas tracker and the Silicon Wall will be upgraded.
The main disadvantage of the actual gas tracker [47] is the limit on the tolerable hit rate, that now is few kHz (due to the slow drift of the positive ions from the multiplication wires to the Frisch grid). This limited rate capability will not be acceptable during the NUMEN Phase 4 with more intense ion beams. For this reason, the new gas tracker will be faster than the actual one, being able to bear a hit rate around 100 kHz/cm. The new gas tracker is designed to be composed of 8 different modules, for a complessive active volume of $1122 \times 185 \times 108$ mm^3. The gas gap will be filled with isobutane at low pressure. The detector consists of a drift region between the multiplication plane and the cathode, a multiplication region based on the Multi-Thick GEM[9] technology and a segmented readout plane.
When a charged particle hits the Gas Tracker, it crosses a thin Mylar window and enters in the gas region. Crossing the gas gap, it loses energy and ionizes the gas molecules, creating a track of ionized atoms and primary electrons. Under a nearly uniform electric field, the electrons drifts with constant velocity crossing the drift region; their drift time is measured and the vertical position is deduced. Then, electrons reach the multiplication region, where they are accelerated by a stronger electric field present in the GEM foil. Then, the jet of electrons is directed to the segmented read-out electrode. The read-out electrode measures the horizontal position and the angles.
The spatial and angular resolution are expected to be 0.7 mm and 0.5° respectively, fulfilling the strict requirements fundamental for the accurate particle ray reconstruction. [35]
The technology of the new gas tracker will not provide an accurate particle identification and the walls of the NUMEN silicon detectors have to be upgraded to enhance the radiation tolerance, so a dedicated wall of telescope detectors has been designed

[8] It is reasonable to dedicate a following part to the details of the new scattering chamber, when the new target system will be illustrated.

[9] A Gas Electron Multiplier (GEM) detector is a type of gaseous ionization detector, where the most of the avalanche of the charge multiplication process occurs in the small holes tailored in a thin polymer sheet. [48]

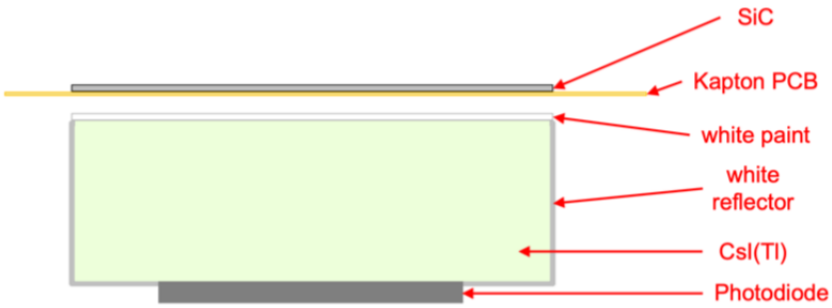

FIGURE 2.6: Layout of a NUMEN silicon telescope detector.

for the upgrade [49]. The technology is based on a telescope solution, where two detectors are involved. The particles cross the first, a thin detector where an energy loss signal is created by the particle, and stop into the second one, where the residual energy is collected. By cross-referencing the information coming from the two detectors, the atomic number Z of the particle can be deduced. Figure 2.6 shows the sketch of a detector cell. The chosen solution is focused on 820 telescopes of Silicon Carbide (SiC) used as thin detector and CsI(Tl) used as thicker detector, placed downstream the gaseous trackers. Each telescope has an active area of 1.5 cm $\times$ 1.5 cm, with a dead space of 0.2 mm. The SiC detector is only 100 μm thick, and the CsI(Tl) inorganic scintillator is coupled to a PIN 1 cm $\times$ 1 cm photodiode.
The overall silicon telescope fulfils the radiation hardness requirements for the NUMEN Phase 4, withstanding a counting rate of few tens of kHz/cm^2. The obtained resolution in the particle identification is $\Delta Z/Z \sim 1/24$ and $\Delta A/A \sim 1/47$.

2.3.4 G-NUMEN, the gamma array

The DCE reactions to be studied by the NUMEN project involve nuclei of different weights[35]. While for the lighter nuclei the energy resolution of the MAGNEX spectrometer is expected to be suitable to discriminate between the ground state and the first excited energy levels of the reaction products, this is not the case of the heavier nuclei. In such cases, an additional detector has been foreseen: the G-NUMEN detector.
It is a detector designed to measure the energy of the gamma rays emitted by deexcitation of the target daughter nucleus, if it comes out from the DCE event in an excited energy. This detector is then supposed to be placed in the region surrounding the target, since the gamma production is isotropic in space. The main problem of this type of detection is related to the very high radiation levels in the target region; in addition to gamma rays, also fast neutrons, electrons, light and heavy ions will be produced in the beam-target collisions. The emission rates of gamma foreseen in the NUMEN Phase 4 reach the order of magnitude of GHz. In addition to that, the neutron production is supposed to increase, and neutrons can demage the gamma detectors. For this reason, the detector has to be radiation robust: inorganic scintillators are the best solution, since they are quite tolerant to fast neutrons and gamma radiation.
Accurate software simulations with the GEANT4 Hadron therapy model [50] and different experimental tests with prototypes have been performed [51].
After dedicated studies, the choice related to the crystal material of the inorganic

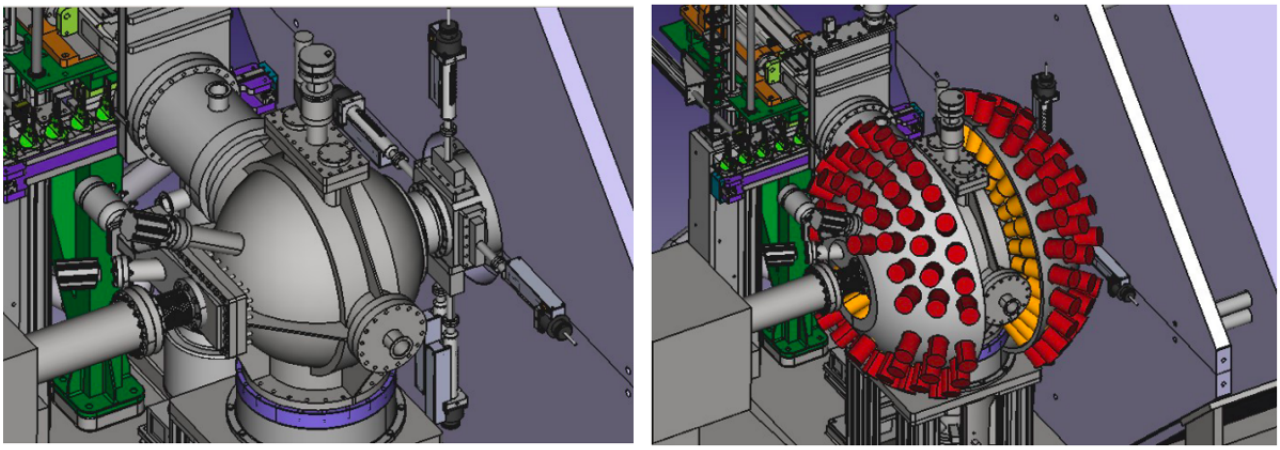

FIGURE 2.7: A sketch of the scattering chamber without (left) and with (right) the gamma array detector.

scintillator fell on $LaBr_3(Ce)$, able to face high particle rates preserving a suitable energy resolution.
Concerning the scintillators number and displacement, the available space for the gamma array is strictly connected to the scattering chamber structure and equipment (as vacuum pumps, beam entrance,...). Figure 2.7 shows a possible layout of the gamma array position. 139 scintillators are assembled in an half-dome, covering around the 20% of the total solid angle around the target. Each $LaBr_3$ detector is 50 mm long and has a diameter of 38 mm. The read-out will be demanded to standard photomultiplier tubes, which allows for the best timing and energy resolutions.
The described solution guarantees a total photopeak efficiency of $\sim$ 4% at 1 MeV. The energy resolution will be 2% and the time resolution less than 1 ns. The expected radiation tolerance should be higher than $10^{10} n/cm^2$.

Chapter 3

The NUMEN Target System

3.1 The targets used during Phase 1 and Phase 2

During the NUMEN Phase 1 and Phase 2, the isotopic materials required to study the DCE reactions of interest were manufactured in thin targets, deposited on carbon backings. The target deposition was usually around 1 μm thick, while the carbon foil used as substrate was a few tens of nanometers thick. The target deposition was performed in the INFN-LNS target laboratory, typically by using Physical Vapor Deposition (PVD) techniques[1].
Since the beams used for the NUMEN experiments of the Phase 1 and Phase 2 had an intensity of $\sim$ 10 nA, the power released in the targets was of the order of 0.2 W. This value was small enough to avoid any cooling system of the target, since the temperature increase was not relevant. This carbon backing, indeed, was never meant to take care of the target cooling: it had a mechanical sustain function, together with the role of post stripper.
This is not the case of the beams foreseen for the Phase 4: when the beam intensity will reach tens of μA, the heat released in the target will be such that the temperature of the target material will reach the melting point for all the foreseen target elements. Another crucial aspect of the new generation of NUMEN targets is related to the requirements on the energy resolution. Preserving the energy resolution is a key point in the design of targets suitable for the Phase 4, since the reactions under study will require for the discrimination of transitions at different (even close to each other) energy levels, as explained in more details in the following. The targets have to be designed also to face this necessity.

3.2 Target Requirements in the Phase 4

As previously described, the main change of the Phase 4 will be the increased beam intensity. The new Superconducting Cyclotron will accelerate ^{18}O and ^{20}Ne beams up to 60 AMeV, like the existing acceleration facility, but the beam intensity will reach 50 μA.
An enhanced beam intensity means a larger quantity of energy released by the beam in the crossed target, since the number of charged particles interacting with the target atoms increases. This fact leads immediately to the most crucial problem that the target system must face: the heat dissipation. As explained in a following section,

[1] The Physical Vapor Deposition is a technique to deposit thin films in vacuum. During the process, the material that will be deposited goes from a condensed phase to vapor, and then back to condensed when deposited on a substrate. Evaporation by electron beam is one of the most common techniques of Physical Vapor Deposition and will be described in the following, since it is the one used for the NUMEN Phase 4 target production.

the heat released in the target could cause serious damages, if not dissipated. For this reason, a dedicated cooling system is necessary.
The second requirement is related to the thickness and the thickness uniformity. Both these features must be carefully evaluated to minimize the effects on the energy resolution (e.g. the energy dispersion and the straggling, described in the following).
All these aspects must be taken into account and make the target design one of the most crucial and challenging part of the NUMEN upgrade.

3.2.1 The Heat Dissipation

As previously described, DCE reactions will be provided by beams of ^{18}O and ^{20}Ne with energies ranging from 15 to 60 AMeV. The beam intensity will be around 50 μA.
The power dissipated by the beam in the target can be calculated from the average energy loss, for ionization, of a single particle of the beam with the formula 3.1.

$$P_{deposited}\ [W] = E_{deposited\ by\ a\ single\ ion}\frac{I}{q_{ion}} \tag{3.1}$$

$P_{deposited}$ is the total energy deposited per second by the beam in the target, $E_{deposited\ by\ a\ single\ ion}$ is the average energy in J deposited by a single charged ion when crossing the target, I is the beam intensity and q_{ion} is the ion charge.
The average energy loss $E_{deposited\ by\ a\ single\ ion}$ can be predicted by the Bethe-Bloch formula, that evaluates the stopping power[2] of a charged particle which passes through the matter. The energy range of validity of this law is between 1 MeV/u and 10 GeV/u[3], so the formula can be used for the evaluation of the heat produced by the beam in the target.
The Bethe-Bloch formula and its derivation and corrections will be described in details in a following dedicated section called *Energy loss of low energy ions in matter: corrections to the Bethe-Bloch formula* of the Chapter 4; for now the important dependence to observe is the one on the energy. In the energy range of the NUMEN beams, the stopping power is inversely proportional to the energy of the projectile, because the high energy corrections are negligible: it means that the worse scenario for the heat dissipation is the one with the lower energy in the foreseen energy range of study, where beams have 15 AMeV.
This correlation between the beam energy and the deposited power can be easily seen in Table 3.1, where the deposited powers from Oxygen and Neon beams in the respective targets are reported. In these calculations, the beam intensity is supposed to be 50 μA; the target thickness has been supposed to be 400 nm for all the isotopes, as indicative value. The deposited power ranges from 0.7 to 2 W, causing a temperature increase in the target material.
From these evaluation the need of a cooling system for the target emerges. The first hypothesis elaborated to cool down the target was to keep the target extremities at a fixed cold temperature by using a metal structure that pinches the target disk [54], as

[2]The stopping power S is the retarding force that acts on charged particles crossing matter; it results in a progressive energy loss [52] [53]. It is mathematically evaluated as the lost energy per unit path x: $S(E) = -dE/dx$.

[3]It must be stressed that the Bethe-Bloch formula, even if it can fit the experimental energy loss in a wide range of projectile energies, can not be used in case of very low energy projectile. This is the case, for example, of the alfa particles coming from a radioactive decay: the energy loss process at low energies will be deeply discussed in a dedicated chapter.

TABLE 3.1: The power deposited by the beam in a 400 nm thick target.

Beam Energy [AMeV] (Beam)	^{116}Sn [W] (^{18}O)	^{76}Se [W] (^{18}O)	^{76}Ge [W] (^{20}Ne)	^{116}Cd [W] (^{20}Ne)	^{130}Te [W] (^{20}Ne)
15	2.0	1.5	2.0	2.9	2.0
30	1.2	0.9	1.2	1.7	1.2
45	0.9	0.6	0.9	1.3	0.9
60	0.7	0.5	0.7	1.0	0.7

sketched in Figure 3.1. The holding frame, if connected to a refrigerator circuit with liquid nitrogen, is kept at 100K. It is reasonable to assume that after some time from the activation of the refrigeration system the whole target system is at 100K. When the beam hits the central region of the target, it will heat the crossed material. The heat will be progressively transmitted to the periferic region of the target and then transferred to the frame. To study the heat propagation, different calculations have been made.

Analytical calculation with a circular beam spot

The first step of the temperature evaluation study consisted in an analytical solution of the heat equation.
The beam has been supposed to be circular with radius of 1 mm, with uniform distribution of the beam particles (uniform beam profile). The worse scenario for the heat production has been considered, when the beam has the lowest energy (15 AMeV) and the highest possible current (50 μA).
The target disk has radius of 0.5 cm and thickness of 400 nm.
Figure 3.1 shows a planar (front) view of the target (upper figure), with the different

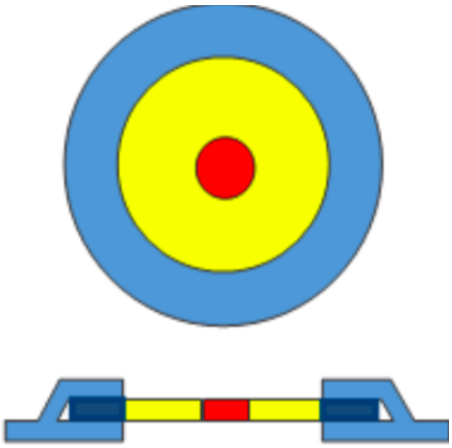

FIGURE 3.1: A standalone target kept at its extremities by a cooled structure. The red area is the one with the highest temperature, since it is fired by the beam. The peripheric circular crown is the coldest area, since it is in contact with the cooled frame (in blue). The intermediate area, in yellow, has an intermediate temperature.

zones of heating, and a side view of the target and the cooling system (lower figure). The central region, hit by the beam, is the one with the highest temperature (in red). The periferic circular crown is the colder area, since it is in contact with the cooled frame (in blue). The intermediate area, in yellow, has an intermediate temperature.

The heat equation can be analytically evaluated at the stationary state. The stationary state is reached when the amount of heat that enters in the target (through the beam interaction with the target material) is equal to the amount of heat that is transferred to the cold frame. Such steady-state is reached after a transient time (a few tens of ms after the beam start).
In cylindrical coordinates[4] the heat equation can be expressed as

$$\frac{1}{r}\frac{d}{dr}\left(r\frac{d\Theta(r)}{dr}\right)+\frac{dQ}{k\,dVdt}=0 \tag{3.2}$$

where k indicates the conduction coefficient, r is the radial coordinate, $\Theta(r)$ is the temperature and $\frac{dQ}{dVdt}$ the heat rate density of the source. $\frac{dQ}{k\,dVdt}$ is different from zero only in the region of the beam spot, since it represents the heat source.
The Fourier law, that links the heat rate and the conduction coefficient, can be written as

$$\frac{dQ}{dt}=-k\,s\,2\pi\,r\frac{d\Theta(r)}{dt} \tag{3.3}$$

where s is the target thickness.
Since the thermal equilibrium is quickly reached, the solution at the stationary regime can be calculated from 3.3 and 3.2, in the hypothesis of a uniform circular beam.
In the crown between the beam spot and the cooled frame ($r_B < r < r_C$, with r_B beam radius and r_C internal radius of the cold frame), the solution is

$$\Theta(r)=\Theta_C+Aln\left(\frac{r}{r_C}\right) \tag{3.4}$$

where Θ_C is the temperature reached at r_C and A can be evaluated as
$A\left[\frac{J}{MeV}\right]=-\frac{1}{k\,2\pi\,s}\,E_b[MeV]\,\frac{I[A]}{Ze[C]}$
$\frac{I}{Ze}$ representing the number of ions passing through the target per unit of time.
In the region of the beam spot ($0 < r < r_B$), the solution is

$$\Theta(r)=\Theta_C+\frac{q}{2}r_B^2+A\,ln\left(\frac{r_B}{r_C}\right) \tag{3.5}$$

where $q=\frac{1}{k}\frac{dQ}{dVdt}$.
Inserting in the solutions the values of all the parameters (r_C, r_B, I, k, s, Θ_C), the maximum beam intensity tolerable to avoid the target melting can be derived. It depends on the target elements, but even in the most favourable case (target with the highest melting point) the beam intensity cannot exceed 2.5 μA.
Since the beam intensity reachable after to the INFN-LNL accelerator upgrade will be more than one order of magnitude higher than this limit, it is mandatory to design a more performing cooling system.
Moreover, the beam provided by the LNS SC is not uniform but has a gaussian shape. To solve the heat equation with this more realistic beam and taking also into account the initial transient of temperature, a numerical calculation code has been implemented.

[4] It is possible to express all the calculations in cylindrical coordinates because of the symmetry of the target system.

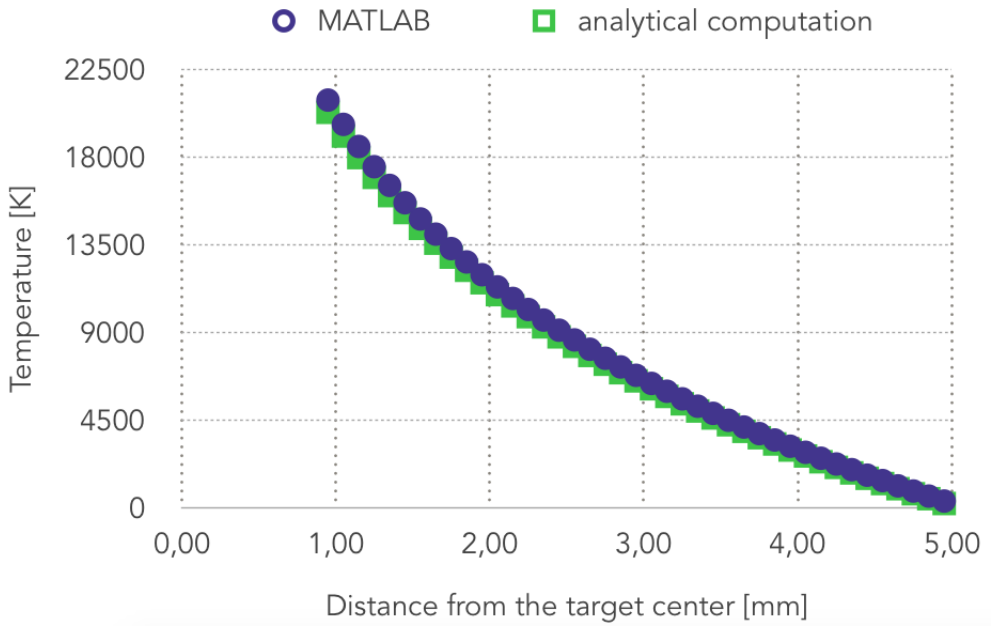

FIGURE 3.2: Temperature reached at $r_B < r < r_C$ in a ^{116}Sn 400 nm thick target, when hit by a 15 AMeV ^{18}O beam. In blue are reported the results of the MATLAB code, while in green the ones obtained with the analytical calculation.

Solution of the (not stationary) temperature equation with a gaussian beam profile

To study the heat propagation in the not stationary state, a code has been implemented in the MATLAB environment. The numerical approach allowed to use a gaussian function for the beam profile, situation similar to the real one. A gaussian with 2 mm of FWHM has been used.
Results obtained by numerically solving the time dependent heat equation are in agreement with the analytical results within a discrepancy of 3% for all the beam-target pairs. A more detailed description of these studies is reported in the PhD thesis of F. Pinna [55], where more details are described.
Figure 3.2 shows the results obtained with the two calculation methods for the ^{116}Sn target case: the temperature dependence on the distance from the target center can be observed. These values exceed the Tin melting point, so the temperatures at the target center will be surely much above the limit.

Results for all the NUMEN targets are reported in Table 3.2: the temperature reached at the center of the target is higher than the melting temperature, for all the isotopes.
This result is crucial and highlights the necessity of a more complex and powerful cooling system for the target, confirming the conclusions on the target temperatures reached solving the heat equation in the stationary state. A stand-alone target, pinched by a cooled frame, is not suitable for the very intense ion beams that will be used for the NUMEN measurements: the following section shows an innovative solution for the target cooling.

TABLE 3.2: The temperatures reached at the center of the targets and the isotopes melting points.

Target	^{116}Sn	^{76}Se	^{76}Ge	^{116}Cd	^{130}Te
Maximum temperature [K]	14070	515000	25360	22920	1882000
Melting temperature [K]	506	493	1211	594	723

3.3 An innovative target cooling system

From the first evaluations of the heat produced by the INFN-LNS beams in the NUMEN targets, the importance of a powerful cooling system is clear.
Here the necessity of an efficient heat dissipation meets also the constraints related to the needs of the other detectors placed near the target and the free room available in the scattering chamber. As previously shown in Chapter 2, a gamma detector will be placed around the target and the scattering chamber will be re-designed to host the robotics for the target handling and exchange. Moreover, the whole scattering chamber will be placed on a rotating platform that has a complex movement system under the floor level.
This complex situation leads to the imperative exclusion of cooling hypotheses as spinning targets. With that technology, the fast rotation allows to dissipate the heat through thermal radiation, but a large target area is required to make the thermal dissipation efficient. The NUMEN targets can not have extended surfaces, since it is not easy to obtain large but uniform targets (and the thickness uniformity is a crucial requirement, as explained in the following section). Moreover, the irradiated power through thermal radiation goes as T^4, so the physics process of dissipation is not suitable to low melting point targets. Another reason to exclude rotating targets is that the NUMEN target holder has to be vertically moved for calibration reasons: the movement of a rotating system would be difficult [56].
For the NUMEN case, one of the most important problems in the dissipation of the heat consists in the poor thermal conductivities of the target elements, that hampers the heat transfer from the target center to the external cooled frame. To overcome this problem, the possibility to add a substrate made of a material with high thermal conductivity has been evaluated. The presence of a substrate could also act as mechanical sustain to prevent any breaks of the thin target. The substrate must be thin, to not excessively interfere in the detection of the ejectiles energy, and its material element must not interact in reactions with large cross-sections at the energies involved in the reactions under study in the NUMEN Project.

3.3.1 The substrate importance

An ideal material to be used as substrate is carbon, that can facilitate the heat transfer offering an easy path to a cooled external frame, being light and with low density. A carbon substrate can moreover act as post-stripper[5], picking up electrons from

[5]A post stripper is a thin foil, placed downstream the target, that picks up electrons from the crossing particle, increasing their electric charge. In this way, the magnetic rigidity of ejectiles different from the ejectiles of interest (the DCE ones) can be changed: this is very useful when in the interaction between the beam and the target are produced also particles that have magnetic rigidity similar to the one of the ejectiles of interest. Indeed the post-stripper bend the trajectory of particles that are not DCE ejectiles, directing them far from the detectors. In this way, these particles don't create background signals in the detectors[57].

the ejectile and making it fully-stripped. For these reasons, carbon has been already used as backing for targets during NUMEN Phase 1 and 2, even if cooling effects were not required.
Among the different kinds of carbon allotropes, excluding diamond for handling and cost reasons, the Highly Oriented Pyrolytic Graphite (HOPG) has been identified as the best solution.
HOPG is an artificial graphite made of graphene layers oriented from each other with an angle smaller than 1°. Thanks to this particularity, the in-plane thermal conductivity is usually around 1950 W/(mK), while the conductivity in the direction perpendicular to the surface is about 3 W/(mK). The high value related to the surface conductivity is the searched key for the heat dissipation, allowing a fast transfer of the heat from the target center to the substrate extremities. These very interesting thermal properties are not crucially invalidated by the crystal damages usually due to beam radiation; this fact makes the HOPG a good radiation-tolerant substrate for a target submitted to very intense ion beams [58].
The HOPG surface is very smooth thanks to its layered nature: this fact is encouraging for our substrate pourpouses, since the thickness non-uniformities could affect the deposition uniformity.
The HOPG thickness has to be minimized to minimize effects as energy straggling and dispersion (deeply described in the following section *Energy Resolution*) that affect the resolution in the energy measurement of the DCE ejectiles. For this reason, the thinnest HOPG on the market, around 2 μm thick, has been chosen.
The Optigraph company, that sells this very unique type of substrate, has not the full control of the HOPG production mechanism for what concerns the thickness. Moreover, the company does not have the possibility to use the suitable instrumentations to perform precise thickness measurements of the sold HOPG samples. For this reason, as shown in the following chapters, the thickness characterization of each HOPG sample used as substrate is of crucial importance and the real sample thickness can significantly deviate from the nominal one.
To evaluate the efficiency of a cooling system based on a HOPG substrate for the target, the substrate presence has been implemented in the previously described numerical code. A target 400 nm uniformly thick has been considered, with a 2 μm uniformly thick HOPG substrate. The target system border is supposed to be kept at a fixed cold temperature of 40K. This cold temperature can be easily maintained by using a cryocooler, as explained later. The beam profile is supposed to be gaussian (FWHM of 2 mm), with intensity 50 μA and energy of 15 AMeV.
The steady state is reached in a few tens of ms: graphics of figure 3.3 represent the case of the ^{116}Sn target fired by a 15 AMeV ^{18}O beam with intensity 50 μm, showing the temperature of the target when the beam starts and when the stationary condition is reached. They are 3D plots, where the planar coordinates indicate the target plane and the vertical coordinate indicates the reached temperature. The beam is supposed to hit the target at its center, represented by the (x,y) coordinates (0,0). The graphic on the left shows the temperature distribution after 10^{-9} s from the beam start: while the most of the target is still at the cold temperature of the cooling system, the target center surface starts to be heated. After a certain time interval, here equal to 0.02 s, the trend is more smooth because the temperature at the target center is uniform along the thickness crossed by the beam; the temperature decreases uniformly when approaching to the cooled target border.
This study has been done for all the targets, with the same boundary conditions ($E_{beam} = 15$ AMeV, $I_{beam} = 50\,\mu$A, $T_{cold} = 40$K, thickness$_{target} = 400$ nm, thickness$_{HOPG} = 2\,\mu$m): results are reported in table 3.3, again compared with the melting points of

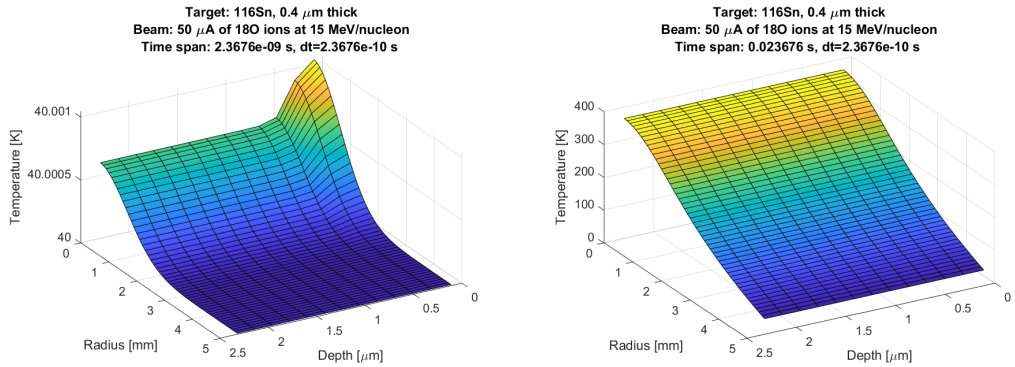

FIGURE 3.3: Temperatures of the target, when sustained by a cooled 2 μm thick HOPG substrate, at the run start (left) and at the stationary state (right).

the different target isotopes.
It can be observed that the found solution for the cooling of the target is sucessfull:

TABLE 3.3: The temperatures reached at the center of the targets when sustained by a 2 μm thick HOPG substrate, which extremities are mantained at 40K.

Target	^{116}Sn	^{76}Se	^{76}Ge	^{116}Cd	^{130}Te
Maximum temperature [K]	368	1337	367	448	688
Melting temperature [K]	506	493	1211	594	723

all the targets reach maximum temperatures under their respective melting temperatures. The only exception is the ^{76}Se target: it is reasonable to consider a decrease of the beam intensity when studying reactions involving this target.
These promising results push to start with the target production. The best way to produce the target system here designed is by the deposition of the target on the substrate.

3.3.2 The target deposition

HOPG is not particularly suited to be used as substrate for material deposition: its very smooth surface, although it is a good feature for the thickness uniformity, does not facilitate an easy adhesion of a deposited layer of another material. For this reason, the related bibliography is very poor: the study of the physics of the deposition of different kinds of materials on graphite, made in the context of the NUMEN target research, undoubtedly has been pioneering and challenging.
Considering the constraints related to the target, it must be stressed that only specific isotopes of the target materials can undergo DCE reactions: the presence of other naturally occurring isotopes of the same element would only introduce background noise and must be therefore avoided. Materials which are artificially enriched with a certain isotope (typically with purity $> 99\%$) can be very costly; therefore, the chosen deposition technique must be fit to use little quantities of it.
Lastly, the target deposition has to be as uniform as possible, so the deposition process must be well controlled.
All these requirements lead to exclude common and largely used deposition techniques as plasma sputtering [59].

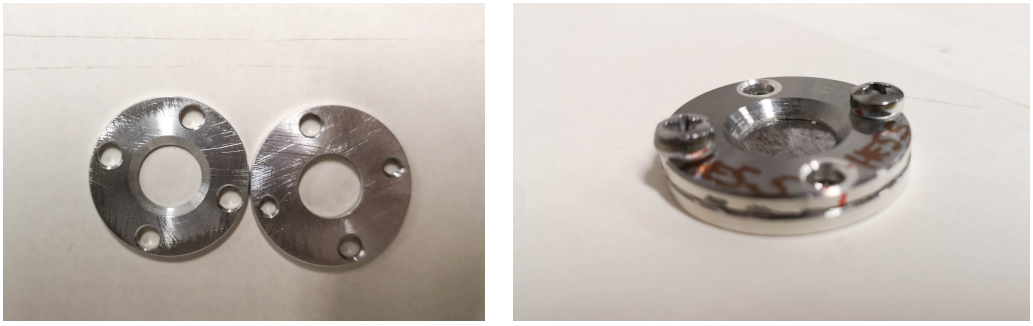

FIGURE 3.4: The two disks that form a frame shown separated and then joined together, with also a graphite substrate pinched between them.

The Electron-Beam Physical Vapour Deposition (EBPVD) technique has been chosen instead.
The deposition is made by the evaporation of the target element by directing an electron beam on a crucible that contains the target element [60]. The amount of material in the crucible can be small, limiting the costs, and the average reachable uniformity on the deposition thickness can be around 5%.
To improve the surface adhesion between the graphite and the deposited layer, the interposition of a buffer layer has been investigated and, in some cases, implemented.
The first pioneering depositions of the target elements have been performed in collaboration with the Trustech Company, specialized in micro and nanotechnology. The frames are placed upside-down on a plate, located in the upper part of the evaporator machine. The evaporation process happens from below upwards, so one side of the substrate pinched in the frame receives the deposition while the other, shielded by the plate, does not.
The frame used to host the substrate for the deposition has been designed to clamp tight the graphite, without causing folds or bendings. In figure 3.4 the frame can be observed. It is formed by two disks with external diameter of 2.5 cm and 2 mm thick, each having four screws holes. Both the disks have a central hole with diameter 1 cm. Once the two disks are joined together, the frame is placed on the evaporator plate. One disk has two threaded holes to allow the union by screws with the other disk; the other two holes are smooth (as the four holes of the other disk) to allow the screwing of the whole frame to the plate used in the evaporator to hold the samples. The central hole of the other disk has a countersink to avoid boundary effects in the deposition.
This frame design allows to produce a final target system where the target is deposited only in the central area of the graphite substrate, complying with the target design assumed in the thermal calculations.

Once produced, the prototypes of target systems have been carefully characterized with different and complementary analysis techniques: this research will be described in the details in the following chapter, being the main topic of this PhD.
Before that, it is of crucial importance to discuss the role of the target thickness and uniformity in the determination of the energy resolution in the NUMEN experiment.

3.3.3 The Energy Resolution

For the NUMEN Project purpose, the correct evaluation of the DCE products energies is of crucial importance. For this reason, the measurement of the ejectiles energies must be performed with very high resolution.
The required resolution depends on the ejectile isotope, but it is usually around 0.5 MeV [62]. The sum of all he contribution to the error must remain below this value. In addition to this source of errors, there are two more contributes due to the experimental set up, related to accelerator and spectrometer. The beam provided by the Superconducting Cyclotron is not monochromatic: with the current facility the spread around the nominal value is around $\frac{1}{1000}$ of the nominal energy. During the R&D phase presently ongoing, magnetic optics and collimators are under study to maintain or decrease the actual beam energy spread, even with increased beam intensity. An equivalent contribute of $\frac{1}{1000}$ is added during the reaction products detection; it is mainly due to the detectors capabilities and to the algorithm used for the tracks reconstruction in the MAGNEX spectrometer.
Since it is not feasible to reduce these contributes, the uncertainty due to the target must be minimized. To understand the influence of the target system on the overall energy resolution, the effects affecting the reaction product energy must be considered. The main two effects that affect negatively the energy resolution are dispersion and straggling.

Dispersion

If a DCE happens, we can only know that it occurred in the target, but not the target depth at which the reaction took place. Since the projectile and the ejectile nuclei have different atomic number, their energy loss (ruled by the Bethe-Bloch law) in a definite material thickness is different. Therefore, the depth at which the DCE reaction takes place has influence on the energy loss by the ejectile in the target, so on the cross-section evaluation.
In the reconstruction algorithm, it is assumed that the reaction happens in the exact middle of the target thickness: this a-priori choice leads to an uncertainty that contributes to the energy resolution. This uncertainty can be quantified with the difference between the final energy of the ejectile if the DCE reaction occurs on the target surface and the same energy in the case of DCE occurred at the end of the target depth. It is clear that the thicker is the target, the more considerable will be this difference between the two energies.
Since this effect is strictly related to the DCE occurrence, only the target is relevant since no reactions of interest occur in the graphite substrate.
Graphics of figure 3.5 show an example of these dispersion studies. Here are reported the calculations related to the DCE reaction $^{116}Sn(^{18}O,^{18}Ne)^{116}Cd$, with both ejectile and target daughter in ground state. Three different exit angles of the ejectiles have been considered: 1°, 5° and 15° degrees from the beam axis. The beam energy is supposed to be 270 MeV. The dependence of the ejectile energy on the depth of the target at which the reaction occurs can be studied. It can be observed that for small ejectile exit angles, the energy spread between the result of a DCE happened at the target surface and the one resulting from a reaction occurred at the end of the target is smaller than 10 KeV. This difference becomes significant when the exit angle increases: at 15° the energy gap due to the dispersion is more than 2 MeV.

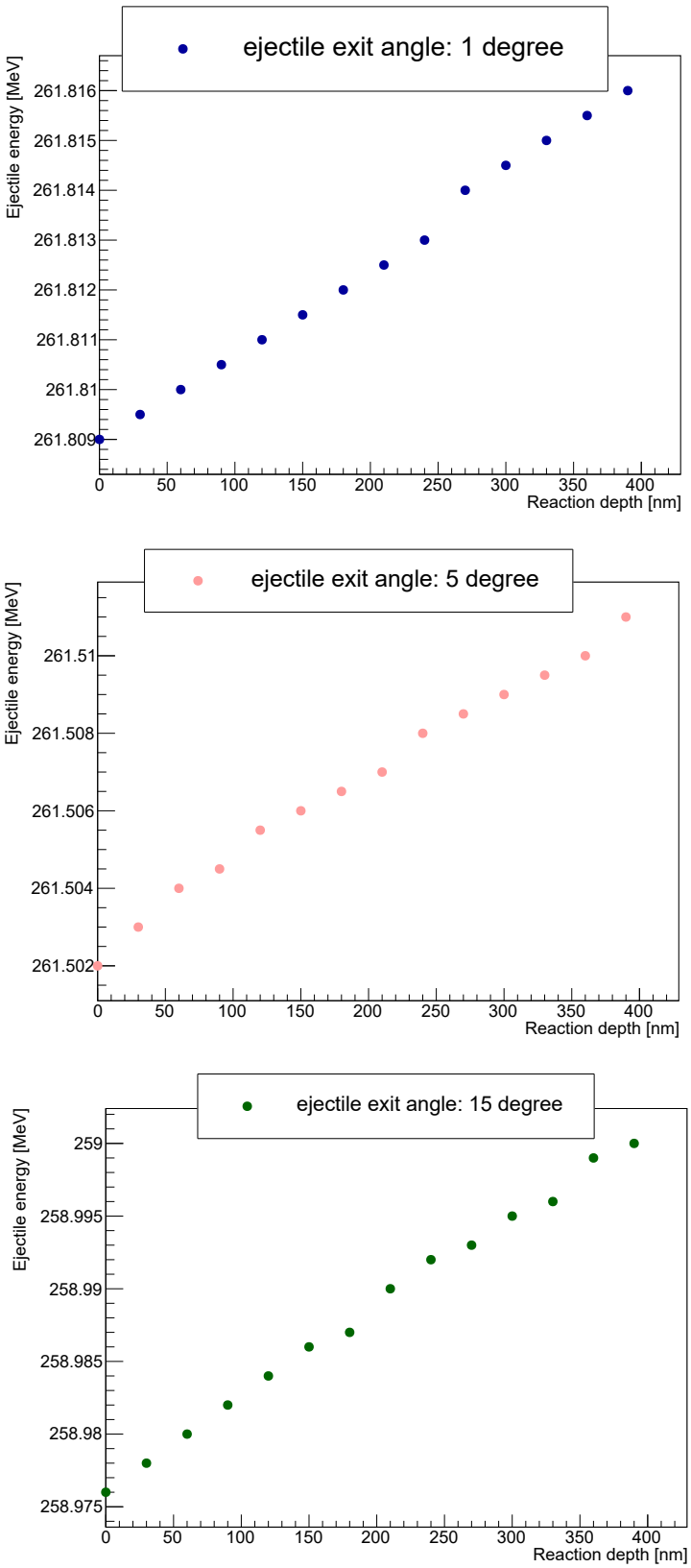

FIGURE 3.5: The dependence of energy of the ejectile, exiting at 1°, 5° and 15° degrees from the beam axis, on the reaction depth. Both ejectile and target daughter are in ground state.

Straggling

The straggling effect is related to the statistical fluctuations in the energy loss process, since the number of collisions between the beam nucleus and the electrons of the target atoms fluctuates. This effect results in a certain distribution of possible final energies of the beam nucleus. Moreover, this effect depends, as the dispersion, on the atomic number of the projectile: it means again that the change of the nucleus atomic number induced by the DCE changes also the uncertainty due to the straggling effect.
There are different models to evaluate this effect; in this study the gaussian model has been used [61]. The standard deviation $\sigma_{straggling}$ of the energy spread added by the straggling effect to the energy of the crossing particle can be estimated as:

$$\sigma_{straggling} = \sqrt{\xi E_{max}(1 - \beta^2/2)} \tag{3.6}$$

where ξ is the mean energy loss and E_{max} is the maximum energy that an electron can transfer in a single collision[6]. These two quantities can be calculated from the electron charge e and mass m_e, the Avogadro number N_A, the material density ρ and its crossed thickness δx, the projectile mass m_x, the projectile charge z, and the target nucleus atomic number Z and mass number A:

$$\begin{aligned} \xi &= \frac{2\pi e^4 N_A z^2 Z \rho \delta x}{m_e \beta^2 c^2 A} \\ E_{max} &= \frac{2 m_e \beta^2 \gamma^2}{1 + 2\gamma \frac{m_e}{m_x} + \left(\frac{m_e}{m_x}\right)^2} \end{aligned} \tag{3.7}$$

Straggling occurs both in the target and in the substrate and is proportional to their thicknesses.

For the described reasons, the target thickness should be minimized to contain the error in the energy evaluation. Nevertheless, it must be reminded that the target thickness is proportional to the collected statistics, since the number of nuclei available to a DCE increases with the material thickness. The collected statistics is a sore point in the NUMEN research, since the DCE cross-sections range from a nb/sr to a few μb/sr. A possible approach is the beam intensity increase, but also here there is an upper limit due to experimental possibilities and the large amount of heat produced in the target, as shown. Therefore the target thickness must be a compromise between the required energy resolution and the collected statistics.
The substrate thickness must be minimized too, since no DCE can occur within it and would only contributes to increase the error due to straggling.
Together with the thickness minimization, also the thickness uniformity of target and substrate must be preserved. Indeed, a particle that crosses a valley of the target (or substrate) will lose less energy than another one that meets, for example, a bump of the target deposition. This will be traduced in a further broadening in the shape of the energy distribution. A relevant non-uniformity could affect all the considerations on the energy resolution and consequently on the DCE cross-sections studies.

[6] β is the relativistic quantity usually estimated as $\beta = \frac{v}{c}$. From β, γ is usually calculated as $\gamma = \frac{1}{\sqrt{1-\beta^2}}$.

Another possibility must be considered, when evaluating the overall energy resolution. As previously mentioned, the ejectile can exit from the DCE reaction in different energy states. Every excited state different from the ground state will mean a decreasing of the kinetic energy of the ejectile, shifting the whole energy distribution to lower values. Even if it causes a rigid shift of the distribution and not a spread of the energy peak, this possibility must be carefully taken into account.

To evaluate the energy separation between ejectiles coming from DCE resulted in products at different energy states, kinematic evaluations have been done. The DCE reaction has been supposed to happen in the middle of a 400 nm thick target: to calculate the ejectile energy, the energy loss of the projectile before the DCE reaction has been calculated, then with a kinematic calculation the energy of the ejectile right after the DCE reaction has been established. In this calculation, the exit angle of the ejectile has been considered to be in the range 1°-15° from the beam axis. Finally, the energy loss by the ejectile crossing the remaining part of the target has been evaluated, giving the final energy of the ejectile. The contribution of the energy loss in the substrate has been not taken into account, since it is a fixed contribution and does not influence the energy separation between different ejectiles here studied.
Graphics reported below show the results for DCE with ejectiles exiting at different angles, in different combinations of energy states of ejectile and target daughter. The graphics of figure 3.6 show this study performed for the DCE reactions $^{76}Ge(^{20}Ne,^{20}O)^{76}Se$ and $^{130}Te(^{20}Ne,^{20}O)^{130}Xe$. Figure 3.7 shows the same study but performed for the DCE reaction $^{116}Sn(^{18}O,^{18}Ne)^{116}Cd$. The beam energy is supposed to be 270 MeV.

Observing the results at the same ejectile exit angle, the grapichs show that the reactions more easily discriminated in energy are the ones resulting with both target daughter and ejectile in ground state and the one related to both nuclei in the second excited state; in these cases, the energy separation is around 5 MeV. The other types of DCE are separated of at least 5 KeV from each other, with the only exception of the reaction with the Sn target, where the combination ejectile in the first excited state - target daughter in the second excited state and the combination ejectile in the second excited state - target daughter in the ground state have energies different for less than 2 KeV, if the ejectile exits at the same angle.
Concerning the angle dependence, it can be observed that the reactions resulting in the same energy states combination, but with ejectiles exiting in the angular range 1°-4°, are not easy to be discriminated. The energy span between DCE reactions occurred at the same products energy states but with ejectiles at different angles is more or less fixed for all the energy states combinations. For reactions involving Sn and Te targets, this energy gap is around 3 MeV, while for reactions with the Ge target this difference is around 5.5 MeV.

The evaluation of the cumulative effect of all these contributes that affect the overall NUMEN energy resolution is not so simple, since they have to be considered together. To perform this study, a Monte Carlo simulation has been implemented.

The Monte Carlo code

The Monte Carlo code simulates the *energy history* of a particle that crosses the target system, considering all the effects that can occur. To take into account the possibile variations of the projectile energy different from the normal energy loss process for ionization, the statistical events have been randomized, using theoretical models

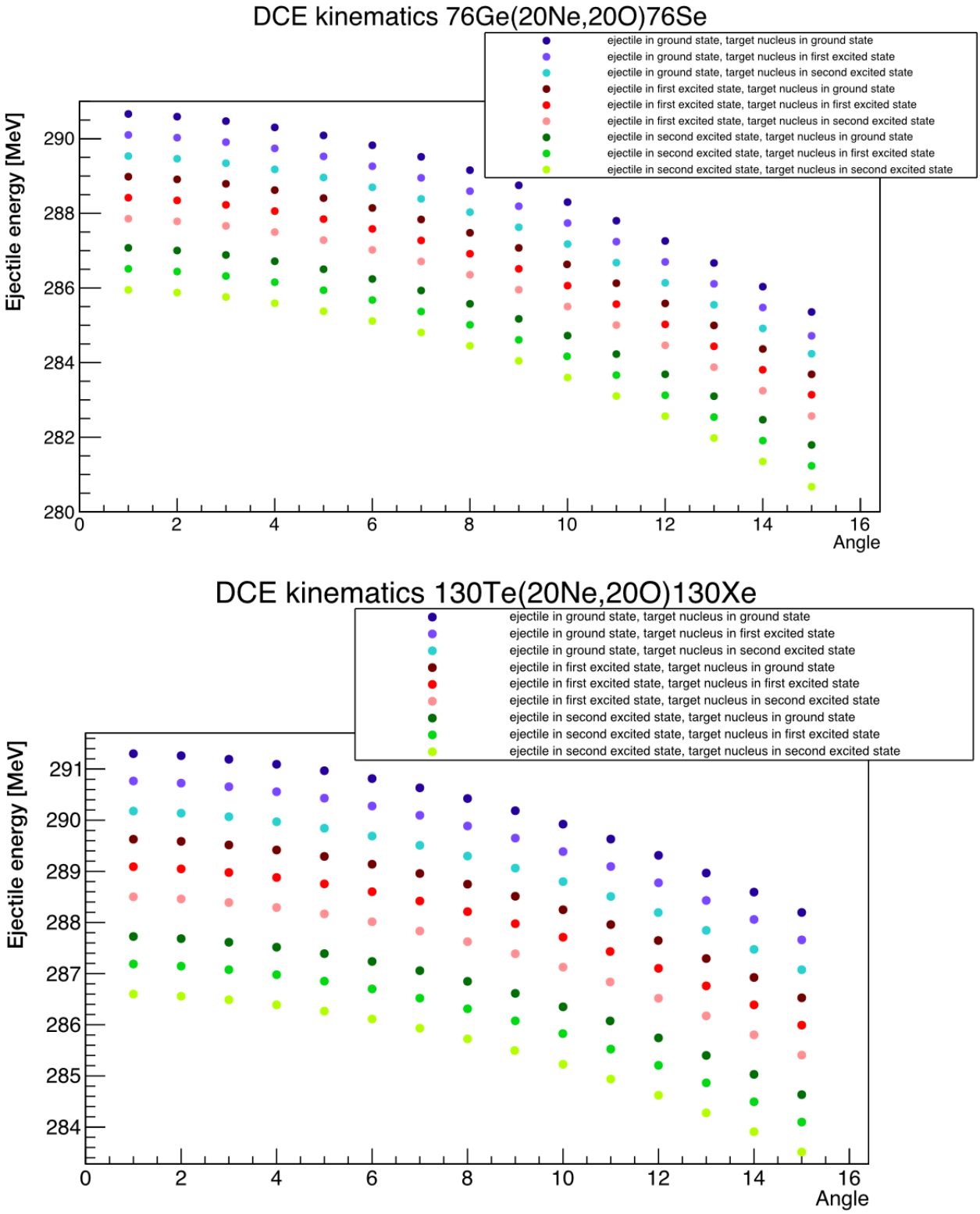

FIGURE 3.6: The energy of the ejectile exiting at different angles from DCE resulting in products in different energy states, for the ^{20}Ne beam induced DCE.

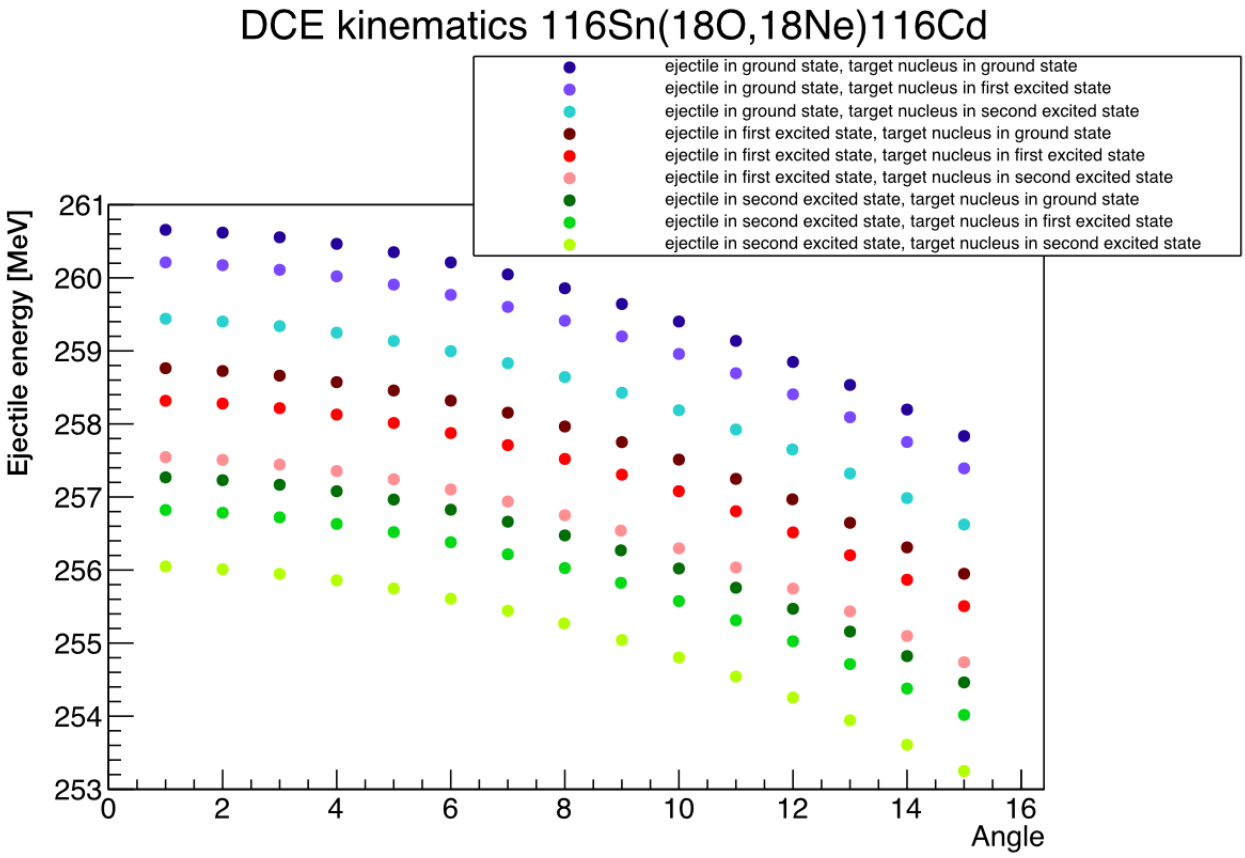

FIGURE 3.7: The energy of the ejectile exiting at different angles from DCE resulting in products in different energy states, for the reaction ^{116}Sn(^{18}O,^{18}Ne)^{116}Cd.

when present (as for the straggling effect evaluation).
Since the real estimations for the DCE cross-sections are still to be evaluated (this is the goal of the NUMEN Project!), a flat statistics has been assumed: the ground state, the first and the second excited states of the ejectile energy state have been assumed as equally likely.
A detailed description of the code can be read in reference [62], here only the main results will be reported.
For each prototype of the NUMEN targets, the physics features have been inserted as inputs for the simulation, to evaluate if the required energy resolution would be guaranteed if using that specific target system. It is important to note that the physical features of thickness and thickness uniformity of target and substrate used as input for the simulations are the real values related to the first produced prototypes. The evaluations of these features have been obtained with the target system characterization procedure that has been designed and performed in the past three years, and will be deeply discussed in Chapter 4.
Here are reported, as example, the Monte Carlo energy distributions for two target systems, named C7 and C21. C7 is a prototype of Tin target, deposited on a substrate of HOPG nominally 2 μm thick. The deposition thickness is 170 nm, with a considerable thickness non-uniformity (around 62%)[7]. The substrate real thickness is 2.63 μm, with non-uniformity of 4%. The sample named C21 is instead a Germanium target prototype, deposited on a thinner HOPG substrate. The Germanium deposition is 372 nm thick, with a non-uniformity of 14%; the substrate is 2.14 nm, with non-uniformity of 5%.
Figure 3.8 shows the outcomes of the simulation for the target systems C7 and C21.

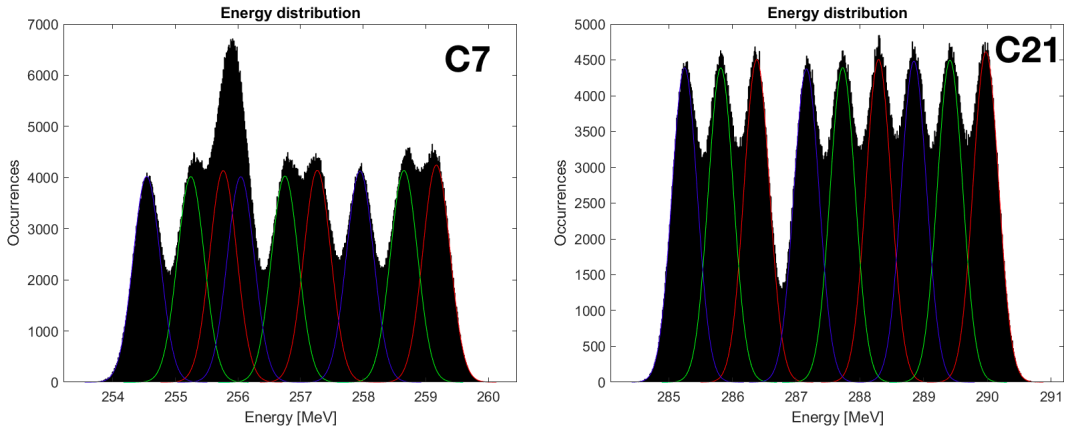

FIGURE 3.8: The energy distribution of the ejectiles, evaluated with a Monte Carlo code: here the results for sample C7 (Tin) and C21 (Germanium).

In these graphics, each peak corresponds to a different combination of ejectile-target daughter energy levels: since the simulation considers the first three energy levels of the reaction products, nine combinations are possible. Each peak is fitted with a gaussian, to facilitate the separation among the peaks. The red gaussians correspond to a target daughter in the ground state, while green and blue gaussian fits are the first and second excited states of the target daughter. The three peaks at higher kinetic energies correspond to the reactions that produce a ground state ejectile, while

[7] The thickness non-uniformity estimation will be deeply described in Chapter 4. The percentage R_{n-u} here reported is evaluated as the ratio between the spread in the thicknesses distribution and the average thickness.

the triplet at lower energies is related to reactions resulting in an ejectile in the second excited state.
The first plot of figure 3.8 shows the energy distribution of the ^{18}Ne ejectiles after the DCE reaction $^{116}Sn(^{18}O,^{18}Ne)^{116}Cd$. It is possible to notice that in each triplet the second excited state of the target daughter is the most separated of the three energy states; however, it is not easy to discriminate between the target daughter second excited state peak of the triplet related to the ejectile in the first excited state (blue peak around 256.1 MeV) and the target daughter ground state peak of the triplet related to an ejectile in the second excited state (red peak around 255.7 MeV). To enhance the energy separation between the peaks, the target features of thickness uniformity (very poor for this Tin prototype) should be improved.
The second plot shows the result of energy resolution obtained if the target system prototype C21 would be fired by a ^{20}Ne beam (the same colours are used in legenda). The better uniformity of the Germanium deposition thickness allows a scenario where the different energy states can be distinguished with high confidence.

3.4 The cryocooler cooling system

As described in the previous chapters, the NUMEN targets must be properly cooled down to avoid a beam-caused melting. The found solution to quickly transfer the heat from the target center, fired by the beam, to its boundaries is the deposition of the target isotope on a HOPG thin substrate.
The analytical and numerical evaluations of the heat transfer gave successful and promising results, as shown. These evaluations are, however, based on the boundary condition of a cooling system that is able to keep the HOPG and target extremities at a cold fixed temperature of 40K. The cooling system has also to face the spatial requirements of the NUMEN scattering chamber that reserves a very limited free space.
Different solutions have been considered and then discarded for spatial reasons and constraints due to the integration with the detectors that will surround the target.
A reliable solution can be provided by a cryocooler based cooling system. A cryocooler is a cooling device where a circuit with a refrigerant liquid, like liquid helium, can cool down a cold finger at a fixed temperature [63]. This solution avoids the footprint due to the presence of pipes with refrigerant liquid in the scattering chamber. Moreover it easily allows the vertical movement of the sample placed on the cold finger of the cryocooler, useful possibility during the calibration procedures. The chosen cryocooler is able to dissipate up to 20W, keeping the graphite substrate extremities at less than 40K. The details of the cryocooler placement and movement can be found in reference [35]. The image on the left of figure 3.9 shows a section of the scattering chamber together with the cryocooler and the actuator for its vertical movement.

The target system will be host by a copper structure, that will be placed on the top of the cryocooler cold finger, mounted with a bayonet coupling. The shape of the target system holder has been optimized to facilitate the heat flow toward the cryocooler cold finger, allowing a wide solid angle aperture for the gamma array detector measurements. The image on the right of the figure 3.9 shows the copper holder. The sample holder is shaped to accomodate four different locations. The one at the center of the structure, near the cyrocooler cold finger, is the one devoted to the target system host. On the top, three other spots are foreseen: one for a sample of graphite for reference measurements, one for an alumina disk useful to check the

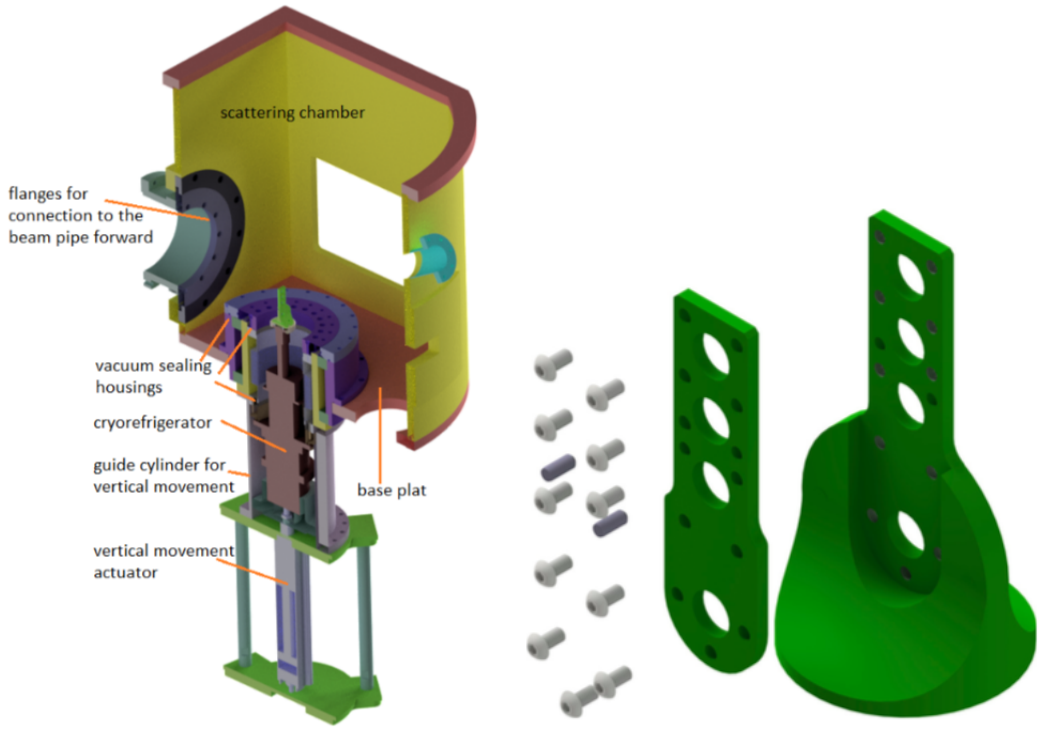

FIGURE 3.9: On the left: a section view of the scattering chamber with the cryocooler system. On the right: the copper holder that will host the target system, the graphite sample and the alumina disks; all the different components are show.

alignment with the beam and an empty hole to measure the background generated by the copper structure.

3.5 The robotic system

After a certain time of data taking with a specific target system, the change of the target will be required to study another DCE reaction. Very intense ion beams will be used in this NUMEN Phase, so the access to the experimental hall will be very dangerous for radioprotection reasons. It will be not possibile to handle the used target physically entering into the scattering chamber, since the materials in this experimental area will be activated. For this reason, a robotic system has been designed to remotely operate in the scattering chamber [46].
A robotic manipulator has been studied to remove the target system holder and change it with a new one. It unscrews the target holder by the bayonet coupling and then moves the copper frame out of the scattering chamber. Figure 3.10 shows the robotic arm that clamps the holder by the top before the unscrewing process.

The robotic arm has been also programmed to move the used holder to its foreseen place on a bigger platform, designed to host a certain number of target holders outside the scattering chamber. This platform moves on a sliding rail, guiding the holders to a protected storage, where all the activated material will be stored until the human manipulation will be safe. These complex movements have been carefully studied and simulated. The images of figure 3.11 show two moments of the target holder transport to the radioprotected storage.

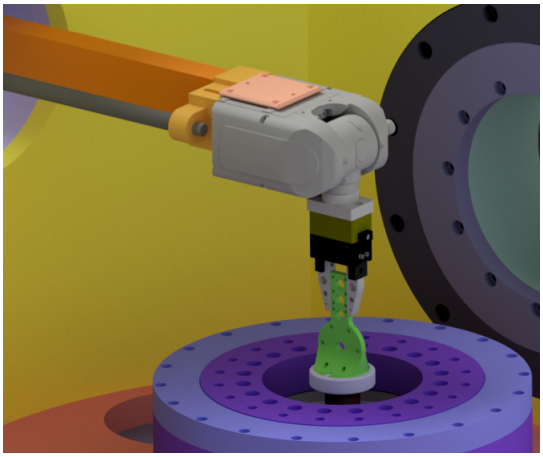

FIGURE 3.10: The robotic manipulator clamps the target system holder in the scattering chamber, before its unscrewing from the cold finger of the cryocooler.

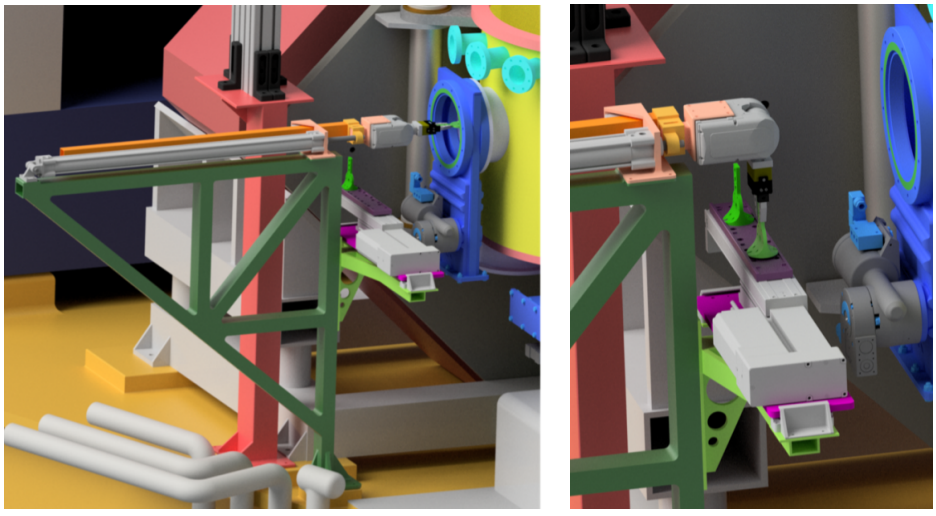

FIGURE 3.11: Two frames during the target holder exchange procedure: in the first image, the target holder is removed by the scattering chamber through the lateral door by the robot manipulator, while the second image shows as the target holder is placed on the sliding platform.

Simulations of the cooling process of the copper frame containing the target by means of the described cooling system have been performed by using the software COMSOL Multiphysics [64]. These evaluations verified that if the copper holder basis is kept at 40K, the graphite extremities will be maintained at the same temperature even if the beam fires the target center [65]. Therefore, this complex cooling system is able to preserve the target from the beam-caused melting and will be used in the NUMEN Phase 4 experimental campaigns.

Chapter 4

Low Energy Ion Beams Analysis Techniques

As previously described, the requirements of the NUMEN project related to the energy resolution demand for a very precise characterization of the physics feature of the targets. To obtain an overall study of the target systems, different analysis techniques can be exploited.
In this context, four different analysis techniques have been experimented, two nuclear based analysis and two microscopies. In this Chapter each technique will be described, starting and focusing on the nuclear based ones, that are the focal point of this PhD.
To exhaustively describe this research, a digression about the energy loss of low energy ions in matter is necessary.

4.1 Analysis techniques based on ion beams: a brief introduction

A charged particle passing through matter loses a portion of its energy by ionization processes[1]. Through the evaluation of this energy loss, calculating the stopping power of that specific particle in the material, the crossed material thickness can be deduced. These techniques allow to get very precise results of thickness and thickness uniformity, not damaging the sample. For these reasons they constitute a very useful (and diffusely used) tool for the analysis and the characterization of targets involved in Nuclear Physics experiments, where the knowledge of the target thickness is required with very high precision.
To perform accurate energy loss measurement, it is necessary to have an energy loss large enough to be measured with good precision. Since the energy loss is proportional to the thickness crossed by the charged particle, thin samples represent a challenge in this type of research.
In these cases, low energy ion beams can be exploited, since their stopping power is high enough to cause a significant energy loss in a limited crossed thickness.
Ion beams with energies of a few MeV are the best probe to study samples with thickness ranging from tens of nanometers to a few micrometers, depending on the

[1]Charged particles crossing matter lose a portion of their energy through elastic and anelastic collisions with atomic electrons and nuclei. The energy loss process can occur by ionization or by Bremsstrahlung effect (negligible for heavy charged particles). If the particle mass is orders of magnitude higher than the electron mass, if the atomic electron that interacts with the charged particle can be considered free and at rest, and if the transferred impulse in the interaction is small, the energy loss occurs mainly by ionization. The average energy loss rate can be calculated through the Bethe Bloch formula, used for relativistic particles. In the following more details are given.

sample material.

In the first years of the XX century the scientific community made many discoveries on the properties of ions. Examples are the ion induced X-rays emission studied by Chadwick in 1912, the Rutherford scattering examined by Geiger and Marsden in 1913 and the nuclear reactions investigated by Rutherford from 1919. It was only in '50s that these finds have been exploited for the analysis of samples. The first measurements based on the Rutherford scattering process are reported in [66] in 1957, where proton and deuteron beams have been used for chemical analysis [67]. This study was the pioneer of a wide research that started in the '60s and goes on until today.
Ion beam analysis have a wide spectrum of advantages that make them largely used until today. They can provide a large variety of information on the sample, as the thickness, the thickness uniformity and the chemical composition. Moreover, they are non-destructive, allowing different and repeated data takings on the same sample (in this way, different techniques can be exploited to study the same samples different times, providing also redundant and cross checking information). Finally, the beams that lose energy in the sample can be provided not only by particle accelerators, that anyway are increasingly diffused, but also by radioactive sources, more easily used in small laboratories.
According to the beam features and energies, different types of studies can be performed. In this PhD research, Rutherford Backscattering and Alpha-Particle Transmission have been largely used and for this reason they will be subject of a following section.
Before entering into the details of these two analysis techniques, a deepening on the physics process of the energy loss is necessary.

4.2 Energy loss of low energy ions in matter: corrections to the Bethe-Bloch formula

The energy loss of a charged particle crossing a medium can be referred to two different processes: one is the interaction with the medium nuclei (nuclear stopping) and one is the energy loss to the medium electrons (electronic stopping). The second contribution is usually greater than the first one, since the probability to interact with an electron of a target atom is much greater than the probability to interact with a nucleus. This evaluation leads to approximate the energy loss to the only electronic component, ignoring any nuclear reaction between the beam ion and a target nucleus.
For energetic light ions, with energy between 1 MeV/u and 10 GeV/u, the ion can be assumed fully stripped (so its charge is due only to protons of the nucleus) and moving much faster than target electrons [68]. In this case, the Bethe Bloch formula[2] can be successfully used to evaluate the energy loss of a particle thorough matter, adding small corrections. When the particle energy is instead lower than 1 MeV/u, the Bethe-Bloch equation validity is compromised by charge neutralisation effects, as described later.
The Bethe-Bloch stopping power equation is commonly expressed as:

[2] Again it must be reminded that the Bethe-Bloch equation considers only the electronic energy loss.

$$S = \frac{kZ_2}{\beta^2} Z_1^2 L(\beta) \tag{4.1}$$

where:
S is the stopping power.
k is a constant: $k = 4\pi r_0^2 m_e c^2$ with r_0 electron classical radius and m_e the electron mass. In units of eV/(10^{15} atoms/cm^2), $k = 0.0005099$.
Z_2 is the target atomic number.
β is the relative ion velocity, $\beta = v/c$.
Z_1 is the ion atomic number.
$L(\beta)$ is the so-called *stopping number*, and contains the corrections to the energy loss obtained for a basic two particles scattering.
The term $L(\beta)$ is the sum of different correction terms, added to the original Bethe-Bloch version of the stopping power formula:

$$L(\beta) = L_0(\beta) + Z_1 L_1(\beta) + Z_1^2 L_2(\beta) + ... \tag{4.2}$$

Fano corrections

L_0 is the correction made by U. Fano [69]. It contains the largest corrections, and it is expressed as:

$$L_0 = \frac{1}{2} ln\left(\frac{2m_e c^2 \beta^2 \Delta E_{max}}{1-\beta^2}\right) - \beta^2 - ln < I > - \frac{\delta}{2} - \frac{C}{Z_2} \tag{4.3}$$

ΔE_{max} is the largest possible energy loss in a single collision[3], while $< I >$ is the mean ionisation term and corrects for the quantised energy levels of the target electrons.
Moreover, Fano added two terms: the *density effect* correction $\delta/2$ and the *shell correction* C/Z_2.

The *density effect* takes into account that in dense materials the experimental stopping power of relativistic high energy particles is less than the predicted [70]. Indeed in solids, the dielectric polarization of the material modifies the particle field, resulting in lower stopping power values. The difference between theory and experiment widens with increasing the particle energy or the crossed medium density. Since this correction is relevant when the kinetic energy of the particle exceeds its rest mass, it can be trascurated for low energy ions in common targets.

A term that instead is very important for low energy ions stopping power is the *shell correction* term. It is added to correct for the Bethe-Bloch requirement that the ion velocity is much larger than the target electron velocity and is evaluated through the calculations of the interaction of the ion with electronic orbits. Indeed, when the particle energy is no more relativistic, in the study of the collision between the ion and a target atom each target's electron orbital bonding has to be considered. For protons with energies between 1 and 100 MeV, it is a large correction (up to 10%).

[3] Writing the ion mass as M_1, the ΔE_{max} is:

$$\Delta E_{max} = \left(\frac{2m_e c^2 \beta^2}{1-\beta^2}\right)\left[1 + \frac{2m_e}{M_1(1-\beta^2)^{\frac{1}{2}}} + \left(\frac{m_e}{M_1}\right)^2\right]^{-1} \tag{4.4}$$

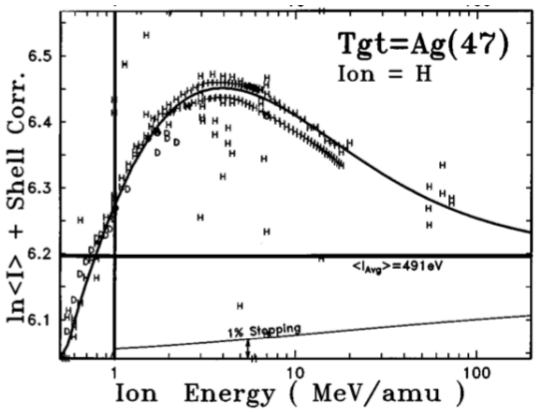

FIGURE 4.1: Comparison between the two shell corrections in Ag target.

Shell corrections can be calculated with different approaches; the most common are the *Hydrogenic wave Functions* (HWF) and the *Local density approximation* (LDA).
The *Hydrogenic wave Functions* technique describes the target electrons with hydrogenic wave functions, resulting in a final shell correction that is the sum of contributions of each target electron, without correlation. The parameters of these equation are obtained by experimental stopping data, while the Local density approximation can be instead calculated without any free parameters.
The *Local density approximation* approach considers the target as a linear superposition of free electron gases, of various densities.
Figure 4.1 compares the two different approaches with the experimental data, for a Silver target [68]: it is difficult to discriminate which shell correction is the best one, and usually an average between the two is used as correction for the Bethe-Bloch equation. The experimental data are quoted as accurate within 1%, even if the data scatter is greater. The differences between the two C/Z_2 approaches can change the final stopping power for less than 1%. Note that the values reported are related to the sum of the shell correction and the mean ionization potential[4].

Barkas correction

L_1 is the Barkas correction. It is multiplied to an odd power of Z_1, so it is sensitive to the ion charge sign. Even if it is a second order correction, it is significant especially for low energy ions.
The Barkas term corrects the Bethe-Bloch assumption that the initial distribution of target electrons is uniformly distributed about a quiescent atom. Indeed, when a positive ion approaches to the target atom the electrons are attracted to the incoming particle, while a negative ion repels them. This polarization of the target changes the electronic density crossed by the ion, changing its energy loss (and stopping power). Moreover, a particle with charge higher than 1 meets an electronic density different from the one seen by a single-charge ion.
This effect becomes negligible for high energy ions (> 10 MeV/u), when target electrons have no time to move before any interaction occurs. At low energies (< 1 MeV/u), the Barkas effect is difficult to isolate and evaluate, since the ion is neutralized because it tends to pickup electrons from target atoms, as described in the

[4]Fano suggested to isolate the two components of the stopping power that require extensive and complex theoretical model, i.e. the mean ionization potential and the shell correction, to evaluate directly the sum from the comparison with experimental data [71].

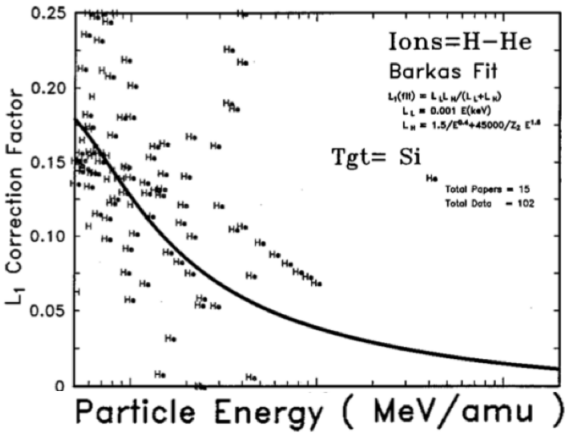

FIGURE 4.2: Barkas correction for He and p in Silicon.

following in "The low limit of the theory: particle neutralization".
The Barkas correction can be evaluated as:

$$L_1 = \frac{L_{low} L_{high}}{L_{low} + L_{high}} \tag{4.5}$$

where $L_{low} = 0.001E$ and $L_{high} = (1.5/E^{0.4}) + 45000/Z_2 E^{1.6}$ (E in keV/u). Figure 4.2 shows the Barkas correction values for He and p projectiles in Silicon [68]. The agreement is well within the scatter of experimental data.

Bloch correction

L_2 is the Bloch correction. This is the smallest correction to the Bethe-Bloch formula, but it is still considerable for low energy ions.
Bloch studied the differences between classical and quantum-mechanical methods of evaluation of the stopping of high velocity particles [72]. He distinguished between two different types of interactions, depending on the impact parameter. At small impact parameters, the interaction can be considered as the one between two free particles, while at larger impact parameters some higher-order terms are necessary. On the whole, this correction can be evaluated adding to the Bethe-Bloch equation the term:

$$Z_1^2 L_2 = -y^2[1.202 - y^2(1.042 - 0.855y^2 + 0.343y^4)] \tag{4.6}$$

where $y = \frac{Z_1}{137\beta}$.

Relative magnitude of corrections for low energy ions and accuracy considerations

All the corrections listed above have to be considered to obtain theoretical stopping powers that correctly fit the experimental data, however not all these contributions are of the same order of magnitude.
Table 4.1, related to protons, shows the percent contributions to the total stopping number L, considering also their signs. The most important correction is the Fano term, that affects the final value for more than 90%. The density term increases with energy, while the Barkas and the Bloch ones are more important at low energies. The same message is shown by the plot in figure 4.3, that shows the weights of the

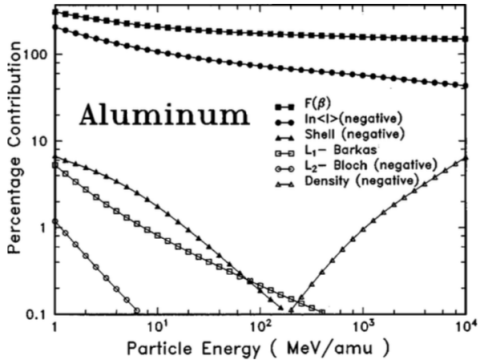

FIGURE 4.3: Contributions of corrections for Al target.

different corrections for an Al target [68].

TABLE 4.1: Percent contribution to L for low energy protons

Proton energy[MeV]	L_0	$[Shell + ln < I >]$	$\delta/2$	L_1	L_2
1	95.95	[-207]	-0.0004	5.239	-1.187
5	98.84	[-126.1]	-0.0007	1.308	-0.1479
10	99.25	[-107.3]	-0.0016	0.8124	-0.0632
50	99.7	[-80.48]	-0.0133	0.3116	-0.0101

Concerning the accuracy of the theoretical evaluation of stopping power data, the experimental values lie within 3% of the calculated values for proton and Helium ions with different targets, while the agreement for Lithium particles is within 5%.

The low limit of the theory: particle neutralization

As previously mentioned, when the incoming ion has low velocity, it captures electrons from the target that partially neutralize its nuclear charge. This possibility is not considered in the Bethe-Bloch theory, that assumes the ion charge constant. Bohr found out that the charge neutralization can be estimated by assuming that the ion is stripped of all electrons whose classical orbital velocities are less than the ion velocity. The charge change can be predicted using the formula:

$$\frac{Z_1^*}{Z_1} = 1 - exp\left[\frac{-v_1}{v_0 Z_1^{2/3}}\right] \tag{4.7}$$

where Z_1^* is the statistical net charge, v_1 is the ion velocity and v_0 is the Bohr velocity (25 keV/u) [73].

4.2.1 Stopping and Range of Ions in Matter

The Stopping and Range of Ions in Matter (SRIM) is a software package of programs that calculate the interaction of ions with matter [74]. SRIM has born in 1980, as

a program of Transport of Ion in Matter (TRIM) [75], that is even today its main core. This package of programs have been implemented by James F. Ziegler and Jochen P. Biersack, and since then it has been continuously updated. Indeed, every six years the software is upgraded with new experimental data and theoretical concepts, keeping SRIM one of the most used tool in radiation and nuclear research.
It is based on a Monte Carlo simulation that can evaluate the transport of a particle in the matter. As input, it asks the particle features (or directly the beam characteristics) and the target properties. It returns the range or the exit energy of the particle, its spatial spread around its initial direction, the concentration of vacancies produced by the beam, the sputtering rate and so on.
Moreover, the software has a database of experimental data related to stopping power of many types of particles in a large variety of targets, including compounds. It performs a fit of these data, combining it with theoretical models as the Bethe-Bloch formula, to deduce an average stopping power. The software is very useful for energy ranges where the simplest version of the Bethe-Bloch law, with the only Fano correction, can not be successfully used, as the case of protons or alpha particles with energy of a few MeV. The accuracy of the SRIM stopping power evaluations is within 4%.
However, the program has some approximation that does not allow microscopic material science studies: for example, it does not consider the crystal structure of the target (all the materials are considered amorphous, with a few exceptions as for the graphite) so the ion channeling effect is not taken into account.
In any case, the stopping power tables that SRIM can provide for low energy ion beams were very useful for this PhD research, especially in the ion beam analysis techniques called Alpha Particle Transmission and Rutherford Backscattering. These two techniques have been largely used in this PhD project to characterize the first prototypes of the NUMEN target systems. The following sections are dedicated to their description.

4.3 Rutherford Backscattering

4.3.1 A little bit of history

The name of this analysis technique is due to Ernest Rutherford. He is considered one of the Nuclear Physics fathers, since from the results of the experiments performed on a thin gold foil, he deduced the atomic structure.
Between 1909 and 1914, Hans Geiger and Ernest Marsden conducted a series of experiments on the transmission of alpha particles through metal foils [76].
They measured particles downstream the target that were clearly deviated from the beam axis. This experimental result was firstly interpreted by the two scientists as an imperfection in the alpha source used to provide the particle beam and, only under suggestion of Rutherford, led to the decision to place a detector upstream the sample. This second detector measured a certain quantity of particles that where clearly backscattered by the sample.
The plum-pudding model of the atom, then in use, described the atom as a positive region with small negative particles spread around. This model was not able to justify the alphas (positive particles) detected as backscattered by the Geiger and Marsden experiments.
This backscattered signal was interpreted by Rutherford as a big mistake in the

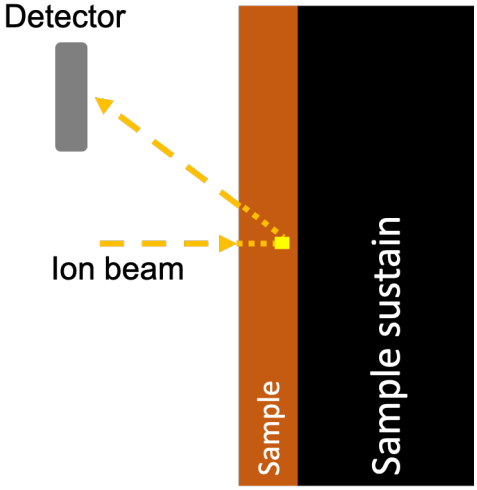

FIGURE 4.4: A schematic view of a backscattering experiment: the ion beam fires the sample and its backscattered portion is detected by a detector.

plum-pudding model: the atom had to have a positive massive (and single) particle, that can elastically collide with an alpha particle. Rutherford was outlining the atomic nucleus, laying the foundations for a new model of the atom: in 1991 he described his theory in the historic paper "The Scattering of α and β Particles by Matter and the Structure of the Atom" [77].

4.3.2 RBS measurements

The Rutherford Backscattering (RBS) technique consists in detecting ions backscattered from target atoms at a fixed angle, to analyze the thickness, the structure and the elemental composition of the target under study.
When an ion enters in the sample, it has a certain probability to undergo a coulomb interaction with a nucleus of a sample atom at a certain sample depth. If this interaction occurs, the ion (that before the collision with the nucleus lost a certain quantity of energy through coulomb interactions, depending on the crossed sample thickness) is deviated from its trajectory and, according to the kinematics laws, loses another portion of its energy (depending on the deviation angle). If the angle is such that the ion is directed backwards, the ion will lose another portion of its energy crossing backwards the sample. Therefore, in summary, the backscattered particles have lost energy in three different steps: by ionization (before the scattering), by kinematic recoil (in the scattering) and again by ionization in their return path (after the backscattering).
The residual energy of the particle can be measured by a detector placed in front of the sample, as in figure 4.4.
Usually silicon surface barrier detectors are used to detect low energy light ions used for RBS measurements. This type of detector is made of a thin (hundreds of nanometers) layer of p-doped silicon on a n-type substrate, creating a p-n junction [78]. From the particle residual energy and the angle of detection, the depth at which the elastic collision happened can be deduced and so, looking at the maximum reached depth, the total sample thickness can be evaluated.

4.3.3 Characteristics

As previously described, the energy loss process of the detected particle has three different phases. Crossing the sample for the first time, the particle loses energy for ionization; during the backscattering with the nucleus of a sample atom, the particle loses energy according to the kinematic rules of the Rutherford elastic scattering[5]; during its second crossing of the sample, this time directed to the detector, the backscattered particles lose again energy by ionization. While the energy loss by ionization is significant when crossed samples are made of heavy elements, during the elastic scattering the energy loss is the smaller the heavier are the sample atoms. This fact means that, if the sample (or its sustain) is made of an heavy element, the backscattering measurements are to be preferred to the transmission ones in studying thick samples.

One of the advantages of the RBS technique is that the study of the sample is not influenced by the contribute of the sample sustain, since particles that have been backscattered in the sample are easily discriminated from the ones that arrived to the sustain and then have been backscattered. Obviously, the essential precondition is that sample and sustain are made of different materials.
Since the kinetic calculations of the energy of a backscattered particle depends strongly on the mass of the target nuclide, RBS spectra allows to clearly distinguish between particles backscattered in different layers. This capability is crucial also in studying samples made of several different layers. NUMEN targets lie in this case study: the target deposition is made on a HOPG substrate and, in some cases, a buffer made of another element (as Chromium or Bismuth) is deposited before the target to facilitate the target deposition adhesion. Even if the thicknesses of these two (or three, in case of a buffer) layers are not known, a separated and well discriminated thickness evaluation can be done for each layer, performing a single RBS measurement of the whole sample.

Thickness evaluations are performed with beams of light charged particles, as alphas and protons. To study the thickness of thin samples with high precision, it is necessary to have a high stopping power, to observe a considerable energy loss of the beam inside the sample. For this reason, the beam energy must not exceed a few MeV, and an alpha beam should be preferred to a proton beam to study a very thin layer. Proton beams are used when the thickness of the sample is larger, but the requirement on the accuracy of the thickness evaluation is not very stringent.
It must be carefully verified that there are not other types of reactions between beam and target that can constitute a background source. A common example are the nuclear resonances: for instance, when using a low energy proton beam on a carbon target, a peak appears in the energy distribution of the backscattered protons, due to a nuclear resonance at 1.7 MeV in the interaction between a Carbon nucleus and a proton of the beam. In these situations, the beam energy must be changed and shifted to avoid the resonance energy.
Figure 4.5 shows a schematic example of RBS energy spectrum, to better understand how the information on the sample are extrapolated. Here a sample made of a 400 nm Tellurium deposition on a 5 μm thick HOPG substrate has been supposed, fired by a 2.2 MeV proton beam, detected when backscattered at 150°. The right part of the spectrum is related to the Tellurium deposition, fired by the beam first, while the

[5]The mathematical calculation of the kinematics of the scattering is deeply described in Appendix A.

left contribution is the one related to the graphite substrate.
The right edges of each contribution are due to the kinematic scattering between the beam and the sample layer (target or substrate): the beam is backscattered at the layer surface, without crossing it, so the energy loss is only related to the backscattering collision. These edges are called *kinematics edges*. Since the backscattering energy is well established by the kinematics, there are no reasons for a spread of the right edge around the predicted energy value: the edge should be perfectly vertical. If it is not, the slope is due to electronics noise of the acquisition chain.
In each contribution, on the left of the kinematics edge, the spectrum shows a plateau, which is usually leaning due to the beam attenuation while crossing the layer. This part is due to the particles that enter in the layer and, after crossing a certain thickness, are backscattered and returned to the detector.
Going on in observing the RBS spectrum from right to left, each layer contribution has a left edge. This edge corresponds to the particles that have crossed all the layer and, at the end of the layer have been backscattered to the detector. The slope of this edge is influenced not only by the electronics noise, but also by the layer thickness uniformity. Indeed, if the layer has not the same thickness in all the surface fired by the beam, it is possible that some beam particles see a certain total thickness, while others meet the same thickness plus a bump and lose a little bit more energy. This non-uniformity causes slightly different final energies of the backscattered particles, resulting in a slope of the left edge. Even if this slope is related to the thickness non-uniformity, it is not trivial to desume a quantitative estimation of the non-uniformity from the RBS spectrum since also other effects contribute to this slope (as the electronics noise, but also the beam attenuation). To perform this study, complex simulations are necessary: there are dedicated software able to perform these evaluations, as SIMNRA [79], but this type of research is not of interest for our purpose.
After crossing the first sample layer, the beam not already backscattered meets the underlying substrate. A portion of the beam is immediately backscattered at the substrate surface; if the mass of the nuclei of the first thin layer is consistently heavier than the mass of the substrate nuclei, the energy separation between the two parts of the spectrum is big (as in figure 4.5) since the energy losses of the projectile in the elastic backscattering with the first layer and with the substrate are consistently different.

The average layer thickness can be derived by the left edge of its contribution to the RBS spectrum. Since the edge is not perfectly vertical, the average energy can be assumed as the energy of the projectile that has crossed the whole layer and has been backscattered at the end of the layer thickness. Remembering that the Bethe-Bloch law can not be used in the typical energy range of the beams used for RBS, SRIM experimental tables of stopping power have been used.
I implemented a code in the C++ programming language, using the CERN framework called ROOT [80], that determines the suitable stopping power according to the projectile energy[6], and then from the exit energy of the projectiles and the detection angle returns the sample thickness. The thickness desumed from a RBS spectrum is always an average thickness, since it is calculated from an average energy. This code allows a quick on-line thickness determination, while the RBS spectra are acquired, and has been used for the data takings in INFN-LNL.
The channel of the *kinematic edge* is always checked, online and then offline when

[6]Since the SRIM stopping powers at low energies are experimental tables, to determine the stopping power at a certain projectile energy the interpolation between the closer table values has been done.

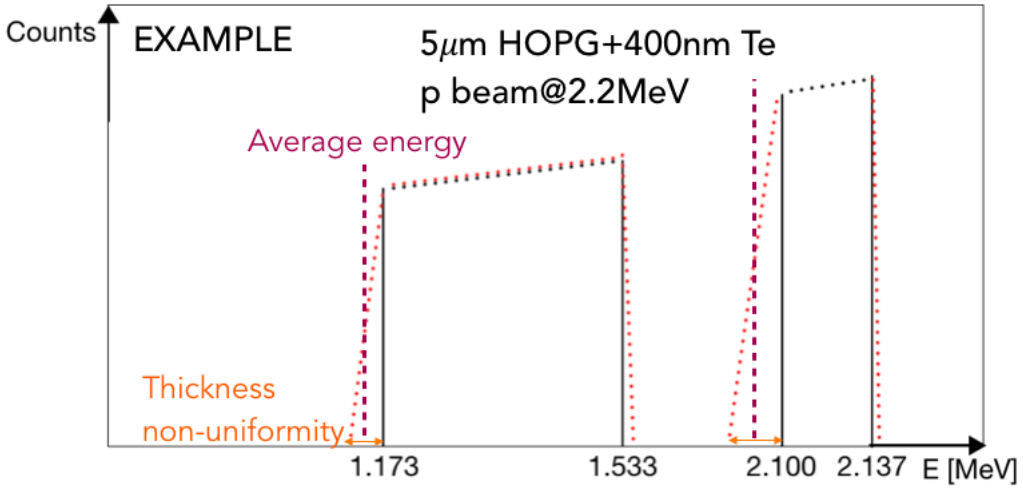

FIGURE 4.5: A schematic example of an energy spectrum acquired with RBS measurements performed with a 2.2 MeV proton beam on a sample made of a Tellurium target (400 nm thick) on a HOPG substrate (5 μm thick). The backscattered beam is detected at 150°.

the complete spectrum has been acquired, to verify that the energy calibration is still correct and no electronics or beam drift happened.

4.3.4 The RBS study on the NUMEN target prototypes

During my PhD, I was the main responsible of the RBS analysis on the first NUMEN target prototypes produced in Torino. This type of analysis has been performed systematically on the prototypes, since it can provide a lot of information that are complementary to the ones collected with Alpha Particle Transmission studies (described later).
The RBS results on the NUMEN target systems will be shown in Chapter 6. These measurements have been performed in the INFN laboratories of Legnaro (INFN-LNL), at the accelerator AN2000. This facility provides proton and alpha beams with energies up to 2.2 MeV and 2 MeV, respectively.
For our purpose, we used an alpha beam of 2 MeV to study the target depositions, since the accuracy on the deposition thickness determination is crucial. This beam is particularly useful also to detect the buffer deposition, when present, that is usually around 10 nm thick. The proton beam has been exploited at 2.2 MeV to study the HOPG backings, thicker than the target depositions.
Both alpha and proton beams have a circular spot with diameter of around 1 mm; the beam position has been checked before every data taking by firing a graph paper placed on the samples sustain. The graph paper can be seen in the right photograph of figure 4.6.
The beams have been detected at 150° or 160° from the beam line, with an AMETEK ion-implanted silicon detector.
Figure 4.6 shows pictures of the AN2000 scattering chamber. The picture on the left is the scattering chamber, with the rings for the movement of the sample holder in the three axes. The picture on the right shows one side of the sample holder: samples are pinched with thin clips and the point to be analysed can be determined through the graph paper. The two samples in the picture are two of the NUMEN target prototypes, clamped in aluminium holder of external diameter of 2.5 cm. Four NUMEN

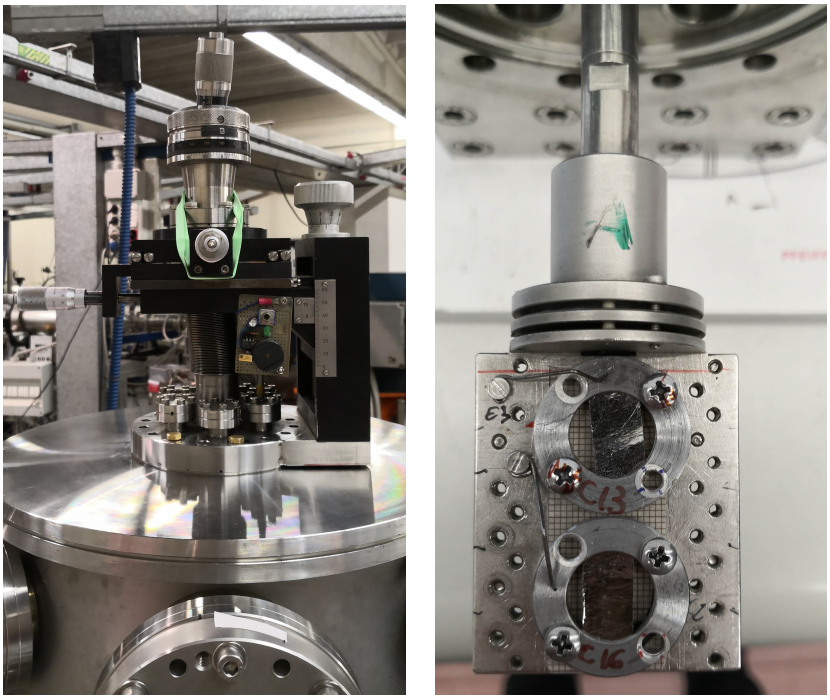

FIGURE 4.6: On the left: the AN2000 scattering chamber on the 160° line. On the right: one side of sample holder with two NUMEN target prototypes.

samples can be placed in the same time in the scattering chamber and then fired by the beam one at a time (thanks to the possibility to move vertically and horizontally the holder without breaking the vacuum). This reduces considerably the dead time for the vacuum operations.

Before every data taking, an energy calibration has been performed, acquiring the RBS spectra of samples whose chemical composition was well known. Through the determination of the channel of the *kinematic edge*, the calibration channel-energy can per determined (since the recoil energy of the beam particle on that element is known from kinematics calculations). Usually calibration samples made of elements with different masses are used, as Silicium, Ruthenium, Copper, Titanium and Carbonium.

Figure 4.7 shows the RBS spectrum acquired with an alpha beam of 2 MeV on the target prototypes called C21, made of a Germanium deposition on a HOPG substrate nominally 2 μm thick. The average deposition thickness calculated from the left edge of the RBS spectrum results to be 355 nm. The analysis of the *kinematic* edge confirmed the Germanium composition of the target layer.

The RBS technique, however, can not easily provide information on thickness uniformity. As previously mentioned, in order to evaluate the sample thickness uniformity complex simulations of the RBS process have to be performed, including precise information on the beam and an hypothesis on the thicknesses distribution of the sample under study.

For this reason, it is very important to accompany the RBS analysis with another technique, where the beam is measured in transmission. The following section will describe the technique of Alpha Particle Transmission.

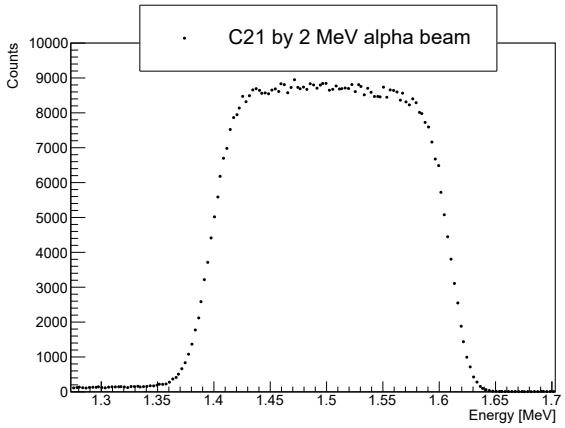

FIGURE 4.7: The RBS spectrum of the sample C21.

4.4 Alpha Particle Transmission

As the previous chapter shows, the energy measurement of the beam backscattered at a certain fixed angle by the sample gives information on the sample thickness and its elemental composition. Another type of technique involving low energy ion beams, useful to perform a study complementary to the RBS one, requires instead a detector placed downstream the target. This type of measurement detects the beam transmitted through the sample, instead of the one backscattered, and, through the evaluation of the energy lost by the beam in its crossing, provides information on the sample features.
The details reachable by the detection of the transmitted particles are related only to the sample physics, and not to its chemical features (as the elemental composition): this technique can provide accurate evaluations on the sample thickness and its thickness uniformity.
Figure 4.8 shows a schematic example of a set-up designed to perform particle transmission measurements.
The ion beam crosses the sample, losing energy mainly by ionization, and reaches the detector placed downstream the sample. The detector is usually made of Silicon as the ones used for RBS measurements since the beam energy ranges are the same to guarantee high stopping powers. The detector measures the residual energy of the transmitted beam. From the evaluation of the beam energy loss, information on the sample thickness can be extrapolated.
Since there are no interactions that cause an instantaneous energy loss depending on the particle mass, as the Rutherford scattering in the RBS process, the energy spectrum of transmitted particles do not provide separated information on the different layers of the crossed sample. For this reason, if the target under study has (as in the NUMEN case) a substrate, the thickness evaluations related to the target alone can be deduced by a two-steps sample characterization, as deeply described in the following section.

4.4.1 The Alpha Particle Transmission studies on the NUMEN target prototypes

The detection of particles transmitted through a sample represents a fundamental tool to characterize thin samples.

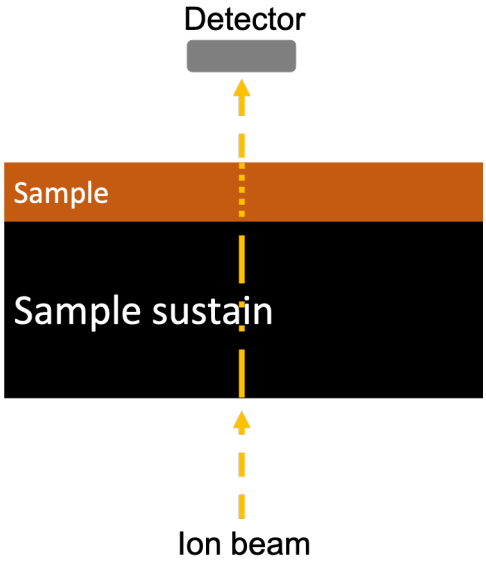

FIGURE 4.8: A schematic view of a particle transmission measurement: the ion beam fires the sample and its transmitted portion is detected by a detector.

Usually, the beams used for transmission measurements are made of light particles, as protons or alpha particles. In the case of very thin samples, as the NUMEN targets, an alpha beam must be preferred because of its higher stopping power. If the samples thickness is around a few micrometers or less, the light ion beam energy can be of the order of a few MeV. This energy range guarantees that the projectile crosses the whole sample, being then detected by a detector placed downstream the sample, but also that the energy loss is high enough to be easily determined.
Since the NUMEN target systems prototypes are small disks with a 2.5 cm diameter, a small scattering chamber is suitable. A vacuum chamber of 0.5×10^{-4} m^3 can easily host both the sample and the silicon detector, and a standard vacuum pump is able to empty the chamber until a vacuum of 2×10^{-3} mbar. Also the electronics chain for the data acquisition consists in few electronics modules, that can be hosted by a single crate. These considerations lead to design a set-up for particle transmission measurements in a small laboratory of Nuclear Physics.
If the instrumentation is host by a small academic laboratory, the only constraint is about the beam. Obviously the beam can not be provided by a big accelerator; radioactive sources can, however, successfully be used in this type of research. In this context, sources that emit alpha particles of a few MeV are the best solution, as the isotope 241 of Americium and the isotope 148 of Gadolinium.
In the Dipartimento di Scienza Applicata e Tecnologia (DISAT) of the Politecnico of Torino, the laboratory of Nuclear Physics has be organised in order to host an experimental apparatus suitable to perform Alpha Particle Transmission (APT) studies.

The apparatus

The APT measurements performed on the NUMEN target system prototypes have been performed in the aforementioned laboratory. During my PhD, I was the main responsible of this research, from the optimization of the experimental set-up to the acquisition of the measurements and the related data analysis.

The experimental set-up consists in a vacuum chamber, a silicon detector, a set of two alpha sources, a set of two collimators, a vacuum pump, an electronics chain to acquire and process the detector signals and a computer for the software acquisition. The vacuum chamber is the Model 807 of the ORTEC Company, with a volume of 0.4 m^3.
The aluminium and stainless steel chamber can be opened from above, removing the top circular part. On this removable part, there is the connector for the silicon detector, that after being screwed in this position remains in the chamber. This connector provides the detector power supply and also carries its output signal. On the lower part of the chamber, there is the connection to the vacuum pump.
The used vacuum pump is the model RV12 of the Edwards Company [81] and is placed on another table from the one that hosts for the vacuum chamber, to avoid mechanical vibrations.
In the center of the vacuum chamber, a movable support hosts the radioactive source and the sample (and, eventually, a collimator). This vertical sustain for the source and sample support has a graduated scale to measure the precise position of the support respect to the detector. The distance between the source and the detector during all the APT measurements shown in this Thesis has been mantained at 31 mm.
Figure 4.9 shows the support, that is fixed to the top of the chamber (here moved out of the chamber). On the support the ^{241}Am source is visible, while under the chamber top circular part the silicon detector can be seen. From the top, the cable for the detector power supply and its output signals comes out from the vacuum chamber.
Figure 4.10 gives another view of the apparatus, showing also the chamber connection to the vacuum pump.
The alpha beams are provided by a ^{148}Gd source and a ^{241}Am source. The first one is used only to perform the energy calibration of the apparatus, together with the Americium source. The first emits alpha particles of 3.18 MeV with an activity of 1.911 kBq, while the second emits alpha of 5.486 MeV and 5.443 MeV with an activity of 1.997 kBq. These activities allow to gather a large enough statistics in a reasonable time: to acquire an energy spectrum with around 14000 events, using a collimator between the source and the sample, one hour and a half is enough. The Gadolinium alphas energy is too low to allow them to cross the NUMEN target system, so only the Americium source is used for the thickness measurements. Since the energies of alpha particles emitted by radioactive sources are very low, the sources are not shielded and have to be handled with the appropriate attention. In any case, their dimensions are small (the diameter of the active area is 5 mm, while the entire disk is 2.5 cm in diameter), so they can be easily placed in the dedicated support of the vacuum chamber.
Two circular collimators have been used, to study different areas of the same sample: one collimator has the hole placed in the center, while the second has the hole 2.8 mm from the center. Through appropriate signs on this last collimator and on the sample, it is possibile to study four different lateral areas of each sample, rotating the collimator respect to the sample. Each mutual position is numerated, to allow a following repositioning of the collimator in the same point of the sample, to study again the sample in a following time. Figure 4.11 shows a picture of these two collimators.
The collimators have an external diameter of 2.5 cm and a hole with diameter of 2.8 mm to have a beam spot similar to the one of the NUMEN beam in Phase 4. The external dimensions of collimators are the same of source and target sample, in order to easy the displacement of the three objects in coincidence one on top of each other.

FIGURE 4.9: The internal part of the vacuum chamber, with the holder for the source and the sample, and the silicon detector.

FIGURE 4.10: The internal and external parts of the vacuum chamber, disassembled, ant the connection to the vacuum pump.

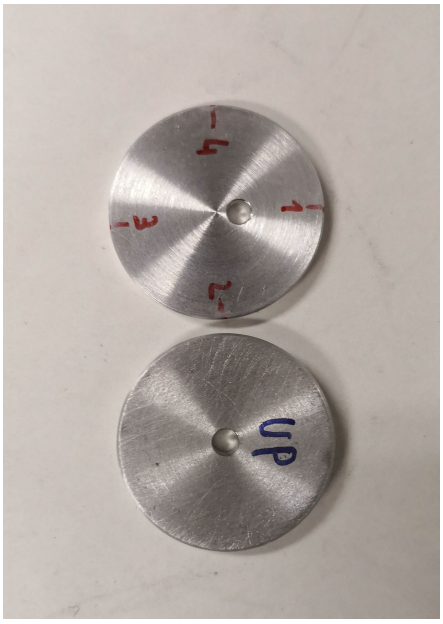

FIGURE 4.11: The two collimators used to analyse small sample areas.

The detector is a ion-implanted silicon detector of the AMETEK Company, named BU-012-050-100, with a positive bias voltage of 70V. It has an active area of 50 mm^2 and a minimum depletion depth of 100 μm. Its measured energy resolution with the electronics chain used for the acquisition, in FWHM, is around 14 keV (when detecting particles coming from the ^{241}Am source). The measurement of the detector resolution is performed before every data taking through the acquisition with the two sources without sample; these preliminary measurements are useful also to perform the energy calibration.
Figure 4.12 shows the channel related to the peak of alpha particles coming from the ^{241}Am source, in dependence on the bias voltage provided to the silicon detector. This graphic can be used as an efficiency plot: it confirms that the opportune detector bias is around 70V, as the silicon detector user manual suggests.
The detector bias supply is supplied by an ORTEC module (Model 428), with noise and ripple lower than 0.0002% and a temperature stability of $0.03\%/C^\circ$ between 0° and 50° [82].
The detector signal, extracted from the top part of the vacuum chamber, is processed by a pre-amplifier (ORTEC model 142, which details can be found in [83]).
After the pre-amplifier, the signal is processed by an ORTEC amplifier (model 575A), whose performances can be read in [84].
The acquisition is then finalized through the Multichannel Analyzer Emulation Software (MAESTRO) [85], installed on a computer fully devoted to the data acquisition. It has a user-friendly interface that allows to start and stop the acquisition and has an on-line display of the acquired events, that fill a channels-counts histogram. During the following data analysis, through the energy calibration related to the day of acquisition of that specific MAESTRO spectrum, the channels histogram is converted in an energies histogram. This energy spectrum is studied for the thickness evaluations, as explained in the following.
Figure 4.13 shows a schematic view of the whole set-up of APT instrumentation.
It has been observed that the energy resolution of the detector is sensitive to the environment temperature, because the electronics chain for the detector data acquisition is probably sensitive to it. Figure 4.14 shows two graphics that report the

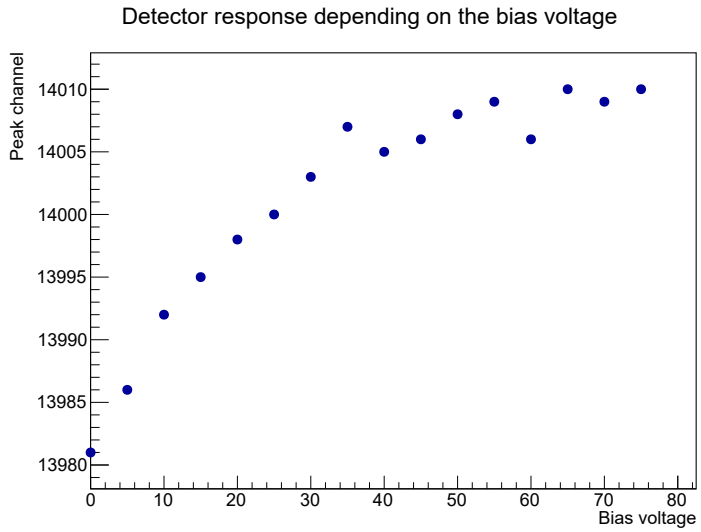

FIGURE 4.12: The channel peak of the Americium alphas in dependence on the voltage bias.

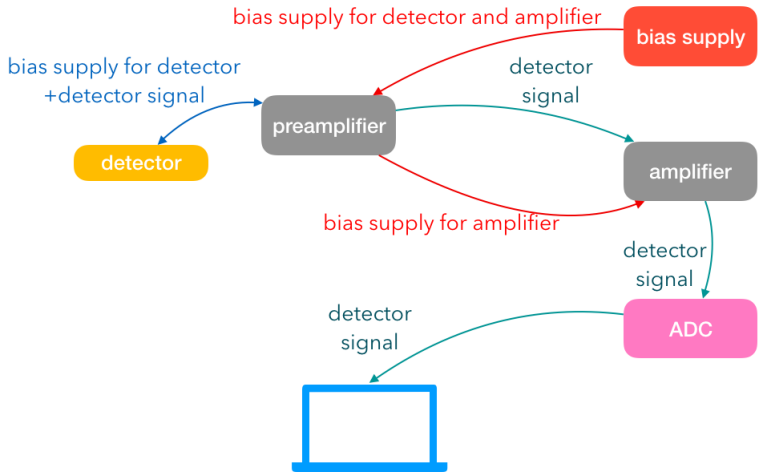

FIGURE 4.13: Sketch of the APT instrumental set-up.

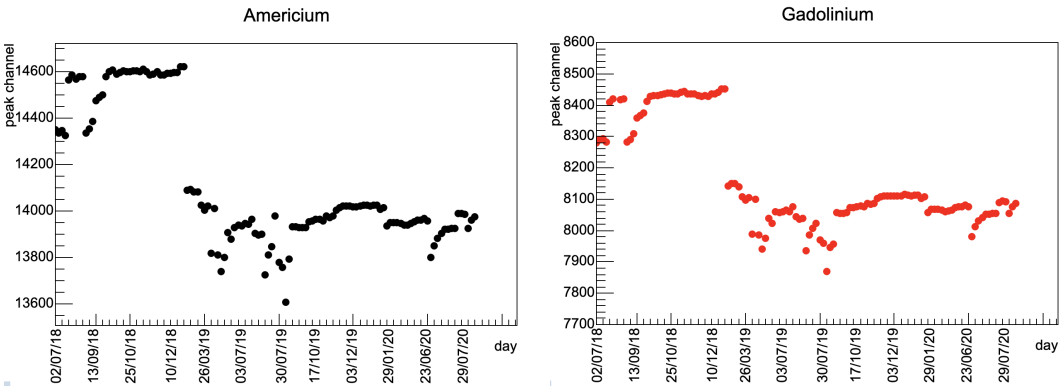

FIGURE 4.14: Americium and Gadolinium peak channels in a time span of three years.

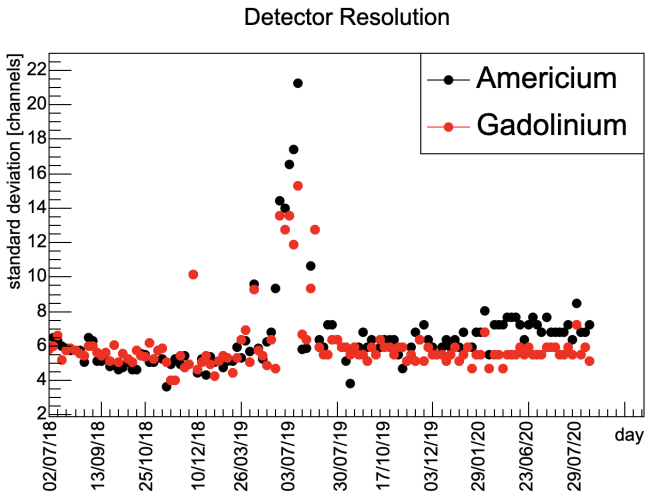

FIGURE 4.15: Sketch of the APT instrumental set-up.

channel related to the main emission peak, for each source, depending on the day. These graphics highlight an oscillation in the detector performance. For the first operational period of the detector, from July 2018 to December 2018, the peak channels of both the sources where higher than the value measured from February 2018, due to a change in the amplifier gain. During the summer seasons, probably when there is an abrupt temperature increase, the peak channels are lower and tend to stabilize when the room temperature is more stable. Observing the graphic of figure 4.15, that report the standard deviation of the main peak of the two sources[7], depending on the day, it can be observed that in July 2019 a big perturbation occurred. This abrupt change has not an equivalent in the peak channels of 4.14, so probably there was not a big shift in the channel axis, but only a broadening of the peaks. The reason is not clear and probably was not only related to a temperature increase (since in summer 2018 and 2020 this strange behaviour was not detected); maybe an electromagnetic noise from a near laboratory contributed.

[7]The energy peak of the source spectrum can be fitted by a Gaussian function. From the fit, the standard deviation can be extrapolated as estimator of the peak spread (due to the detector and electronics chain noise)

The procedure to study the NUMEN target prototypes

As previously explained, the NUMEN target prototypes are very particular samples, made of different layers that have to fulfil more or less strict requirements on the thickness and thickness uniformity.
To satisfactorily analyse these special target systems, I've worked to design an APT procedure that leads to a complete characterization of the sample. Indeed it must be highlighted that my PhD research has been an R&D study, needed as pioneer to outline a characterization procedure that the INFN-LNS laboratories (that will produce the NUMEN targets with the needed isotopes during the Phase 4) could use to analyse the targets before submitting them to the ion beams. The design and optimization of this type of study will be transferred to the INFN-LNS laboratory, as a consolidated method to get accurate informations on the physics features of the NUMEN target systems.
The whole study of the target prototypes will proceed through 3 steps: the energy calibration, the energy distribution measurement and the thickness and uniformity measurement.

The energy calibration

As previously mentioned, before the first data taking of the day the energy calibration is performed.
Spectra with only the source (once the ^{241}Am and once the ^{148}Gd), without any sample, are acquired. Through the evaluation of the peak channel, since the alpha energies of the two sources are well known, the calibration can be performed.
Depending on the room temperature and, maybe, on the electromagnetic noise due to the instruments used in the near laboratories, the peak channels can slightly shift or widen. For this reason the energy calibration has to be checked every day.
Figure 4.16 shows the APT spectra of the two sources, before the calibration. The source peaks should be lines, since each emission is monochromatic; the peak spread is due to the electronics noise of the acquisition chain. This spread can be an estimator of the error due to the noise: assuming the main Americium and Gadolinium peaks as gaussians and fitting them, the peak standard deviation σ_{noise} can be derived. The standard deviation σ_{noise} is extremely important in the determination of the sample thickness non-uniformity, as explained in the following.
Figure 4.16, for example, shows the calibration procedure performed on November 19^{th} 2020. The σ_{noise} have been estimated as 6.4 keV for Americium and 4.7 keV for Gadolinium[8].

The energy distribution measurement and the thickness determination

After the calibration procedure, the thickness measurements can be performed.
Before the target deposition, the substrate alone must be studied in order to subtract its contribution when the entire target system (target+substrate) will be produced but only the target features will be subject of study.
As an example, in the following we report the plot of 4.17, which shows the APT energy spectrum acquired with a substrate of HOPG nominally 2 μm thick. This HOPG layer has been prepared and studied to be the substrate for a Germanium deposition, named C21. Here the collimator with the central hole has been used.

[8]This difference in the peaks width is related to the slightly different detector response at different energies.

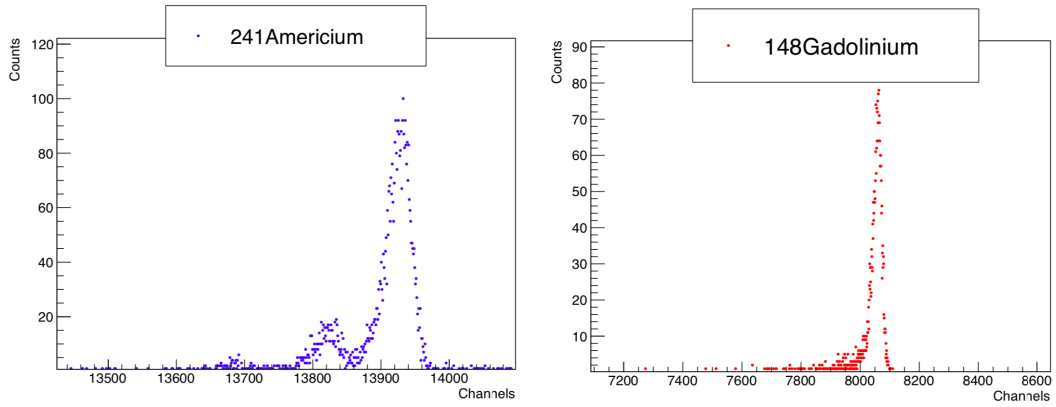

FIGURE 4.16: Americium and Gadolinium APT spectra.

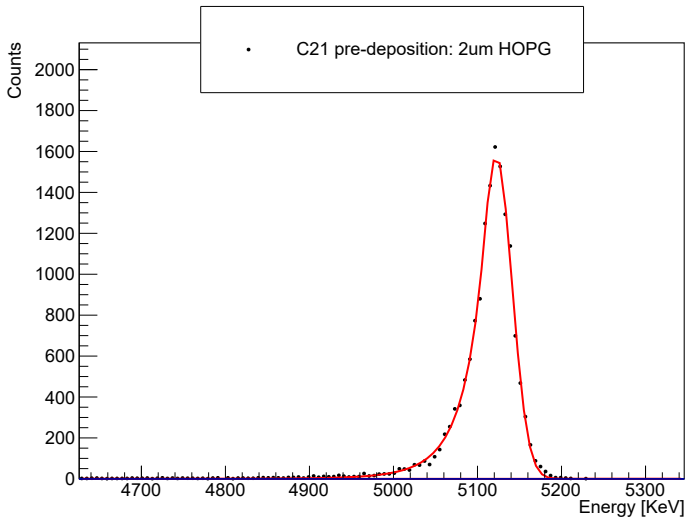

FIGURE 4.17: The C21 APT analysis before the target deposition.

The black points are the experimental data, while the red line is a Crystal Ball fit. The Crystal Ball functions $f(x;\alpha,n,\bar{x},\sigma)$ [86] are the best solution to fit the APT distributions, that have an asymmetric gaussian-like shape. This functions family has been developed by the scientific collaboration of the Crystal Ball experiment at CERN to describe a wide range of energy loss processes in high energy physics. The Crystal Ball functions have a gaussian core and a power-law tail and depend on four parameters; equations 4.8 give their formulation.

$$\begin{aligned} f(x;\alpha,n,\bar{x},\sigma) &= N\, e^{-\frac{(x-\bar{x})^2}{2\sigma^2}} \quad \text{for} \quad \frac{x-\bar{x}}{\sigma} > -\alpha \\ f(x;\alpha,n,\bar{x},\sigma) &= N\, A \left(B - \frac{x-\bar{x}}{\sigma}\right)^{-n} \quad \text{for} \quad \frac{x-\bar{x}}{\sigma} \leq -\alpha \end{aligned} \tag{4.8}$$

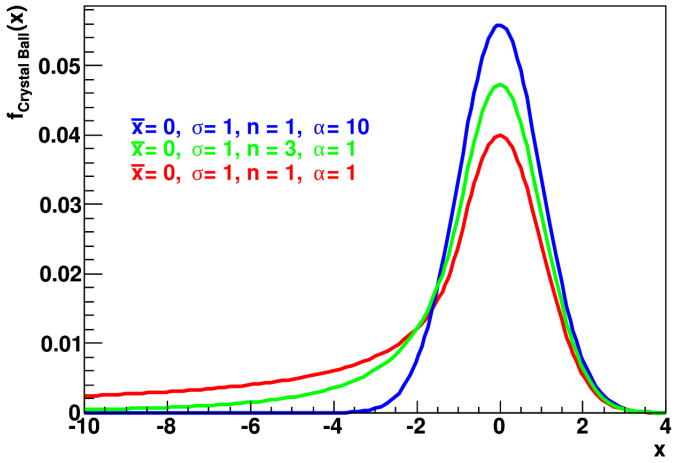

FIGURE 4.18: Examples of Crystal Ball functions changing the parameters.

where the parameters are given by formulas 4.9, being *erf* the error function.

$$
\begin{aligned}
A &= \left(\frac{n}{|\alpha|}\right)^n e^{-\frac{|\alpha|^2}{2}} \\
B &= \frac{n}{|\alpha|} - |\alpha| \\
N &= \frac{1}{\sigma(C+D)} \\
C &= \frac{n}{|\alpha|}\,\frac{1}{n-1} e^{-\frac{|\alpha|^2}{2}} \\
D &= \sqrt{\frac{\pi}{2}}\left(1 + erf\left(\frac{|\alpha|}{\sqrt{2}}\right)\right)
\end{aligned}
\tag{4.9}
$$

Figure 4.18 shows examples of the Crystal Ball Functions, plotted changing the parameters.

Coming back to the APT spectrum, the Crystal Ball fit allows to estimate the peak energy and its spread σ. For the sample here shown, the fit converged and its outputs were 5122.45 keV for the peak energy, with an error of 0.01 keV, and 18.60 keV for the σ, with an error of 0.01 keV.

While from the peak energy the average thickness of the sample can be deduced, the σ value is extremely important to determine the thickness non-uniformity.

To extrapolate the average thickness, since the alphas energies are outside the Bethe-Bloch validity range, the SRIM stopping power tables for low energy alpha particles in graphite can be used. In order to speed this evaluation, I implemented a code, in the C++ programming language, in the CERN framework ROOT.

This code, starting from the exit energy of alpha particles, calculates the crossed

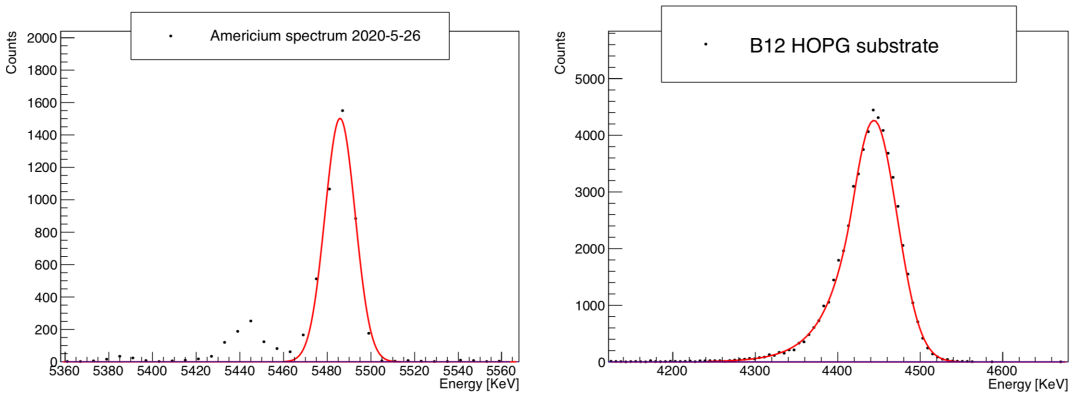

FIGURE 4.19: On the left, the energy spectrum acquired with the Americium source is shown. On the right, the spectrum related to a 5 μm thick HOPG substrate is reported. The spreads of the two peaks are different of around one order of magnitude.

thickness in the target material (specified as input of the calculation)[9].
For the present case, the thickness of the substrate of C21 is 2.130 μm.
To evaluate the thickness non-uniformity, the σ can be used. Before proceeding to the explanation of the non-uniformity calculation, it is important to make a brief digression on the detector resolution.

From the energy distribution to the thickness and uniformity distribution
Indeed, to make a correlation between the alpha energy spectrum and the sample thickness spectrum, it must be assumed that the detector resolution is good enough to assume the detector response as a Dirac delta. This approximation can be done, if the energy spread related to the detector response is at least around one order of magnitude smaller than the spread due to the sample thickness non-uniformity.
This difference is verified and can be observed in figure 4.19, where the energy distribution related to the source and the energy distribution acquired with a HOPG substrate can be observed. On the left, the spectrum related to the Americium source is shown: the $\sigma_{detector}$, estimated through a gaussian fit, is around 6 keV. On the right, the energy distribution of the HOPG substrate of the prototype B12 is shown: the peak spread σ, estimated through a Cyristal ball function, is around 40 keV. This situation is verified for all the target systems.

In the following discussion, N_α is the number of the α particles emitted by the source that pass through the sample, s is the thickness of the sample passed by the α particle, E_α is the energy of the emitted α particle, $E(E_\alpha, s)$ is the energy of the α particle after passed a thickness s and $F(s)$ is the distribution of the thickness of the (non-uniform) sample.

[9]The code calculates the energy loss by the alpha particles in the sample as a sum of small energy losses, occurred in infinitesimal spatial paths. Each small energy loss (the step is chosen as input) is determined by extrapolating from the ICRU tables (contained in the SRIM software) the stopping power related to that specific energy of the charged particle. A linear fit between two table values is performed to get the exact stopping power at that specific energy). The code starts its calculation supposing a very thin sample and evaluates the final energy of an alpha that would cross that sample. Then it compares this final energy with the real final energy given as input by the user. If the real energy is lower than the calculated one, the code updates the hypotized sample thickness to a thicker one, and starts again the calculation. When the two energies (the calculated one and the input one) are the same, or the calculated one is slightly thicker than the real one, the hypotized thickness is assumed as the real thickness of the sample. This logic procedure is the same of the code that I implemented for the analysis of the RBS spectra.

The goal here is to find the distribution $F(s)$ of the thickness of the (non-uniform) sample from the measured distribution $\frac{dN_r(E_r)}{dE_r}$ of the measured energy E_r of the α particles passed through the sample.
The number of α particles, which pass through a thickness in the range $(s, s+ds)$ of the (non-uniform) sample, is given by

$$dN_\alpha(s) = N_\alpha \; F(s) \; ds \tag{4.10}$$

Taking into account that the relationship $E(E_\alpha, s)$ between the travelled thickness s and the final energy E is bi-univocal (through the Bethe-Bloch formula or SRIM tables), we can invert this relationship into $E(E_\alpha, s) \rightarrow s(E_\alpha, E)$. Equation 4.11 becomes

$$dN_\alpha(s) = N_\alpha \; F(s) \; \frac{ds}{dE} dE = dN_\alpha(E) \tag{4.11}$$

where $dN_\alpha(E)$ represents the number of α particles, which exit from the target with an energy in the range $(E, E+dE)$.
If an α particle exits from the target with energy E, a silicon detector measures an energy E_r distributed around E with a distribution function $G_{\sigma_r}(E, E_r)$, typical of the detector. Therefore, the number of particles $d^2N_\alpha(E, E_r)$ detected with energy in the range $(E_r, E_r + dE_r)$ among the number of particles $dN_\alpha(E)$, is given by

$$d^2N_\alpha(E, E_r) = dN_\alpha(s) \; G_{\sigma_r}(E, E_r) \; dE_r = N_\alpha \; F(s(E)) \; \frac{ds(E)}{dE} dE \; G_{\sigma_r}(E, E_r) \; dE_r \tag{4.12}$$

Integrating 4.12 over all the exiting energies E, we obtain the number $dN_r(E_r)$ of α particles detected with energy in the range $(E_r, E_r + dE_r)$:

$$dN_r(E_r) = \int_{E=-\infty}^{E=+\infty} d^2N_\alpha(E, E_r) = N_\alpha \; dE_r \; \int_{E=-\infty}^{E=+\infty} F(s(E)) \; \frac{ds(E)}{dE} dE \; G_{\sigma_r}(E, E_r) \; dE \tag{4.13}$$

The distribution function $G_{\sigma_r}(E, E_r)$ of the silicon detector of the APT setup of Politecnico looks very similar to a narrow Gaussian with $\sigma_r \sim 5$ keV:

$$G_{\sigma_r}(E, E_r) = \frac{1}{\sqrt{2\pi}\,\sigma_r} e^{-\frac{(E-E_r)^2}{2\sigma_r^2}} \tag{4.14}$$

Since $\sigma_r \sim 5$ keV is much smaller than the width of the transmitted α spectra (about one order of magnitude less), the following approximation can be done:

$$G_{\sigma_r}(E, E_r) = \frac{1}{\sqrt{2\pi}\,\sigma_r} e^{-\frac{(E-E_r)^2}{2\sigma_r^2}} \sim \lim_{\sigma_r \rightarrow 0} \frac{1}{\sqrt{2\pi}\,\sigma_r} e^{-\frac{(E-E_r)^2}{2\sigma_r^2}} = \delta(E - E_r) \tag{4.15}$$

In this approximation, equation 4.13 becomes

$$\frac{dN_r(Er)}{dE_r} = N_\alpha \; \int_{E=-\infty}^{E=+\infty} F(s(E)) \; \frac{ds(E)}{dE} \delta(E - E_r) \; dE = N_\alpha \; F(s(E_r)) \; \frac{ds(E_r)}{dE_r} \tag{4.16}$$

From equation 4.16 the distribution of the thicknesses can be derived

$$F(s(E_r)) = \frac{1}{N_\alpha} \; \frac{1}{\frac{ds(E_r)}{dE_r}} \; \frac{dN_r(E_r)}{dE_r} = \frac{1}{N_\alpha} \; \frac{dE_r}{ds} \; \frac{dN_r(E_r)}{dE_r} \tag{4.17}$$

Equation 4.17 shows that the thickness distribution function $F(s)$ is equal to the measured spectrum multiplied by the energy loss rate $\frac{dE_r}{ds}$ (apart a normalization factor).

If the mean rate of energy loss (stopping power) is described by the Bethe-Bloch formula and the thicknesses are very thin, the function $\frac{dE_r}{ds}$ can be approximated by a constant and the spectrum of the detected α particles has the same shape as $F(s)$:

$$\frac{ds(E_r)}{dE_r} = cost \quad \rightarrow \quad F(s) \propto \frac{dN_r(E_r)}{dE_r} \tag{4.18}$$

In this case, the standard deviation of the thickness is proportional to the standard deviation of the spectrum and is easily calculated.
Remark: even if all the NUMEN target systems (both HOPG substrates and isotopic targets) are very thin, nevertheless the energy loss rate is not exactly constant and the $F(s)$ distribution is deformed, showing an asymmetric enhancement in the lower energy tail. This asymmetry is often masked by important non-uniformity, that even in some situations causes an asymmetric enhancement of the spectrum at high energies.

The evaluation of the thickness and uniformity of Sample C21
The Crystal Ball functions fit well the APT spectra of the α particles passed through a layer. It must be remarked that the fitted parameter σ is related to the standard deviation of the Gaussian term: it is not exactly the standard deviation of the distribution but is very close. Therefore, in the following it has been used as standard deviation of the spectrum. Nevertheless, such a standard deviation cannot be considered as due to only the non-uniform thickness. In fact, not only the thickness but also the straggling along the layer and the silicon detector resolution contribute to the broadening of the energy distribution. Since each contribution has a Gaussian shape, the following relation holds:

$$\sigma^2_{APT\ spectrum} = \sigma^2_{thickness\ non-uniformity} + \sigma^2_{detector} + \sigma^2_{straggling} \tag{4.19}$$

where $\sigma_{APT\ spectrum}$ is the σ of the Crystal Ball fit of the APT spectrum, $\sigma_{detector}$ is the detector resolution and $\sigma_{straggling}$ is the spread due to the straggling occurred in the sample[10].

As an example, the formula 4.19 applied to the case of the HOPG support of the sample C21 before the target deposition gives the following standard deviation of the energy spread due to the thickness distribution:

$$\begin{aligned} \sigma_{thickness\ non-uniformity} = \sqrt{\sigma^2_{APT\ spectrum} - \sigma^2_{detector} - \sigma^2_{straggling}} = \\ \sqrt{18.60^2 - 6^2 - 12^2} = 12.88\ keV \approx 13\ keV \end{aligned} \tag{4.20}$$

To obtain the standard deviation of the thickness distribution $\sigma_{thickness\ non-uniformity}(s)$, it is sufficient to calculate the value E' of the APT spectrum:

$$E' = E_{peak} + \sigma_{thickness\ non-uniformity} \tag{4.21}$$

and to get the corresponding value $s(E')$ of the thickness distribution. The standard deviation of the thickness distribution is the difference between the average thickness (corresponding to the average energy of APT spectrum) and $s(E')$.
In the case of the HOPG substrate of C21: $E' = E_{peak} + \sigma_{thickness\ non-uniformity} =$

[10]For the straggling evaluation, the gaussian model has been used.

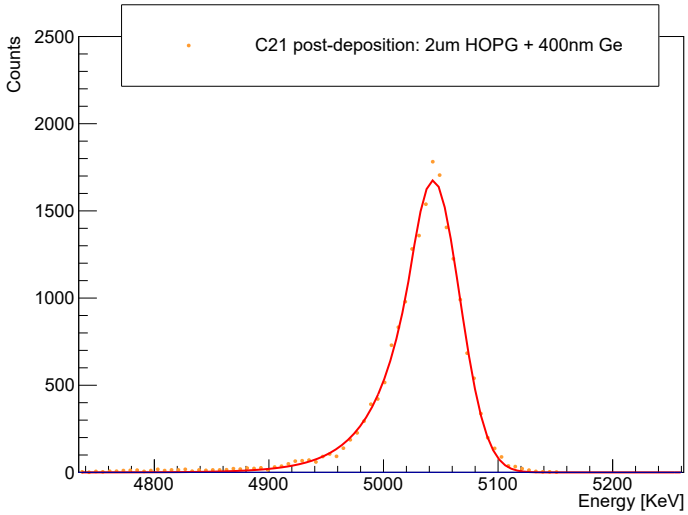

FIGURE 4.20: The C21 APT analysis after the target deposition.

$5122.45 + 12.88 = 5135.33$ keV$\approx$ 5135 keV. Now, the thickness related to an α particle coming out from the HOPG sample with this energy is 2.060 μm. From the subtraction between the sample average thickness (that is 2.130) and this value, we have the σ related to the non-uniformity in micrometers: $\sigma_{thickness\ non-uniformity} = 2.131 - 2.056 = 0.075$ μm, that is the 3.5% of the average thickness. This percentage thickness uniformity in the following will be named R_{n-u} and is evaluated as the ratio between $\sigma_{thickness\ non-uniformity}$ and the average thickness.

After the study of the substrate, the target deposition can be done. On the substrate C21, a Germanium deposition has been done, asking to the Trustech Company to deposit around 400 nm of material. The natural Germanium has been used, and not the (costly) isotope required for the DCE studies, since it was only a target prototype.
At this step, the sample C21 is made of a HOPG substrate (which thickness and uniformity have been already evaluated) and a Germanium thin layer. As previously described, the thickness and thickness uniformity of the target have to be known with good precision.
Therefore, the sample is again submitted to the alpha beam coming from the Americium source, in the APT set-up. The APT acquired spectrum can be observed in figure 4.20.
From the Crystal Ball fit, the peak energy resulted to be 5043.29 keV, with an error of 0.02 keV, while the σ resulted equal to 23.09 keV with an error of 0.01 keV.
To evaluate the average thickness of the target deposition, it is necessary to evaluate the thickness crossed by an α that enters in the sample with 5122.45 keV$\approx$ 5122 keV and exit from it with 5043.29 keV$\approx$ 5043 keV [11].
Using the same ROOT code described above, now by specifying that the crossed material is Germanium and not graphite, the target average thickness results to be 380 nm. To evaluate the thickness non-uniformity, 4.19 can be used, now modified

[11] Indeed, the target sample is placed in such a way that the HOPG substrate is the first to be crossed by the α particles coming from the radioactive source. Since the vacuum in the chamber is high, it can be assumed that there are no energy losses of the particles reaching the detector, after crossing the sample.

in order to subtract the substrate contribution:

$$\sigma^2_{target\ non-uniformity} = \sigma^2_{spectrum} - \sigma^2_{sub.\ non-uniformity} - \sigma^2_{detector\ sub.\ spectrum} + \\ -\sigma^2_{sub.\ straggling} - \sigma^2_{detector\ target+sub.\ spectrum} - \sigma^2_{target\ straggling} \tag{4.22}$$

where $\sigma_{target\ non-uniformity}$ is the non-uniformity of the target deposition, $\sigma_{spectrum}$ is the σ of the APT spectrum of figure 4.20, $\sigma_{sub.\ non-uniformity}$ is the contribute due to the substrate thickness non-uniformity, $\sigma_{detector\ sub.\ spectrum}$ is the resolution of the detector measured when the substrate APT spectrum has been acquired, $\sigma_{sub.\ straggling}$ is the part related to the straggling in the substrate, $\sigma_{detector\ target+sub.\ spectrum}$ is the detector resolution measured on the day of the spectrum 4.20 and $\sigma_{target\ straggling}$ is the uncertainty related to the straggling in the target deposition.
This calculation, considering that the spread due to the straggling in the Germanium deposition is only 7 keV, evaluates the σ due to the only target non-uniformity as 55 nm, that is the 15% of the total target thickness (R_{n-u} value).
Concerning the thickness measurements, the results provided by APT and RBS techniques on the same sample C21 agree within the 4%[12].

This type of study with the APT technique is a very important tool to get quantitative and accurate information on the thickness and thickness uniformity of the composite NUMEN target systems. Considering all the sources of error, the resolution on the thickness determination can be considered 5 nm.

In the following chapter, two microscopy analysis will be briefly described and inserted in the context of the NUMEN targets development and characterization.

[12]The agreement is evaluated as the ratio between the difference (between the two results) and the average of the two.

Chapter 5

Microscopy analysis techniques: a brief description

The previous Chapter describes how the low energy ion beams constitute a very important asset for the characterization of the thin NUMEN target systems, giving precise quantitative evaluations on thickness and thickness uniformity.
Therefore, in the context of a more complete analysis of these samples, other tools can help to get complementary informations.
Microscopy analysis can, for example, provide qualitative informations on the surface topography of the deposition: Atomic Force Microscopy and Field Emission Scanning Electron Microscopy have been used as additional analysis tools in this PhD research.

5.1 Atomic Force Microscopy

Atomic Force Miscroscopy (AFM) belongs to the family of the Scanning Probe Microscopies[1]; here only the main characteristics will be described, in [88] more details can be found. From its birth in 1985, thanks to the IBM research group, AFM is one of the most used techniques to study a sample at the nanoscale.
The AFM probe is made of a cantilever, made usually of silicon, that ends with a tip. More the tip extremity is sharp, more detailed measurements can be done: ideally, the tip should end with only an atom to reach the atomic resolution. When the tip arrives in proximity of the sample surface, it is submitted to the forces of interaction with the sample leading to a bending of the cantilever. The movement of cantilever and tip can be detected by measuring with a photodiode the reflection of a laser on the cantilever. Through the measurement of this bending, the tip movement can be derived and the sample features can be extrapolated.
Figure 5.1 shows schematically how the AFM works.
AFM can work in different operational modes: contact mode, tapping mode and non-contact mode. According to the sample and to the searched information, one is preferred to the others. In the first one, the tip is maintained in contact with the sample surface, on which is dragged; in the non-contact mode instead the tip is not in contact with the sample and the cantilever oscillates near its resonance frequency [89]. The tapping mode is instead a middle way for these two, where the tip is in a

[1]Scanning Probe Microscopy (SPM) is a type of microscopy that studies the sample surface with a physical probe, returning a scanning image of the sample made of a grid of points. Different operational modes can be used, according to the type of interaction between the probe and sample. The probe, that is a mechanical tip, can be moved on the sample with good accuracy thanks to piezoelectric actuators.[87]

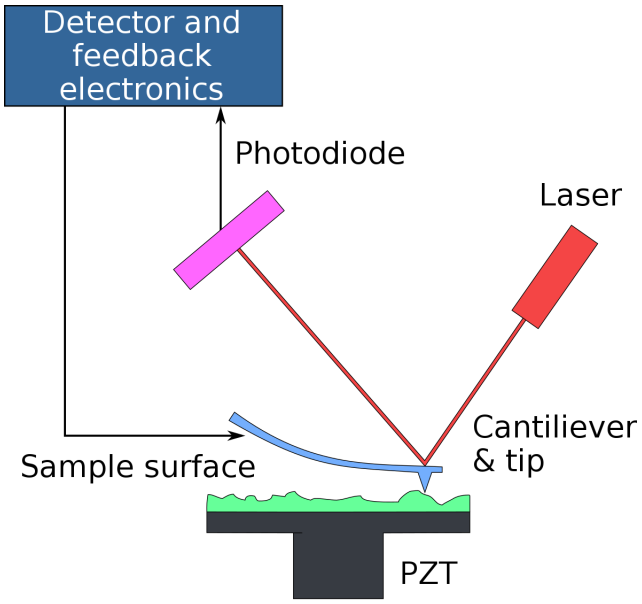

FIGURE 5.1: A sketch of the AFM operation: the tip interacts with the sample and causes a cantilever bending. The bending changes the amount of laser light reflected in the direction of the photodiode. Through the evaluation of the reflected light, the cantilever bending can be derived and so the tip movement on the sample, from which the informations on the sample are extrapolated.

intermittent contact and the cantilever oscillates up and down.
AFM can perform different types of studies [90]. It can perform force measurements, measuring the force between the probe and the sample to get, as example, information on the mechanical properties of the sample. The AFM tip can also modificate the sample, in a manipulation process, changing the sample properties (as in lithography). Moreover, AFM can provide topographic images of the sample surface, by measuring the reaction of the probe to the forces of interaction with the sample.
This last type of functioning has been used to study the surface of the HOPG samples sold by the Panasonic and the Optigraph Company, thanks to the precious help and collaboration of the Microscopy laboratories of the DISAT Department of Politecnico of Torino.
Figure 5.2 shows two AFM maps, one for a sample of HOPG 10 μm thick, sold by Panasonic, and one for a sample 5 μm thick sold by Optigraph. The surface of the thinner HOPG is undoubtedly more smooth. Actually APT measurements performed on the two types of graphite showed that the Optigraph HOPG (both the 5 μm HOPG and the 2 μm thick one) is more uniform in its whole thickness, and not only on the surface.

5.2 Field Emission Scanning Electron Microscopy

The Field Emission Scanning Electron Microscopy (FESEM) can provide information on the morphology and the elemental composition of the sample under study.
The working principles are the same of the Scanning Electron Microscopy (SEM) [91], with the main difference in the beam emission. FESEM uses a field emission gun, where a cathode is submitted to a huge electrical potential gradient, generating

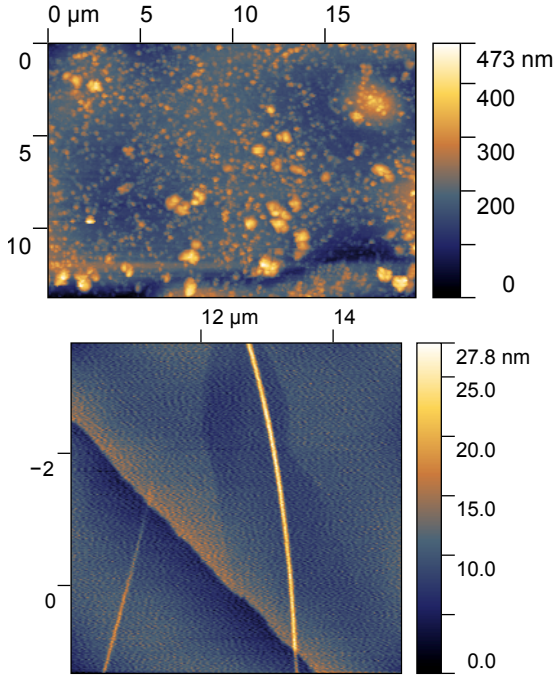

FIGURE 5.2: AFM maps of a sample of 10 μm HOPG (upper) and of a sample of 5 μm thick (lower).

the electron beam, while in SEM the electron beam is provided by heating a tungsten filament. Respect to SEM, FESEM provides more focused and energetic beams, elaborating morphology images with a better resolution.
The electron beam is focalised by a series of electromagnetic lenses and reaches the sample, located in an ultra-vacuum chamber. Depending on the chemical composition of the sample, the electron beam can penetrate more or less, causing the emission of sample electrons at different depth of the interaction volume.
Electrons emitted in the superficial region of the sample (1-5 nm) are emitted for Auger effect[2], being named *Auger electrons*. They have high energy, from 50 to 1000 eV.
Electrons coming from depths of 5-50 nm have lower energies, from 0 to 50 eV, and are called *secondary electrons*; the detection of these electrons allows to reach spatial resolution of the order of 5 nm and represents the best choice when the sample is rough and uneven, with big thickness non-uniformities.
There are also electrons backscattered from the sample: they have higher energies, around 20-30 keV, and give information on a deeper layer of the sample. Since the backscattering process depends on the atomic number of the sample atom that has backscattered the electron beam, the analysis of the backscattered electrons gives information on the elemental composition of the sample.
Lastly, also X-rays can be emitted (as atom relaxation process competitive to the Auger effect): they are useful probes of the first micrometers of the sample depth. The detection of X-rays is the heart of the Energy Dispersive X-ray (EDX) analysis, that provide a qualitative characterization of solid samples by performing an elemental analysis.

[2]When the electron beam interacts with the sample atoms, an electron of the shell K or L (the nearer to the atom nucleus) can be emitted and the atom reaches an excited configuration. Then, the atom relaxes and a more external electron goes to occupy the freed position. This process can lead to the emission of a X-ray or of an Auger electron.

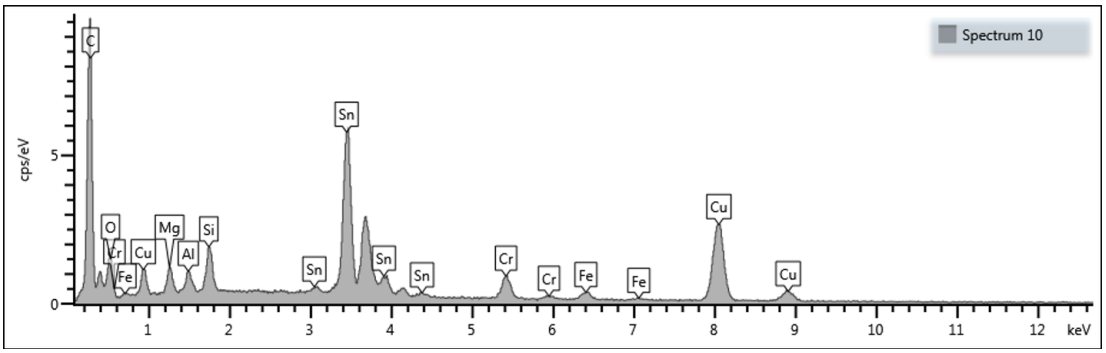

FIGURE 5.3: EDX analysis of the target prototype C8: in addition to the expected presence of Tin, Chromium and Carbonium, other elements revealed their presence, giving X-rays signals. Magnesium, Iron, Aluminium, Silicon and Copper impurities are highlighted.

Figure 5.3 shows the EDX study performed on the NUMEN target prototype named C8, that during RBS measurements revealed the presence of not expected elements. When studied by EDX, in addition to Tin (that constituted the wanted target deposition), Chromium (required as buffer layer) and Carbonium (due to the graphite substrate) other elements appeared in the plot. Magnesium, Iron, Aluminium, Silicon and Copper impurities were due to a not cleaned vacuum chamber of the evaporator, that released small tracks of these previously deposited elements.

Figure 5.4 shows two images of these impurities. The left part of each image has been acquired detecting the secondary electrons, while the right part is related to the detection of the Auger electrons. The topography shows a quite uniform deposition, even with channels of non-uniformity, with the impurities released by the chamber that lie on it.

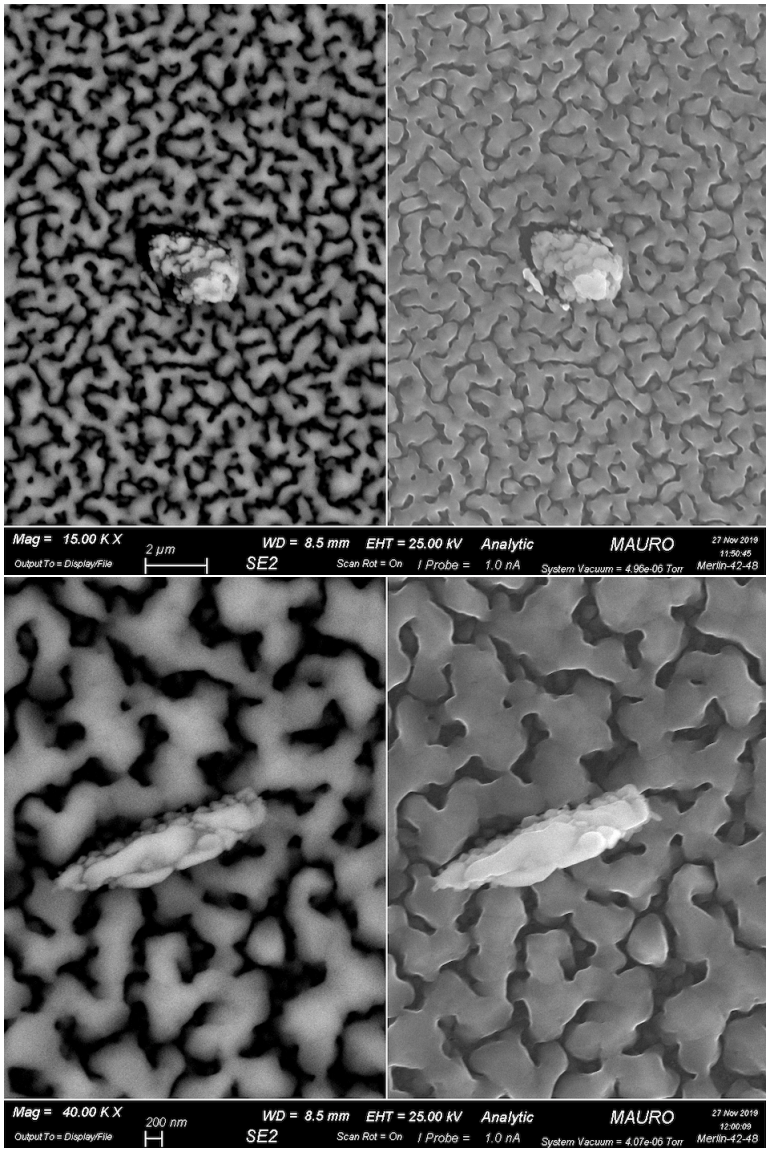

FIGURE 5.4: FESEM images of 2 regions of the sample C8, with different magnification: 15Kx (upper pictures) and 50Kx (lower pictures). The left pictures are obtained by secondary electron emission and show deep interstitial valleys (dark grooves), indicating non-uniform deposition. The right pictures are obtained by Auger electron emission and show a slighter contrast between valleys and hills, due to less penetrating electrons. Two blocks appear in the central zone, corresponding to the impurities detected by EDX.

Chapter 6

Results of the NUMEN target system prototypes characterization

As explained in the previous chapters, the goal of this PhD research was the study of the features of the NUMEN target systems in order to minimize the target effects that could affect the overall energy resolution of the Experiment. This goal led to the experimentation of different analysis techniques in order to define a complete and efficient characterization procedure for the NUMEN target systems. The pioneering research described in the past chapters fulfilled its purpose with the definition of a procedure that will be used as standard practice in the INFN-LNS target laboratory to precisely characterize each target before it is submitted to ion beams.
To arrive to this milestone, many target prototypes have been studied with the previously described analysis techniques. This Chapter will show the main results on the characterization measurements performed on the prototypes of the NUMEN target systems produced in the past three years.
In the following sections, the three main elements studied in this first R&D phase will be considered: Germanium, Tellurium and Tin. For each element, a summary of the deposition campaigns will be reported. Then, different examples of the produced target systems will be shown, spanning in the wide variety of combinations of substrate thicknesses and deposition parameters. For each target system prototype, the results gained with Alpha Particle Transmission[1], Rutherford Backscattering and microscopies will be described. Finally, the target prototype features have been used as input for the Monte Carlo code to evaluate the target effects on the NUMEN energy resolution; the output ejectile energy distributions will be shown.

6.1 Tin target systems

Tin targets will be involved in the measurements of the DCE reaction
$^{116}Sn(^{18}O,^{18}Ne)^{116}Cd$ and of all the competing channels.
Tin has been the first target element that has been studied and also the hardest one to be deposited. As described in this section, the substrate temperature and the presence of a buffer have been evaluated as possible solutions to get a uniform deposition on the HOPG samples.

[1] All the APT results shown in this chapter are the thickness evaluation performed on the central region of the target system, by using the collimator with the central hole.

6.1.1 Deposition campaigns

As described in Chapter 3, the deposition of the target layers on the substrates have been performed by Electron Beam Physical Vapour Deposition. All the Tin target prototypes have been produced with this technique, with only one exception, constituted by a deposition trial by Joule effect[2].
Table 6.1 summarizes all the Tin deposition trials performed in the past three years.

The first column reports the nominal target thickness: here the adjective "nominal" means the target thickness asked to the Trustech Company (responsible of the depositions), and not always corresponds to the real deposition thickness, as verified with the characterization measurements.

The second column reports the substrate thickness, that varied in a range between 2 and 65 μm.
The thicker graphite was the first used for the deposition trials, since it was already available in our laboratories.
Then, foils of 10 μm thick HOPG have been bought by the Panasonic Company. This type of HOPG have two drawbacks: the first one is related to the thickness, too thick to fulfil the strict requirements on the energy resolution, while the second one is related to the HOPG itself. Indeed, it is sold with ad adhesive layer on one side, since it is usually used for heat dissipation in electronics devices, where the possibility to paste the HOPG directly on the chip is appreciated. This adhesive must be removed to use the HOPG as target substrate.
A first trial of adhesive removal has been performed with oxygen plasma etching, varying the etching power and the duration of the treatments, reaching quite good results. Then a more efficient method has been found in the ultrasonic baths, that allow a uniform and fast removal of the whole adhesive layer from the graphite sheet. Using this last technique for the adhesive removal, the Panasonic HOPG have been used as deposition substrate, since in a first time the hypotized energy resolution requirements allowed a 10 μm thick substrate for the target [92]. In the end, more accurate evaluations of the energy resolution requirements led to the exclude this thick HOPG, and a thinner HOPG has been searched.
The Optigraph Company sells HOPG layers of thickness down to 2 μm, without any adhesive. For this reason in table 6.1 also depositions on 2 and 5 μm HOPG [93] are cited. Again, the substrate thicknesses here reported are nominal values, declared by the seller; each substrate sample has been characterized to get the real average thickness.

The third column shows the temperature of the substrate[3] during the deposition process. In some cases, the substrate heating can indeed facilitate the deposition adhesion, and for this reason this possibility has been investigated.

Also the fourth column is related to the deposition adhesion to the substrate, since a buffer between the two layers can overcome the atomical flatness of the graphite surface (not the ideal surface to be used as substrate). Chromium and Bismuth have been used, and the use of other elements is actually under investigation.

[2] In depositions performed with the Joule effect procedure, the target element in the crucible is evaporated by being crossed by an high current, and then deposited.

[3] This temperature is not the real substrate temperature, since the temperature reader is not located on the same plate that hosts the substrates. These temperatures values must be considered as temperature parameters used in that specific evaporator of the Trustech Company as estimators of the substrate temperatures.

The buffer element has to be chosen carefully to avoid backgrounds in the DCE measurements.

Lastly, the fifth column reports the number of trials that have been performed for each type of deposition; this number can be higher than one since many fine-tunings in the evaporation process have been made during the research.

Nominal target thickness [nm]	Nominal substrate thickness [μm]	Substrate temperature	Buffer	Number of trials
400	10 μm	120 °C	Chromium (10 nm)	1
400	10 μm	130 °C	Chromium (10 nm)	5
400	10 μm	130 °C	NO	2
400	5 μm	130 °C	Chromium (10 nm)	1
400	5 μm	130 °C	NO	1
400	2 μm	130 °C	NO	1
400	10 μm	130 °C	Chromium (10 nm)	1*
400	10 μm	135 °C	NO	1
400	10 μm	140 °C	Chromium (10 nm)	1
400	10 μm	150 °C	Chromium (10 nm)	1
400	10 μm	150 °C	NO	2
400	65 μm	150 °C	NO	1
400	10 μm	175 °C	NO	1
250	10 μm	Room Temperature	NO	1

TABLE 6.1: Deposition campaigns of Tin target system prototypes. The deposition marked with the star * has been performed by Joule effect

The full characterization of three Tin target system prototypes, deposited on 10, 5 and 2 μm thick HOPG substrates, will be shown in the following. APT, RBS and FESEM results will be discussed.

6.1.2 Target system A16

The prototype of Tin target system named A16 has a HOPG substrate nominally 10 μm thick. A deposition of 400 nm (nominal value) of Tin has been deposited by EBPVD technique, heating the substrate at 130° degree. No buffer has been used. The prototype has been fully characterized by APT, RBS and FESEM; the results are reported below.

Alpha Particle Transmission results

The procedure of APT characterization has been deeply described in Chapter 4; here only some experimental results are shown.
In figure 6.1 the APT energy spectra, acquired before (black points) and after (orange points) the target deposition can be observed, with the related Crystal Ball fits. From the fit functions parameters, the peak average energy and the peak spread can be estimated. As previously described in Chapter 4, from the energy values the thickness values can be deduced.
The HOPG substrate of the target prototype A16, nominally 10 μm thick, resulted

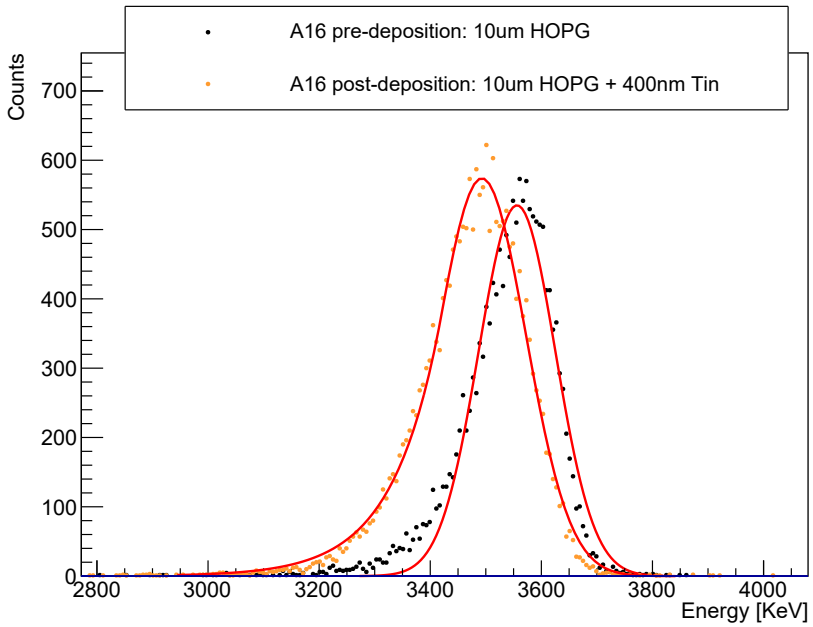

FIGURE 6.1: APT spectra acquired with the only A16 substrate (10 μm HOPG) and after the deposition with the whole target system (Tin deposition and HOPG substrate). Crystal Ball function fits of the two peaks are also shown, in red.

to be 10.080 μm thick, with a non-uniformity parameter $R_{n-u} \approx 2\%$[4].
From the comparison between the two spectra, the thickness features of the target deposition can be desumed. The target deposition, asked to the Trustech Company[5] as a layer 400 nm thick, resulted to be 220 nm thick, with a non-uniformity of 67%.

Rutherford Backscattering results

The sample has been studied also with RBS, using an alpha beam of 2 MeV, detected when backscattered at 160° degree from the beam line.
Figure 6.2 shows the energy distribution of the backscattered alpha particles. Only the target deposition contribution can be observed, since the beam energy is too low and the stopping power too high to allow alphas to arrive to the substrate and then being backscattered to the detector.
The high non-uniformity of the target, quantitatively estimated through the analysis of the APT spectra, can be immediately realized also from the quite strange RBS spectrum. Indeed the usual shape, made of two edges and a quite horizontal plateau, is here substituted by a unique decrease that from the right edge arrives to the spectrum lowest energies. From the analysis of the RBS spectrum, as explained in Chapter 4, the average thickness of the target can be calculated. In this case, the thickness estimation was complex since the usual left edge can not be clearly recognised in the spectrum. For this reason, the target average thickness has been calculated by the average energy, calculated as the average between the peak energy and

[4] As explained in Chapter 4, section 4, the non-uniformity parameter R_{n-u} is defined as as ratio between the standard deviation $\sigma_{non-uniformity}$ and the average $s_{average}$ of the thickness distribution: $R_{n-u} \equiv \frac{\sigma_{non-uniformity}}{s_{average}}$.

[5] Company that performed the deposition processes.

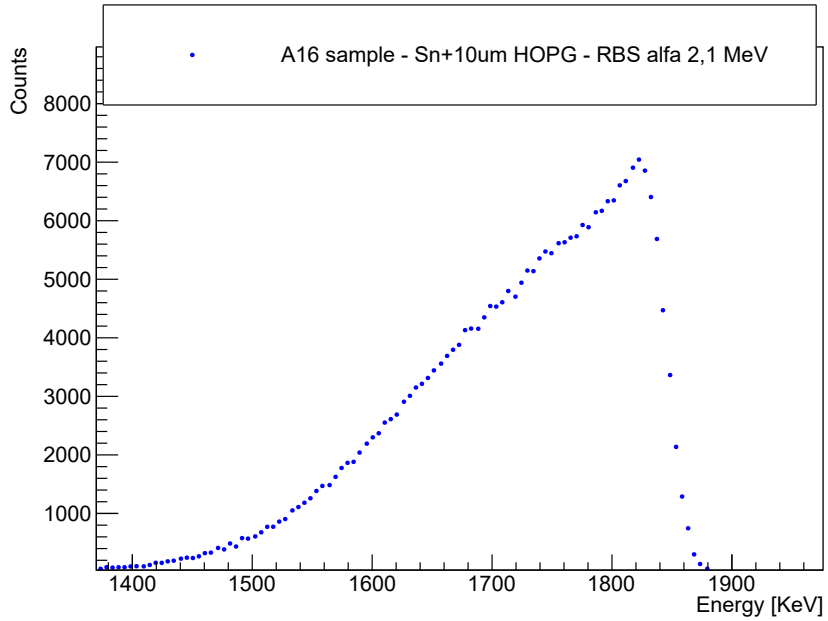

FIGURE 6.2: RBS spectrum of the target system A16, measured with a 2.1 MeV alpha beam, detected at 160° degree. The only contribution of the target deposition can be observed, since the beam energy is too low to detect also the HOPG substrate.

the spectrum lowest energy. The average thickness resulted to be 250 nm. Therefore, the agreement on the thickness results of RBS and APT techniques is of 13%; this not optimal agreement can be referred to the high non-uniformity of the target deposition, that surely affected the determination of the average thickness from the RBS spectrum.

Field Emission Scanning Electron Microscopy results

The sample has been then analyzed by FESEM, to observe the superficial roughness of the target deposition. The instrument allows to observe the sample with different magnifications; the 25K and the 100K images are reported in figure 6.3.
It can be hypotized that the non-uniformity quantified by low energy ion beam techniques can be here observed as Tin "rocks", about a micrometer in size, lying on a underlying layer of deposition made of smaller grains, with dimension of few nanometers.

Monte Carlo simulation

Figure 6.4 shows the results related to the Monte Carlo simulation run with the prototype A16 as target system. As explained in Chapter 3, section 3.3.3, this code allows to evaluate the energy resolution in the measurements of the DCE ejectile energy. In this case, the DCE reaction under study is $^{116}Sn(^{18}O,^{18}Ne)^{116}Cd$, so the ejectiles are ^{18}Ne nuclei.
The energies on the x axis are kinetic energies. The coloured gaussians are the theoretical predictions of the ejectile energies for different combinations of energy levels of ejectile and target daughter.

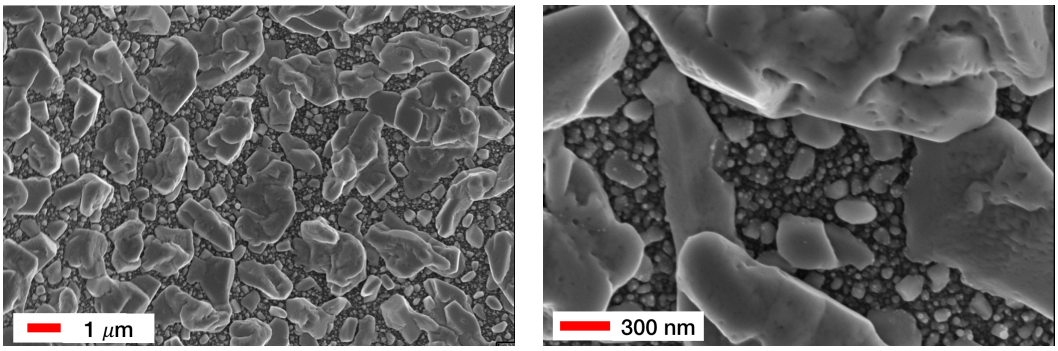

FIGURE 6.3: FESEM images of the sample A16, acquired with magnification 25k and 100k. Big structures look like stones of less than 1 μm, lying on a quite uniform deposition layer made of many small pebbles with dimensions of few nm.

The gaussians triplet at highest energies is related to the ejectile in ground state, while the gaussians triplet at lowest energies represents the ejectile in the second excited level. The red gaussian at the highest kinetic energies is related to DCE whose ejectile and target daughter are both in ground state. The blue gaussian at the lowest energes is instead referred to the DCE where both ejectile and target daughter are in the second exited level (since a significant portion of their energy is due to the excited state, their kinetic energy is lower). The black points are instead the simulated ejectile energies.
To make easier the understanding of the Gaussian plots in the following figures, the notation of colours is recalled hereafter:

1. The triplet of Gaussian curves in the high energy region represents the states couple:
   (a) Ejectile in ground state - target daughter in ground state (red)
   (b) Ejectile in ground state - target daughter in first excited state (green)
   (c) Ejectile in ground state - target daughter in second excited state (blue)
2. The triplet of Gaussian curves in the intermediate energy region represents the states couple:
   (a) Ejectile in first excited state - target daughter in ground state (red)
   (b) Ejectile in first excited state - target daughter in first excited state (green)
   (c) Ejectile in first excited state - target daughter in second excited state (blue)
3. The triplet of Gaussian curves in the high energy region represents the states couple:
   (a) Ejectile in second excited state - target daughter in ground state (red)
   (b) Ejectile in second excited state - target daughter in first excited state (green)
   (c) Ejectile in second excited state - target daughter in second excited state (blue)

The ideal situation, where an acceptable energy resolution is achieved, is a spectrum in which all the nine peaks can be easily discriminated one from each other. It is clear that the spectrum reported in figure 6.4 is not this case: for the most of the peaks, the distinction is not possible.

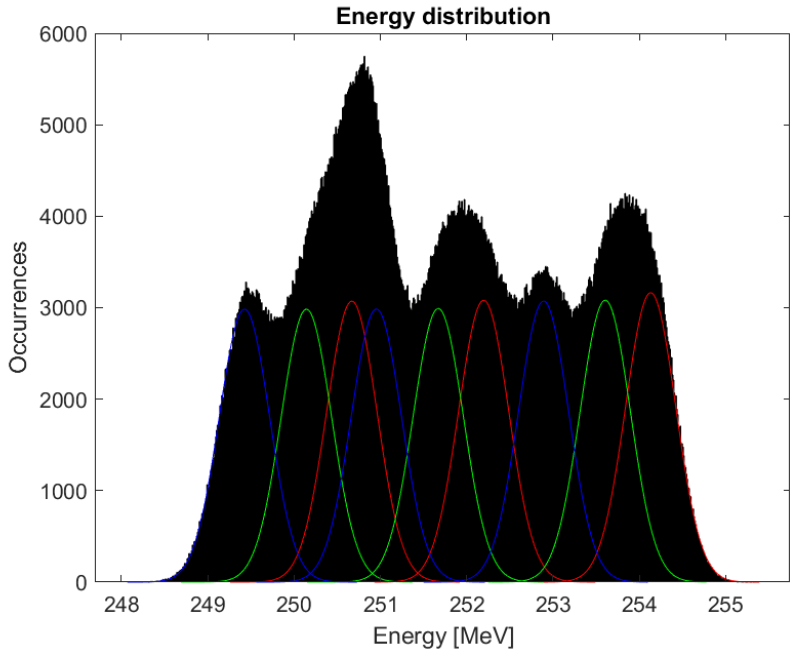

FIGURE 6.4: Energy distribution of the ejectiles of the DCE reaction $^{116}Sn(^{18}O,^{18}Ne)^{116}Cd$, using as target system the prototype A16.

This bad result is surely due to the high thickness non-uniformity of the Tin deposition, and push to study better the element deposition process.

6.1.3 Target system B4

The prototype of Tin target system named B4 has a HOPG substrate nominally 5 μm thick, with a required Tin deposition of 400 nm. During the deposition, the substrate has been heated at 130° degree. No buffer has been used.
The prototype has been fully characterized by APT, RBS and FESEM; the results are reported in the next pages.

Alpha Particle Transmission results

Figure 6.5 shows the APT study of the Tin target prototype B4. Again, the black dots are referred to the energy spectrum of the transmitted alpha particles acquired with only the substrate, before the target deposition, while the orange spectrum must be referred to the whole target system, reached after the deposition.
From the analysis of the APT spectra, the results on thickness and thickness uniformity of substrate and target have been deduced.
The substrate, nominally 5 μm thick, resulted 5.740 μm thick, with a non-uniformity of 3%.
The target deposition, asked as 400 nm, is instead 230 nm, with a non-uniformity of 68%. Again, the thickness uniformity obtained by depositing Tin on a substrate heated at 130° degree, without any buffer, is not satisfactory.
The thickness results related to this sample are very similar to the A16 ones; this analogy can be referred to the fact that the two target depositions have been evaporated simultaneously, in the same deposition process.

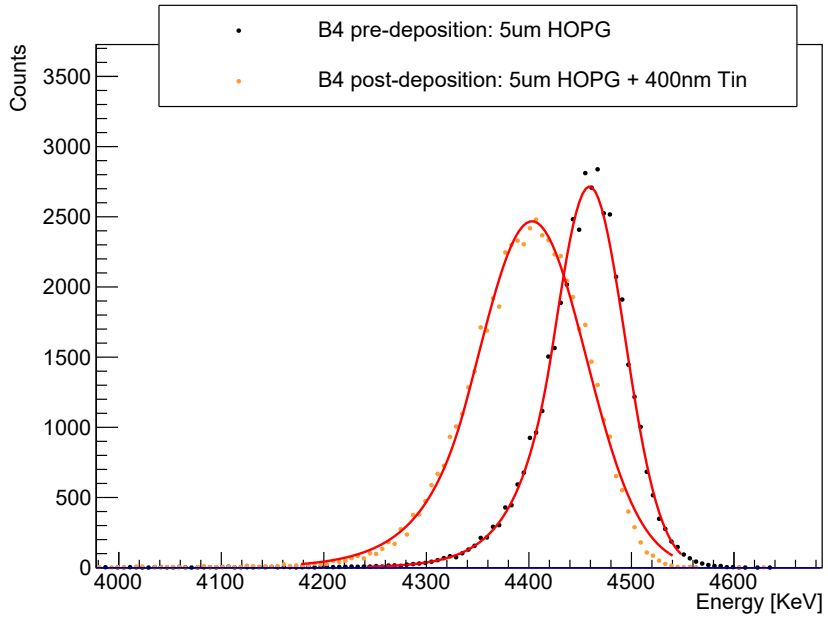

FIGURE 6.5: APT spectra acquired with the only B4 substrate (5 μm HOPG) and after the deposition with the whole target system (Tin deposition and HOPG substrate). Crystal Ball function fits of the two peaks are also shown, in red.

Rutherford Backscattering results

RBS analysis has been performed, with an alpha beam of 2.1 MeV. The backscattered beam has been detected at 160° degree.
In the spectrum of figure 6.6, the same strange shape observed in the RBS spectrum of sample A16 can be here seen, due to the high non-uniformity of the target deposition.
Therefore the average thickness has been calculated in the same way used for the RBS analysis of sample A16, and resulted to be 260 nm. The agreement on the thickness results between RBS and APT techniques is of 12%; this not good result can be again referred to the high non-uniformity in thickness of the sample.

Field Emission Scanning Electron Microscopy results

FESEM analysis has been performed on sample B4, to evaluate the deposition roughness. Figure 6.7 reports the 25K and 100K magnification images.
The results are quite similar to the ones of sample A16, since the substrate thickness does not influence the deposition. Big structures with dimensions of micrometers cover uniformly the whole sample surface. Under these structures, a quite uniform deposition layer can be glimpsed.

Monte Carlo simulation

Figure 6.8 shows the output of the Monte Carlo simulation for the energy resolution achieved using the target prototype B4.
Also in this case, as for the A16 results, the distinction between the peaks related to

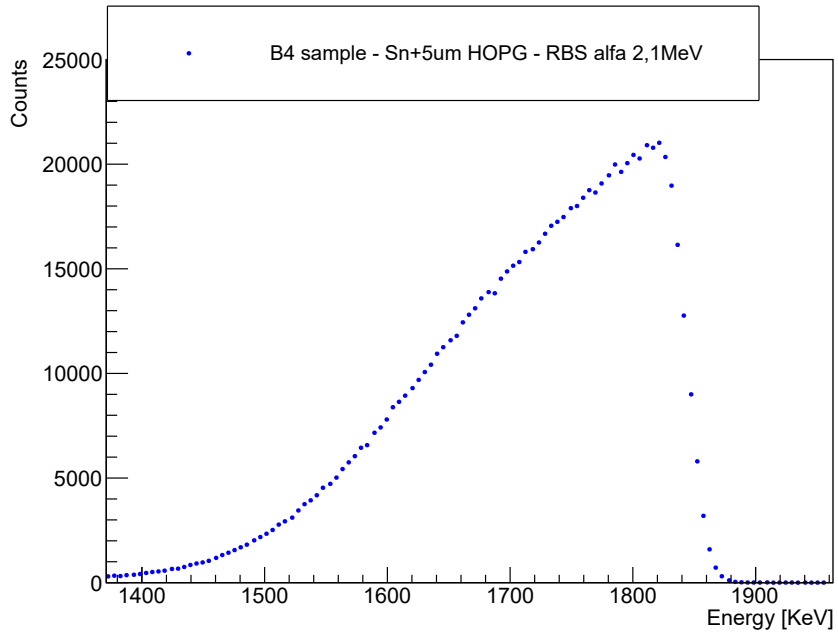

FIGURE 6.6: RBS spectrum of the target system B4, measured with a 2.1 MeV alpha beam, detected at 160° degree. The only contribution of the target deposition can be observed, since the beam energy is too low to detect also the HOPG substrate.

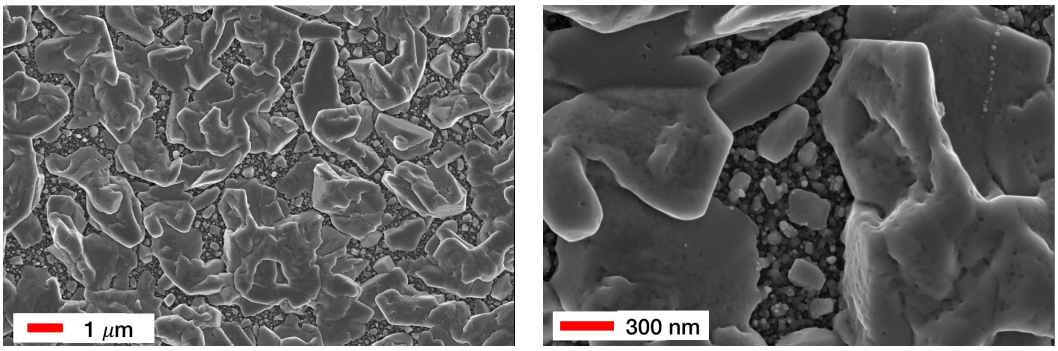

FIGURE 6.7: FESEM images of the sample B4, acquired with magnification 25k and 100k. Big structures look like stones of less than 1 μm, lying on a quite uniform deposition layer made of many small pebbles with dimensions of few nm.

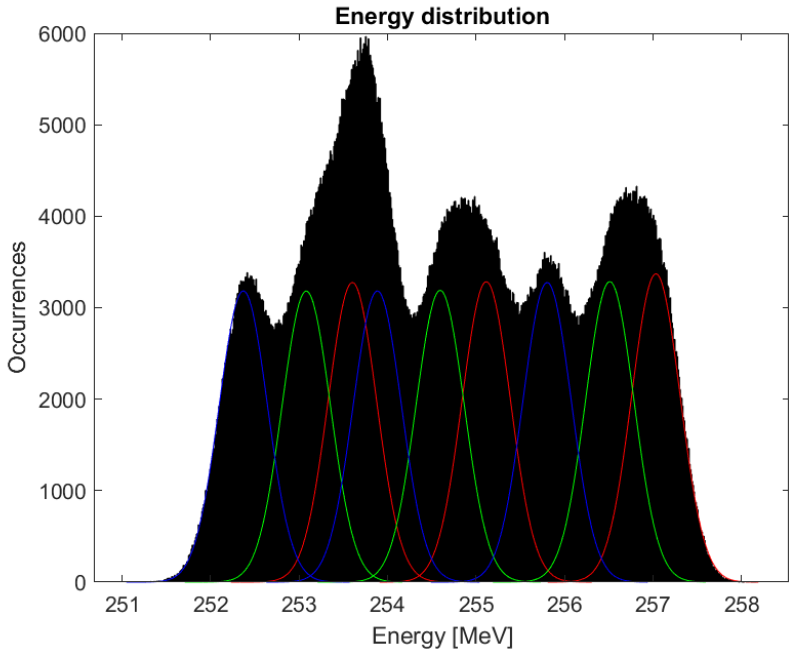

FIGURE 6.8: Energy distribution of the ejectiles of the DCE reaction $^{116}Sn(^{18}O,^{18}Ne)^{116}Cd$, using as target system the prototype B4.

the different energy levels is not easy, especially between the red one (target daughter in ground state) and the green one (target daughter in first excited level), at each ejectile energy level.
This result can be again referred to the high non-uniformity in thickness of the Tin deposition.

6.1.4 Target system C7

Sample C7 is composed of a Tin deposition (400 nm thick) on a 2 μm thick HOPG. The deposition has been performed mantaining the substrate at 130°C degree. To enhance the deposition uniformity, a buffer made of Chromium, around 10 nm thick, has been evaporated on the substrate before the target deposition.
Again, the characterization results will be presented.

Alpha Particle Transmission results

Figure 6.9 shows the APT analysis performed on the target system C7: the black spectrum is related to the only substrate, nominally 2 μm thick, while the orange spectrum has been acquired analysing the whole target system.
From the analysis of the two spectra, thickness evaluations on substrate and target have been performed.
The substrate resulted to be 2.635 μm thick, with a non-uniformity of 4%.
To evaluate the target thickness, the chromium buffer (deposited immediately before the target element) has been taken into account. The Chromium buffer thickness has been determined through the RBS analysis (shown in the following) as 40 nm thick. Considering this buffer thickness, the target resulted to be 170 nm thick, with a non-uniformity of 62%.
This percentage is slightly lower than the ones expressing the non-uniformity of target systems A16 and B4, where the Chromium buffer was not used. Probably this

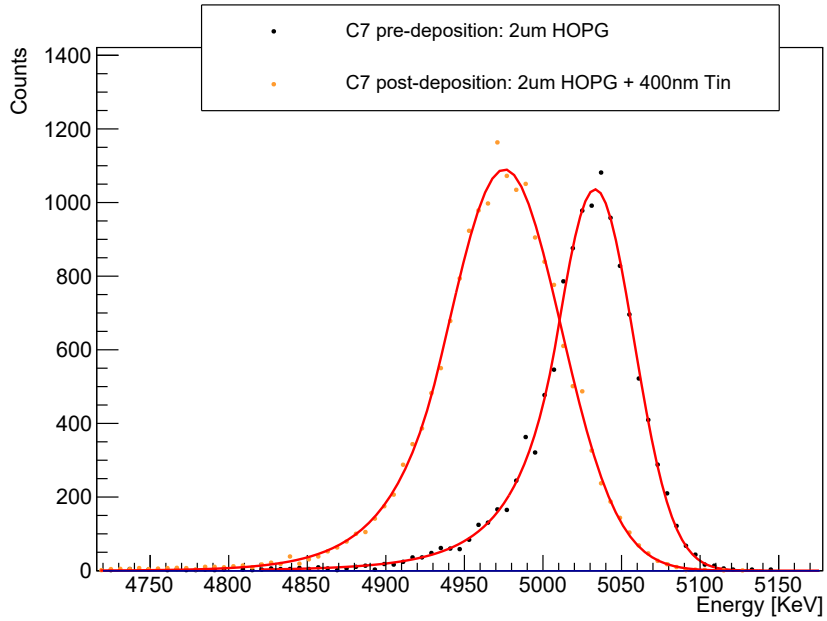

FIGURE 6.9: APT spectra acquired with the only C7 substrate (2 μm HOPG) and after the deposition with the whole target system (Tin deposition and HOPG substrate). Crystal Ball function fits of the two peaks are also shown, in red.

difference means that the buffer helps in the target adhesion and so in its uniform deposition.

Rutherford Backscattering results

The RBS technique has been exploited to study the target prototype, in particular to separately study the Chromium buffer.
In this case, in the spectrum part related to the target the usual plateau can be recognised, even if the slope of the left edge clearly highlights a high non-uniformity of the target deposition.
On the left, two wide and low peaks appear. The one nearest to the target contribution is the Chromium one, from which peak energy the buffer thickness has been deduced.
The one at lower energy is instead caused by many impurities in the deposition layer. To better understand their nature, an EDX analysis has been performed. The results are the same of the sample C8 (deposited together with C7, in the same prototypes set), reported in figure 5.3 of Chapter 5. A large variety of elements was detected, revealing that the evaporator vacuum chamber in which the Tin deposition has been performed was not cleaned.
Concerning the thickness evaluation, from the study of the left edge of the target related part in the RBS spectrum the average thickness resulted to be 160 nm. The agreement between the APT and RBS thickness results is within the 6%.

Field Emission Scanning Electron Microscopy results

Figure 6.11 shows the FESEM analysis performed on the target system C7. The FE-

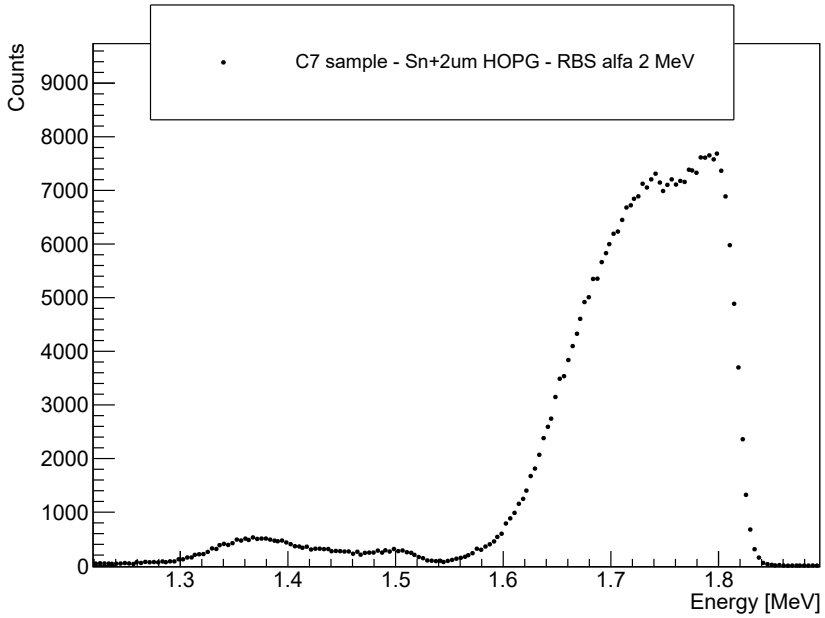

FIGURE 6.10: RBS spectrum of the target system C7, measured with a 2 MeV alpha beam, detected at 160° degree. The only contributions of target deposition and buffer can be observed, since the beam energy is too low to detect also the HOPG substrate. An additional contribute appears at lower energy, related to impurities in the deposition layer.

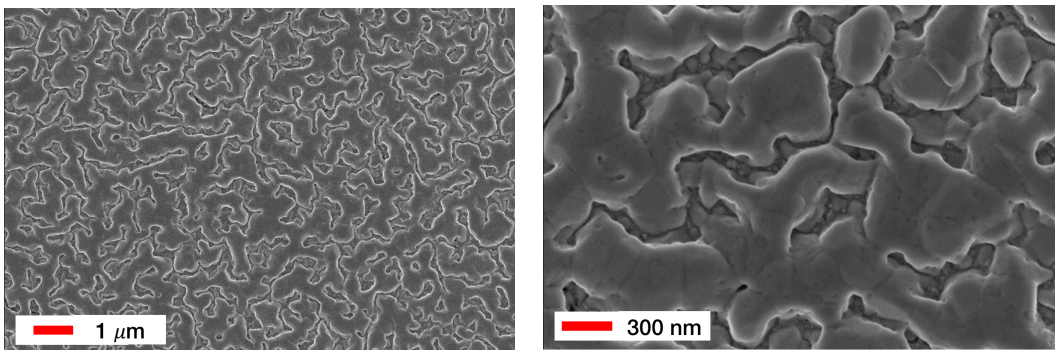

FIGURE 6.11: FESEM images of the sample C7, acquired with magnification 25k and 100k. Two different deposition layers can be observed: the superficial one, quite flat, shows channels through which the underlying layer can be observed, made of very small pebbles.

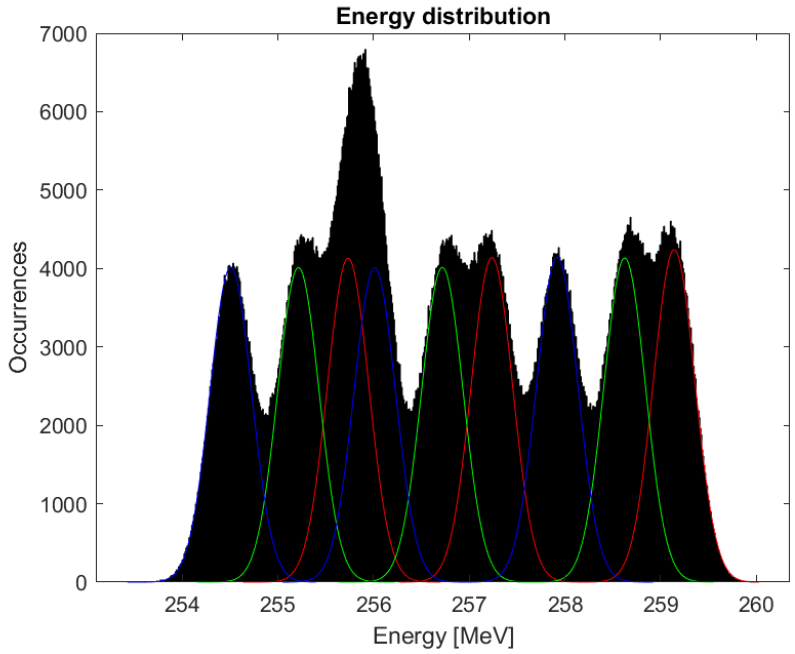

FIGURE 6.12: Energy distribution of the ejectiles of the DCE reaction $^{116}Sn(^{18}O,^{18}Ne)^{116}Cd$, using as target system the prototype C7.

SEM images show a deposition uniformity better than the ones of the previous FE-SEM studies on A16 and B4 samples. Now the big structures are joined together forming a deposition layer with channels, through which the underlaying deposition layer made of small grains can be still observed. This better result can be probably referred to the use of the Chromium buffer, and appears also in the quantitative non-uniformity evaluation measured by means of APT technique.

Monte Carlo simulation

Finally, in figure 6.12 is reported the Monte Carlo simulation performed for the prototypal target system C7. This result has been already shown in Chapter 3, now is presented again as part of the whole characterization of the sample.
Now the distinction of the different peaks is easier, even if not yet very clear in the entire tails of the gaussians related to target daughter in ground state and target daughter in first excited state. Instead it is not possible to discriminate between the DCE reaction with ejectile in first excited state and target daughter in second excited state (blue peak around 256 MeV) and the DCE exiting in ejectile in second excited state and target daughter in ground state (red peak on the left of the blue peak).
This result, even if not yet satisfactory, is better than the ones obtained with A16 and B4. One possibile reason lies in the better thickness uniformity, but surely also the thinner substrate plays a crucial role in tightening the separation of the peaks.

6.1.5 Conclusions on Tin target system prototypes

In the past three years, a lot of work has been done in the research related to the Tin deposition on HOPG substrates [94].
It resulted that the thickness of the substrate does not influence the target thickness uniformity, even if obviously has influence on the energy resolution.
A buffer should be used, maybe of Chromium, to help in the deposition adhesion

on the substrate.
In the same direction the heating of the substrate can work. Even if the reference temperatures of the Trustech evaporator can be used as precise parameters only in that specific instrument, the fact that the best deposition results have been obtained at around 130° degree is an indication of the necessity to heat the substrate at temperatures well above the room temperature.
The thickness uniformity of the produced prototypes is still not good enough to fulfil the energy resolution requirements; other buffer elements and a precise study on the substrate temperature influence will be done in the next year.

6.2 Tellurium target systems

Tellurium targets are required to measure the cross-sections of the DCE reaction $^{130}Te(^{20}Ne,^{20}O)^{130}Xe$, together with all its competing channels.
Tellurium is a material easier to be deposited respect to Tin; deposition with good uniformity can be obtained even without substrate heating or buffer.
Indeed, a punctual comparison between the deposition performed with the heated substrate and with the substrate at room temperature showed that no evident uniformity differences can be observed. Also the presence of a buffer does not influence the uniformity of the target deposition. For these reasons, the best solution is to avoid the substrate heating and the buffer evaporation, minimising two possible causes of mistakes during the deposition process.

6.2.1 Deposition campaigns

The table 6.2 summarises all the deposition parameters that have been experimented during the pioneering campaigns of Tellurium deposition.
To study the influence of the substrate temperature on the deposition thickness uniformity, different trials have been made heating the substrate at 100°, both with and without the buffer. These prototypes have been compared to prototypes evaporated on room temperature substrates. No evidences have been found of uniformity differences by heating or not the substrate, so it has been assumed that Tellurium targets can be satisfactorily deposited at room temperature, as previously mentioned.
The same can be said on the buffer use; different pioneering deposition with buffer have been performed and verified that a buffer does not considerably help the deposition uniformity.

6.2.2 Target System A14

The Tellurium target system prototype named A14 is deposited on a 10 μm thick HOPG maintained at room temperature. No buffer has been used.
As the other Tellurium target prototypes shown in this section, A14 has been deposited in the INFN-LNS laboratories.
The sample has been exhaustively analysed by APT, RBS and FESEM techniques. The results are here reported.

Nominal target thickness [nm]	Nominal substrate thickness [μm]	Substrate temperature	Buffer	Number of trials
400	10 μm	Room Temperature	Chromium (10 nm)	2
400	10 μm	Room Temperature	NO	4**
400	5 μm	Room Temperature	NO	2
400	2 μm	Room Temperature	NO	2
400	10 μm	100°C	Chromium (10 nm)	3
400	10 μm	100°C	NO	1

TABLE 6.2: Deposition campaigns of Tellurium target system prototypes. One of the depositions marked with the star ** has been performed in the INFN-LNS target laboratory, while all the other depositions have been made by the Trustech Company.

Alpha Particle Transmission results

Figure 6.13 shows the APT analysis performed on the sample A14, before (black spectrum) and after (orange spectrum) the target deposition.
To estimate the average thickness and the thickness non-uniformity, the considerations previously described have been done also in this case.
The average thickness of the HOPG substrate resulted to be 10.130 μm, with an estimated thickness non-uniformity of 3%.
The average thickness of the Tellurium deposition resulted to be 430 nm, with a non-uniformity of 6%.

Rutherford Backscattering results

Figure 6.18 shows the RBS spectrum acquired in INFN-LNL laboratory, using an alpha beam of 2 MeV. The beam was detected at 160° degree.
While the *kinematic edge* was used to verified that the deposition was effectively Tellurium, from the left edge of the spectrum the average thickness has been deduced. It resulted to be 425 nm; this result was in agreement with the APT thickness result within the 0.2%.

Field Emission Scanning Electron Microscopy results

Finally, A14 underwent a FESEM analysis. Figure 6.15 reports two images acquired with 25k and 100k magnifications.
The target deposition is quite uniform and flat; Tellurium grains can be discriminated, but their heights are small and also their in-plane dimensions are of the order of tens of nm.

Monte Carlo simulation

Figure 6.16 shows the Monte Carlo code output for the target system prototype A14. As previously explained, the goal is to have a ejectile energy spectrum that allows to discriminate among the energy levels peaks. From the spectrum it is clear that by

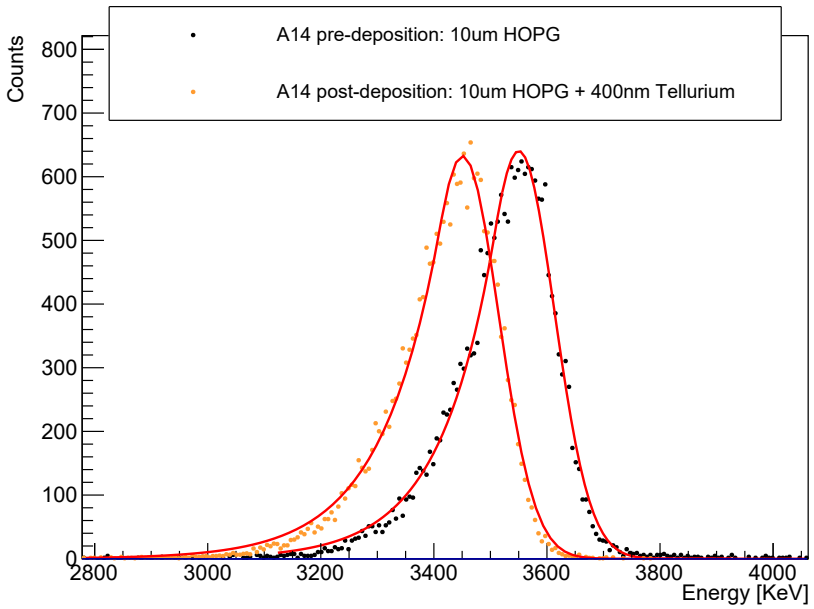

FIGURE 6.13: APT spectra acquired with the only A14 substrate (10 μm HOPG) and after the deposition with the whole target system (Tellurium deposition and HOPG substrate). Crystal Ball function fits of the two peaks are also shown, in red.

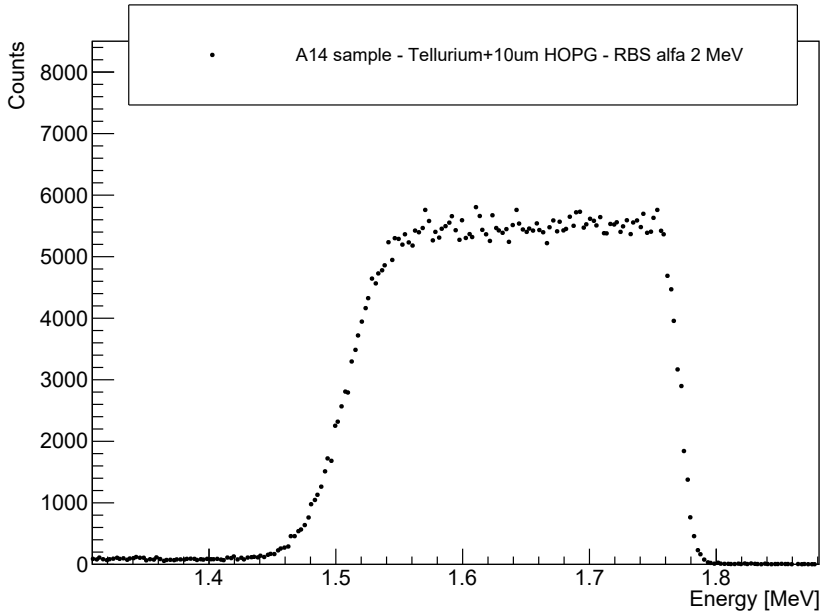

FIGURE 6.14: RBS spectrum of the target system A14, measured with a 2 MeV alpha beam, detected at 160° degree. The only contribution of the target deposition can be observed, since the beam energy is too low to detect also the HOPG substrate.

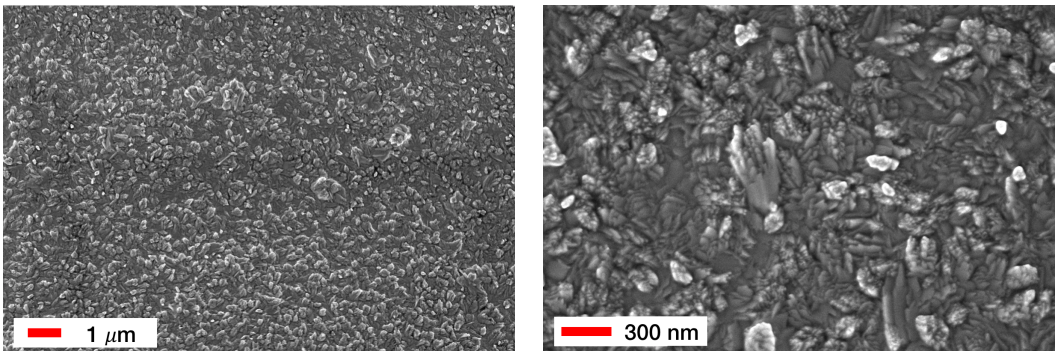

FIGURE 6.15: FESEM images of the sample A14, acquired with magnification 25k and 100k.

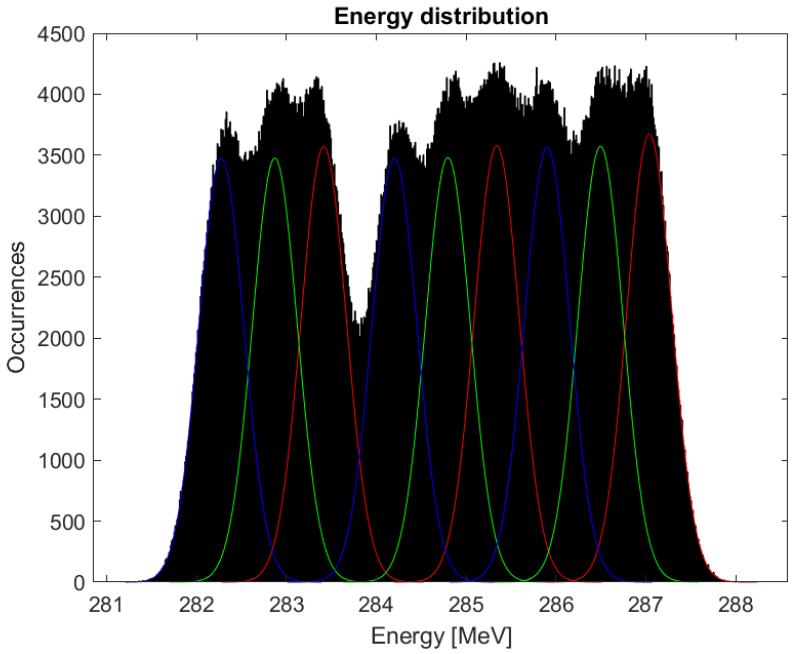

FIGURE 6.16: Energy distribution of the ejectiles of the DCE reaction $^{130}Te(^{20}Ne,^{20}O)^{130}Xe$, using as target system the prototype A14.

using A14 as target system, the required resolution can not be achieved. Probably this is due not only to the target thickness uniformity, that is under the 10%, but to the thick substrate of graphite.

6.2.3 Target System B10

The Tellurium target system prototype named B10 has a Tellurium deposition, nominally 400 nm thick, on a nominally 5 μm thick HOPG. The deposition has been performed without a previous buffer evaporation, keeping the substrate at room temperature.
In the following, the characterization is reported.

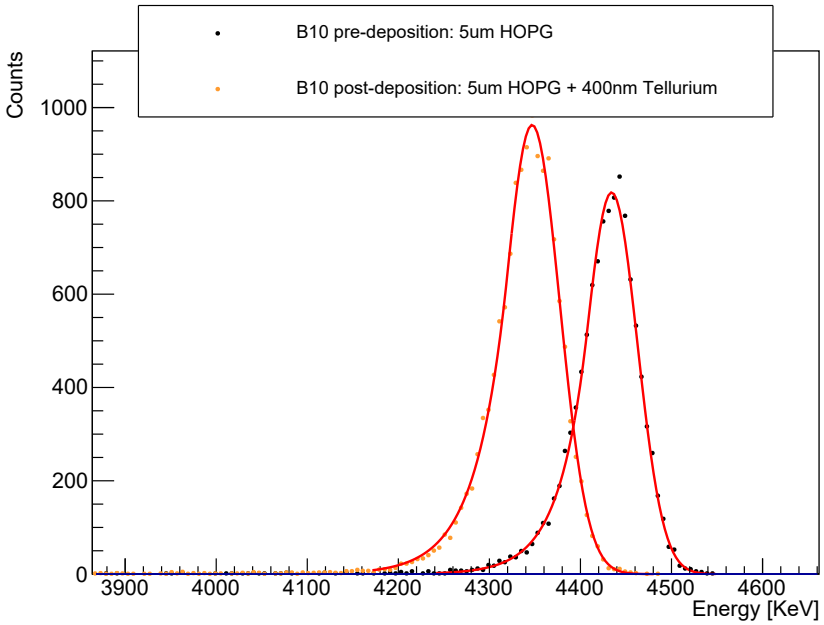

FIGURE 6.17: APT spectra acquired with the only B10 substrate (5 μm HOPG) and after the deposition with the whole target system (Tellurium deposition and HOPG substrate). Crystal Ball function fits of the two peaks are also shown, in red.

Alpha Particle Transmission results

Figure 6.17 shows the APT measurements performed on the sample B10. Again, the black energy spectrum is related to the only substrate, while the orange energy spectrum is related to the entire target system.
From the analysis of the black peak, the substrate resulted to be 5.865 μm thick, with a non-uniformity of 10%.
The target thickness features have been deduced from the comparison between the black spectrum and the orange one: the target resulted to be 435 nm thick with a non-uniformity of 11%.

Rutherford Backscattering results

Figure 6.18 shows the RBS spectrum related to the sample B10. An alpha beam of 2 MeV has been detected at 160° degree.
From the left edge, the average thickness of the Tellurium deposition resulted to be 415 nm. Therefore, the agreement with the APT thickness results is around 4%.

Field Emission Scanning Electron Microscopy results

Figure 6.19 reports the FESEM images of the deposition surface of B10. The same observations done for the FESEM images of A14 can be here repeated: the deposition seems to be quite flat and uniform (in agreement with the thickness non-uniformity estimated by APT).

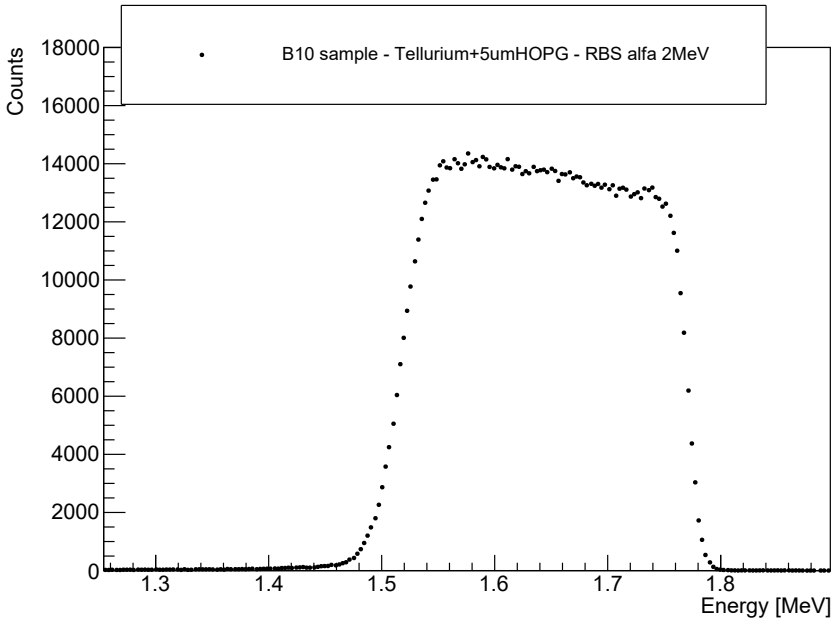

FIGURE 6.18: RBS spectrum of the target system B10, measured with a 2 MeV alpha beam, detected at 160° degree. The only contribution of the target deposition can be observed.

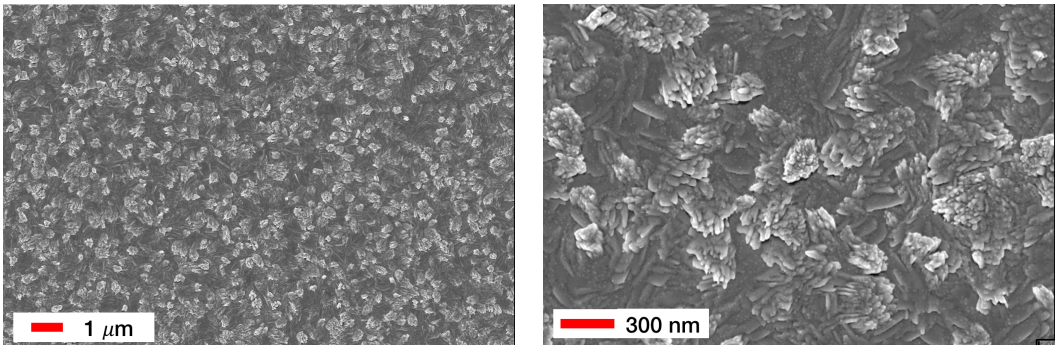

FIGURE 6.19: FESEM images of the sample B10, acquired with magnification 25k and 100k.

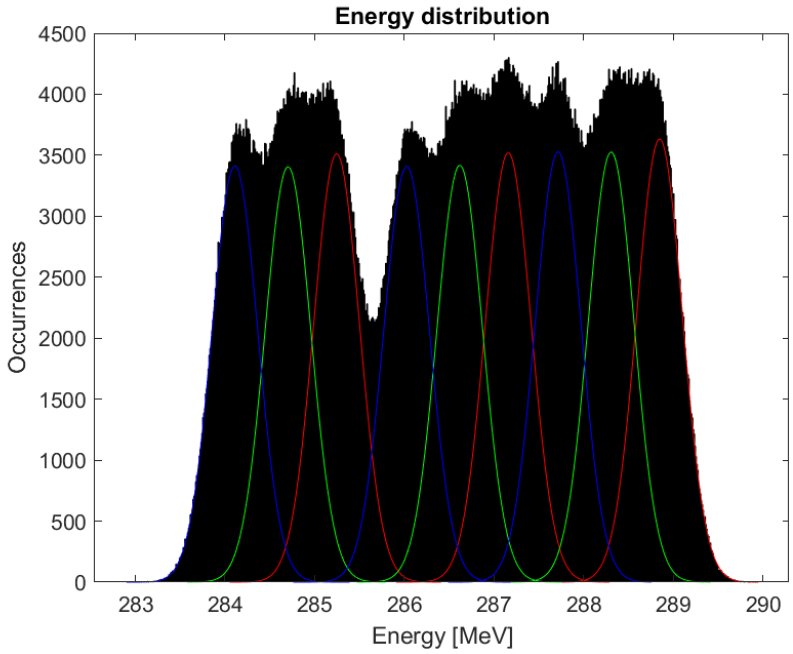

FIGURE 6.20: Energy distribution of the ejectiles of the DCE reaction $^{130}Te(^{20}Ne,^{20}O)^{130}Xe$, using as target system the prototype B10.

Monte Carlo simulation

Figure 6.20 shows the energy distribution of the ^{20}O nuclei coming out from the DCE reaction $^{130}Te(^{20}Ne,^{20}O)^{130}Xe$. The target system prototype B10 has been hypotized as target system participating to the DCE reactions.
Again, as for the Monte Carlo output related to the sample A14, the discrimination between the different peaks is not possible for the most of the energy levels.
To get a better results, a 2 μm thick substrate must be used, as shown in the following.

6.2.4 Target System C4

The NUMEN target prototype C4 has been deposited on a nominally 2 μm thick HOPG. Again, the HOPG was not heated, and no buffer was required.

Alpha Particle Transmission results

Figure 6.21 shows the APT results related to the C4 prototype. Again, the black energy spectrum has been acquired before the target deposition, while the orange spectrum must be related to the entire target system.
The substrate resulted to be 1.285 μm thick with a non-uniformity of 10%. The target deposition is instead 435 nm with a non-uniformity of 1%.

Rutherford Backscattering results

Figure 6.22 shows the RBS analysis performed on C4. Again, the measurements have been performed with a 2 MeV alpha beam, detected at 160° degree.

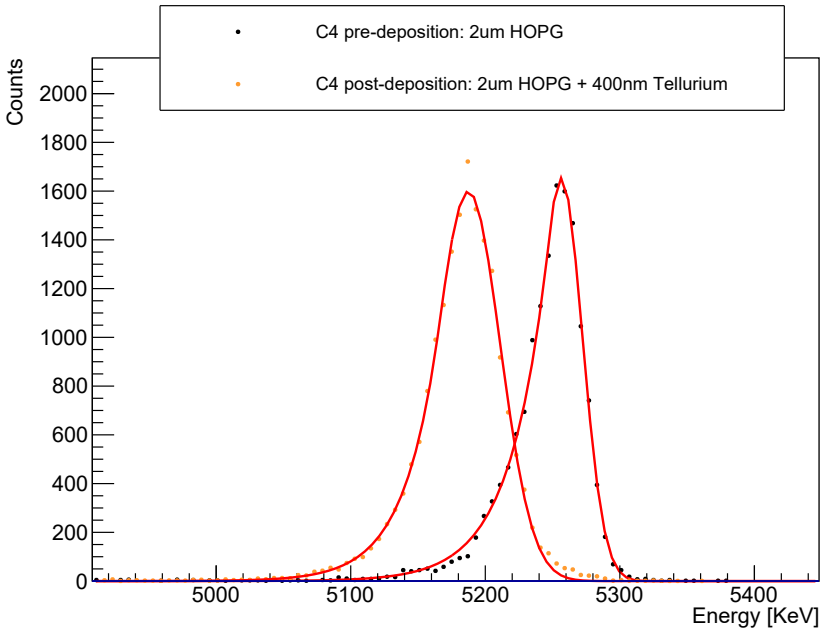

FIGURE 6.21: APT spectra acquired with the only C4 substrate (2 μm HOPG) and after the deposition with the whole target system (Tellurium deposition and HOPG substrate). Crystal Ball function fits of the two peaks are also shown, in red.

The average thickness deduced by the spectrum analysis is 420 nm; the agreement with the APT result is within the 4%.

Field Emission Scanning Electron Microscopy results

Figure 6.23 shows two FESEM images of the microscopy analysis performed on the sample C4. It can be observed that also performing the deposition on the thinner graphite, the superficial uniformity of the deposition is preserved.

Monte Carlo simulation

The Monte Carlo results related to the target system prototype C4 are reported in the energy spectrum of figure 6.24.
Now the energy resolution requirements are fully fulfilled, since the central part of each gaussian is clearly distinguishable from the near peaks.
This good result is allowed by the very low target thickness non-uniformity, here only 1%, but also to the low thickness of the HOPG substrate, here less than 1.5 μm. Ideally a very thin substrate should be crucial to get a good energy resolution, but 1 μm thick HOPG sheets are very hard to find on the market and also very fragile.

6.2.5 Conclusions on Tellurium target system prototypes

From the performed research on the Tellurium deposition processes, it resulted that there is no necessity to use a buffer between the target layer and the substrate [94]. Also the substrate heating has not a significant influence.
The deposition thickness uniformities of the produced prototypes are encouraging, but from the point of view of the energy resolution the use of a very thin (lower than 2 μm, if possible) HOPG substrate is crucial.

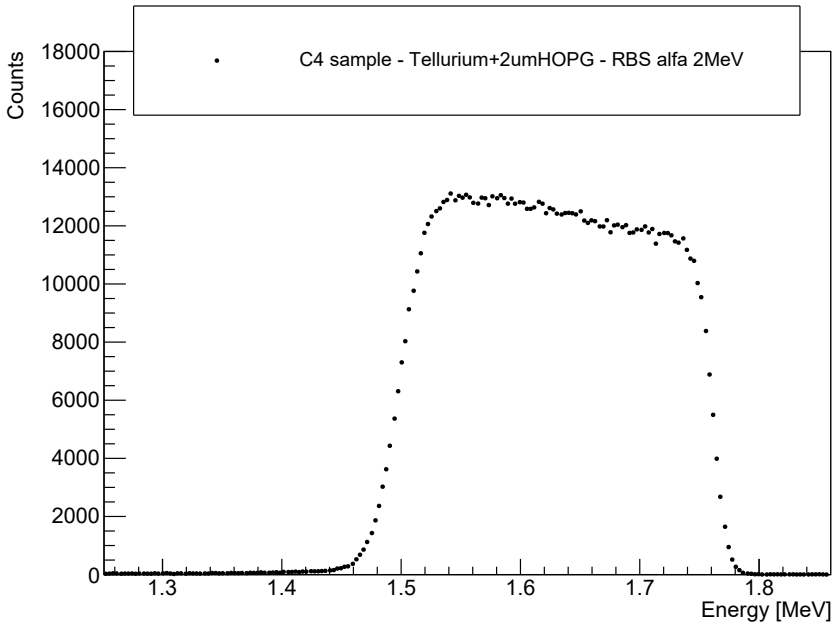

FIGURE 6.22: RBS spectrum of the target system C4, measured with a 2 MeV alpha beam, detected at 160° degree. The only contribution of the target deposition can be observed.

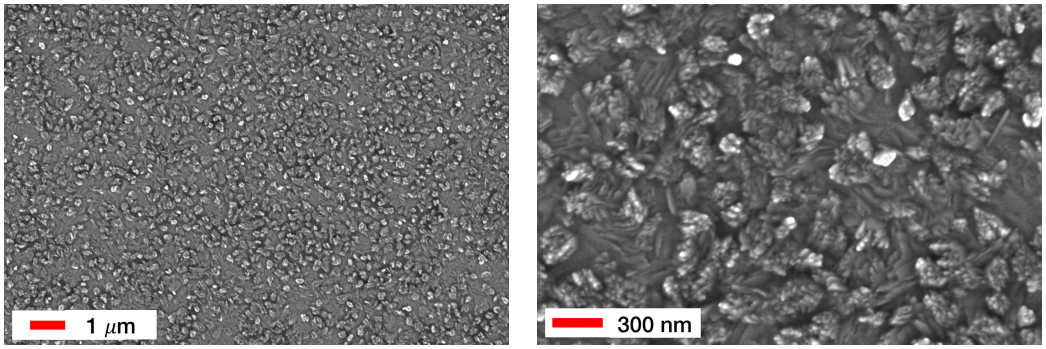

FIGURE 6.23: FESEM images of the sample C4, acquired with magnification 25k and 100k.

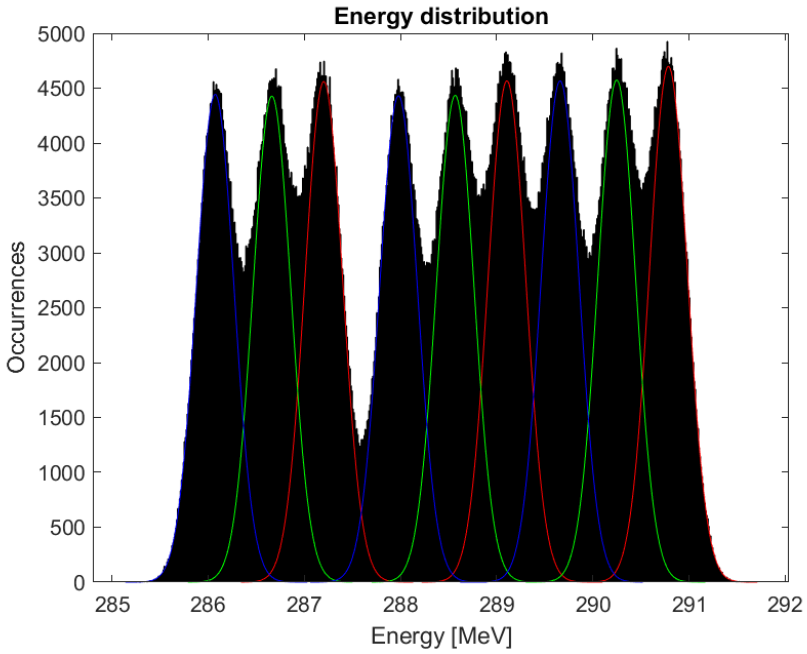

FIGURE 6.24: Energy distribution of the ejectiles of the DCE reaction $^{130}Te(^{20}Ne,^{20}O)^{130}Xe$, using as target system the prototype C4.

6.3 Germanium target systems

Germanium targets are required for the DCE research related to the reaction $^{76}Ge(^{20}Ne,^{20}O)^{76}Se$, together with its competing channels.
In the past two years, several Germanium deposition campaigns have been performed, to found out the best parameters to get a uniform target deposition layer. We found out that this element has a deposition behaviour very similar to the Tellurium one: by depositing Germanium in different evaporation conditions, the best solution turns out to be the simplest process, without substrate heating or buffer.
In the following, the most significant results will be shown, as it has been done for Tin and Tellurium.

6.3.1 Deposition campaigns

Table 6.3 reports all the deposition trials performed with Germanium. Since the Germanium study began after the research on the Tellurium deposition, we started with room temperature evaporations. The first results were promising, so we continued to optimize the Germanium target production at room temperature. Also the buffer is probably not necessary, as the characterization of the first prototypes produced without Chromium layer shows.

6.3.2 Target System A25

The A25 prototype of Germanium target system represents one of the first trial of Germanium deposition on HOPG. At that time, the evaluations on the energy resolution requirements allowed to use a target 600 nm thick, so this deposition thickness has been asked to the Trustech company. In the following, as it will be shown, the requirements on the energy resolution become more stringent, so the target thickness

Nominal target thickness [nm]	Nominal substrate thickness [μm]	Substrate temperature	Buffer	Number of trials
600	10 μm	Room temperature	Chromium (10 nm)	3
600	5 μm	Room temperature	Chromium (10 nm)	2
600	2 μm	Room temperature	Chromium (10 nm)	2
400	5 μm	Room temperature	Chromium (10 nm)	1
400	2 μm	Room temperature	Chromium (10 nm)	1
350	5 μm	Room temperature	NO	2
350	2 μm	Room temperature	NO	2

TABLE 6.3: Deposition campaigns of Germanium target system prototypes.

was reduced to 350 nm to minimize energy dispersion and straggling effects.
A25 has been deposited on a 10 μm thick HOPG, after the evaporation on the substrate of a thin layer of Chromium as buffer. The HOPG substrate was not heated.
In the following, the characterization results will be reported, as for Tin and Tellurium.

Alpha Particle Transmission results

A25 underwent APT analysis, before the deposition and once the target has been deposited. Figure 6.25 shows this study, where the black energy spectrum is related to the first acquisition and the orange one is related to the second APT acquisition, after the target deposition.
From the black spectrum, the HOPG features has been extrapolated: it resulted to be 10.120 μm thick, with a non-uniformity of 2%.
The orange spectrum has been used, in comparison with the black one, to analyze the Germanium target. To get the target features, also the Chromium buffer has been considered, which thickness has been evaluated by RBS as 10 nm. In the end, the target layer resulted to be 530 nm thick, with a non-uniformity of 16%.

Rutherford Backscattering results

Figure 6.26 reports the RBS spectrum measured with an alpha beam of 2 MeV detected at 160° degree. The contribution on the left of the main target contribution is related to the Chromium buffer.
From the study of the left edge of the main contribution, the target average thickness can be extrapolated, being 535 nm. The agreement of this value with the APT thickness evaluation is within the 1%.
Once the target average thickness has been evaluated, the left peak can be used to establish the average Chromium buffer thickness. This resulted to be 10 nm.
The RBS technique is very important not only as validation technique for the APT thickness results, but also in the context of the buffer evaluation. The RBS estimation of the average thickness of the Chromium buffer is fundamental to extrapolate the correct target thickness in the study of the APT energy spectra.

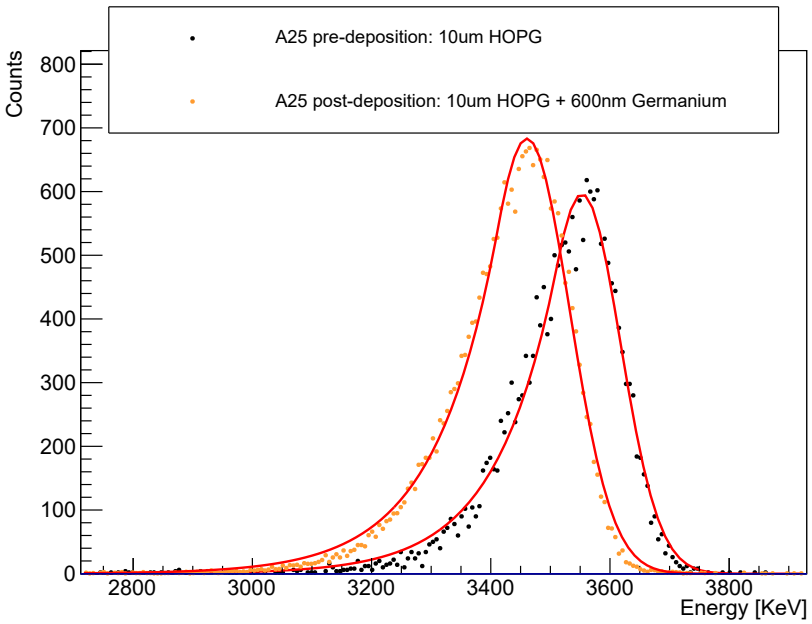

FIGURE 6.25: APT spectra acquired with the only A25 substrate (10 μm HOPG) and after the deposition with the whole target system (Germanium deposition and HOPG substrate). Crystal Ball function fits of the two peaks are also shown, in red.

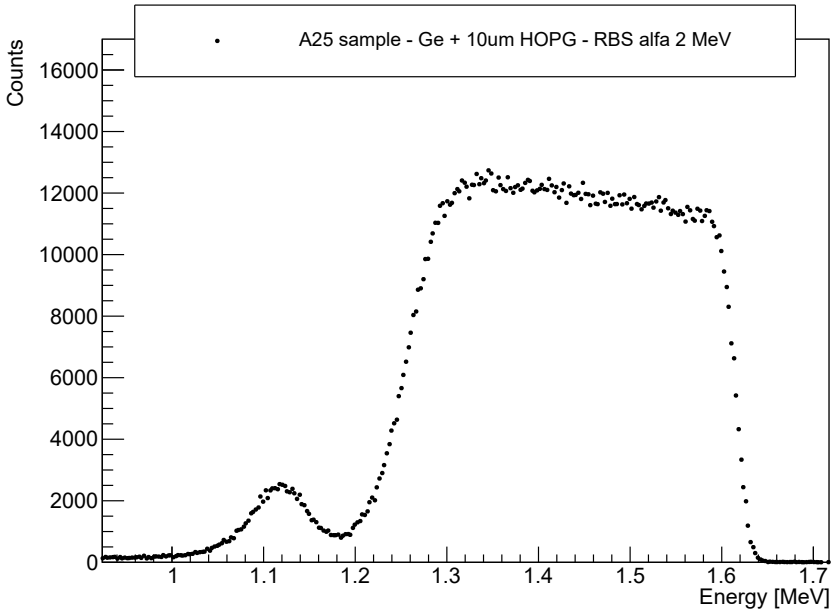

FIGURE 6.26: RBS spectrum of the target system A25, measured with a 2 MeV alpha beam, detected at 160° degree. The peak on the left of the target contribution is related to the Chromium buffer.

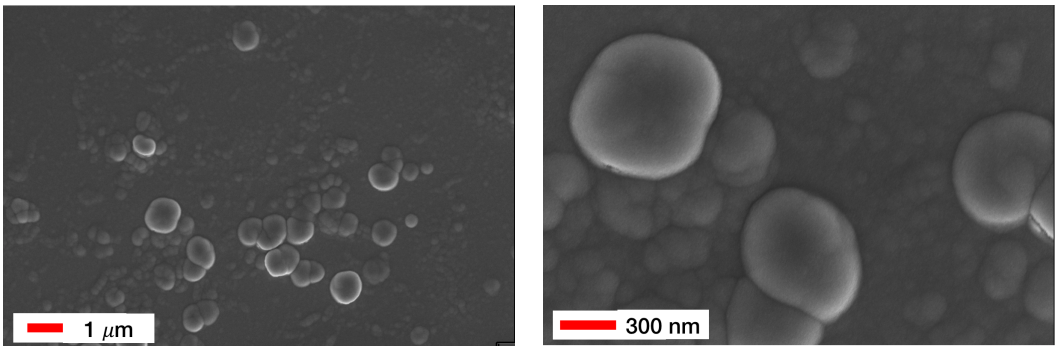

FIGURE 6.27: FESEM images of the sample A25, acquired with magnification 25k and 100k.

Field Emission Scanning Electron Microscopy results

The FESEM analysis has not been performed on sample A25. Figure 6.27 shows the FESEM analysis of another sample, named GE10, different from A25 but deposited in the same deposition. The GE10 substrate is the HOPG 10 μm thick, as the one of A25. Therefore, the FESEM images acquired on the sample GE10 can be reasonably used as analogous of the A25 FESEM analysis.
The deposition surface is flat, with the exception of some Germanium spheres, less than 1 μm in diameter, that lye on the flat deposition layer. From the higher magnification image, it can be hypotized that the flat deposition layer is, in turn, composed of many smaller spheres that joined together.

Monte Carlo simulation

Figure 6.28 shows the evaluation of the energy resolution achieved by using the target system A25. Again, it can be observed that the discrimination among the peaks is not easy, in particular between the red ones and the green ones (that correspond to target daughters respectively in ground states and first excited levels).

6.3.3 Target System B22

The target system named B22 is a Germanium deposition, asked as 350 nm, deposited on a 5 μm thick HOPG substrate. The substrate was not heated during the deposition process. No buffer has been used.

Alpha Particle Transmission results

Figure 6.29 shows the energy spectra of the transmitted alpha through the only substrate (black peak) and through the entire target system (orange peak).
As usually, the two spectra have been compared to perform the thickness evaluations on the HOPG substrate and on the Germanium target.
The substrate resulted to be 4.335 μm thick, with non-uniformity of 2%.
The target layer is instead 405 nm, with a non-uniformity of 16%.

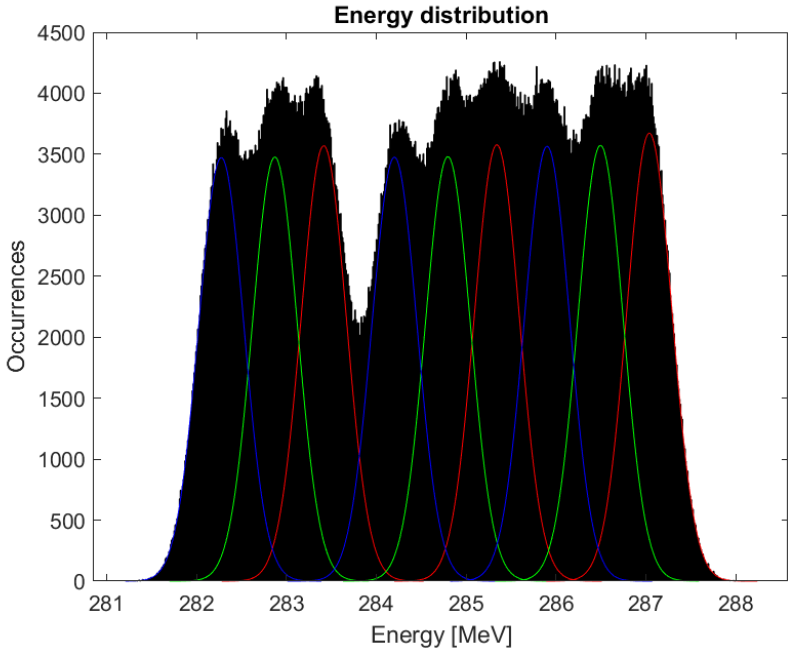

FIGURE 6.28: Energy distribution of the ^{20}O ejectiles of the DCE reaction $^{76}Ge(^{20}Ne,^{20}O)^{76}Se$, using as target system the prototype A25.

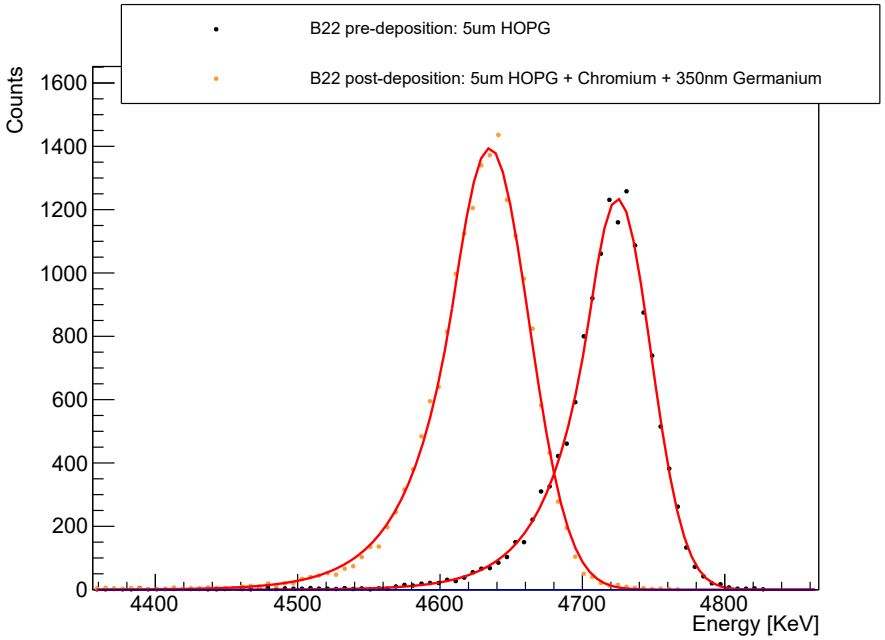

FIGURE 6.29: Black spectrum is related to the only substrate (5 μm thick HOPG), while the orange spectrum is related to the entire target system. Crystal Ball function fits of the two peaks are also shown, in red.

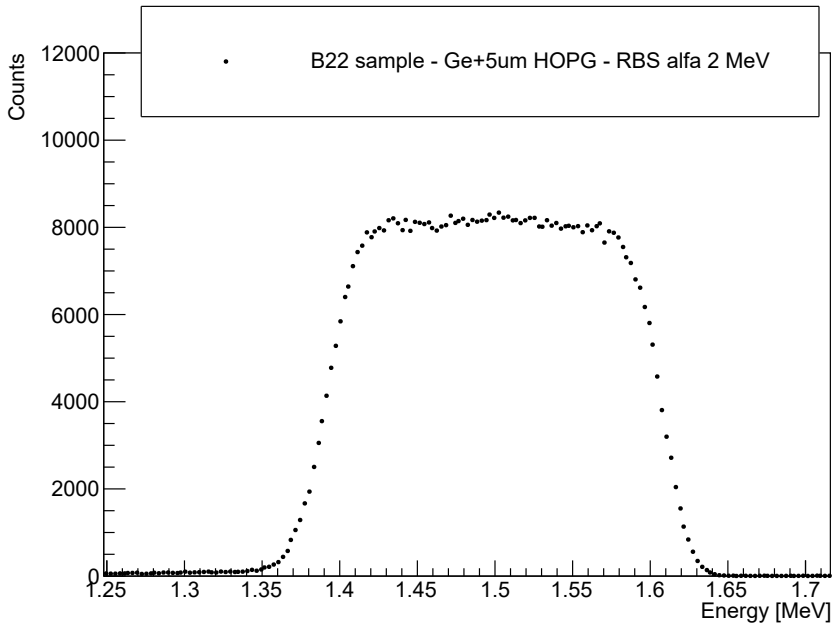

FIGURE 6.30: RBS spectrum of the target system B22, measured with a 2 MeV alpha beam, detected at 160° degree.

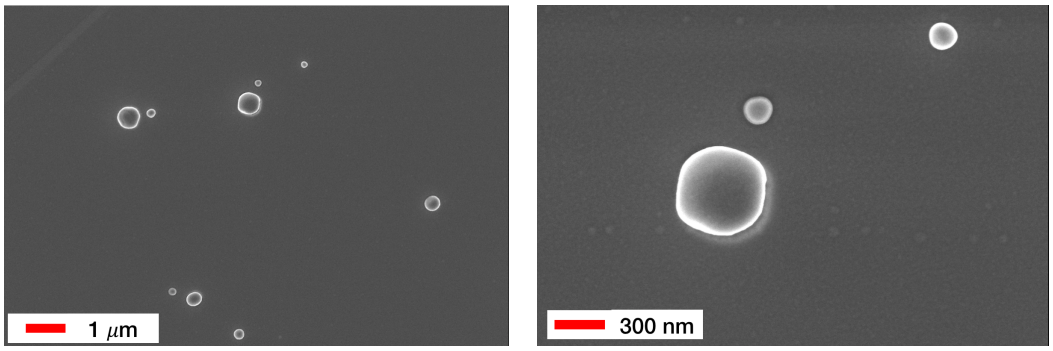

FIGURE 6.31: FESEM images of the sample B22, acquired with magnification 25k and 100k.

Rutherford Backscattering results

Figure 6.30 is the RBS spectrum acquired on the target system prototype B22, by detecting an alpha beam of 2 MeV when backscattered at 160°.
With the usual analysis procedure, the average thickness of the Germanium layer resulted to be 385 nm; the agreement with the APT measurement is within 5%.

Field Emission Scanning Electron Microscopy results

The superficial non-uniformity of the Germanium deposition can be appreciated by observing the FESEM images at different magnifications in figure 6.31. The deposition seems flat and uniform, with some little spheres with diameter of around half micrometer. Anyway, the number of Germanium spheres seem lower than the one appreciable in FESEM images of the target A25, deposited with buffer (see 6.27).

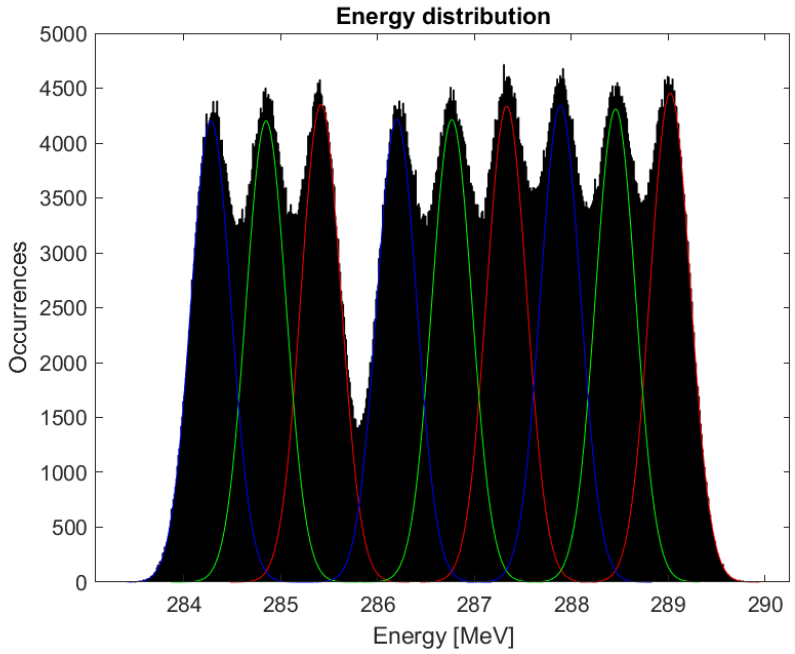

FIGURE 6.32: Energy distribution of the ^{20}O ejectiles of the DCE reaction $^{76}Ge(^{20}Ne,^{20}O)^{76}Se$, using as target system the prototype B22.

Monte Carlo simulation

Figure 6.32 reports the energy distribution of the oxygen nuclei ejectiles of the reaction $^{76}Ge(^{20}Ne,^{20}O)^{76}Se$, assuming as target system the sample B22.
The Monte Carlo output is promising if observing the distance between the energy levels peaks, that now are well distinguishable. This result, better if compared to the A25 one, can be referred to the thinner graphite substrate and to the thinner target layer (fact that minimizes both energy straggling and dispersion effects).

6.3.4 Target System C11

The Germanium target system prototype C11 has a 400 nm deposition on a 2 μm thick HOPG. A Chromium buffer has been evaporated on the substrate before the target deposition. The substrate was not heated during the deposition process.

Alpha Particle Transmission results

Figure 6.33 shows the APT results on the prototype C11. From the usual data analysis, the substrate resulted to be 1.845 μm thick, with a non-uniformity of 4%. Considering a buffer of 10 nm (evaluated by RBS measurements), the target layer resulted to be 350 nm thick, with a non-uniformity of 13%.

Rutherford Backscattering results

Figure 6.34 reports the RBS study performed on the sample C11. Again, an alpha beam of 2 MeV has been used, backscattered at 160°.
Both the target and buffer contributions can be distinguished in the spectrum. The

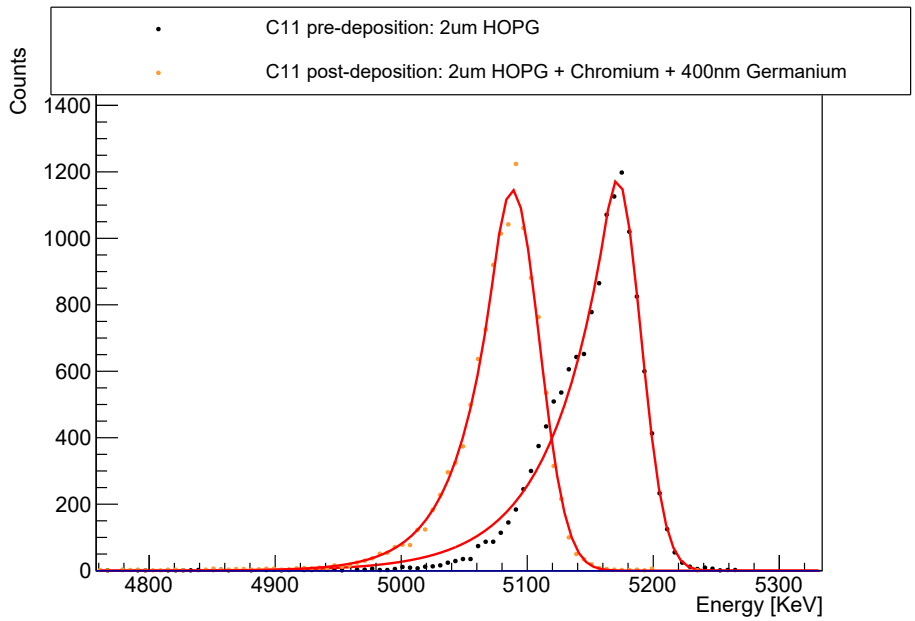

FIGURE 6.33: Black spectrum is related to the only substrate (2 μm thick HOPG), while the orange spectrum is related to the entire target system. Crystal Ball function fits of the two peaks are also shown, in red.

target average thickness, evaluated from the left edge of the spectrum main contribution, is 380 nm (being the agreement with APT thickness evaluation within the 6%). The thickness of the Chromium buffer resulted instead to be around 10 nm.

Field Emission Scanning Electron Microscopy results

Images of figure 6.35 shows again a good superficial uniformity of the Germanium deposition. The deposition seems quite flat, with the same rare spheres observed in the FESEM images of B22.

Monte Carlo simulation

Figure 6.36 shows that the target prototype C11 is an ideal solution to preserve the overall energy resolution in the ejectiles measurements. This good result is due to the good thickness uniformity of the target deposition, together with a substrate thinner than 2 μm.

6.3.5 Conclusions on Germanium target system prototypes

The same observations made for the Tellurium deposition process can be here repeated.
The Chromium buffer seems to be not really relevant to enhance the target deposition uniformity, as the substrate heating. For this reason, the found solution is to perform the Germanium depositions at room temperature, without buffer evaporation.
Concerning the energy resolution, the prototype C11 confirms that the thickness uniformity reached with the studied deposition process is good enough to fulfil the energy resolution requirements, if a thin (if possible less than 2 μm) HOPG buffer is

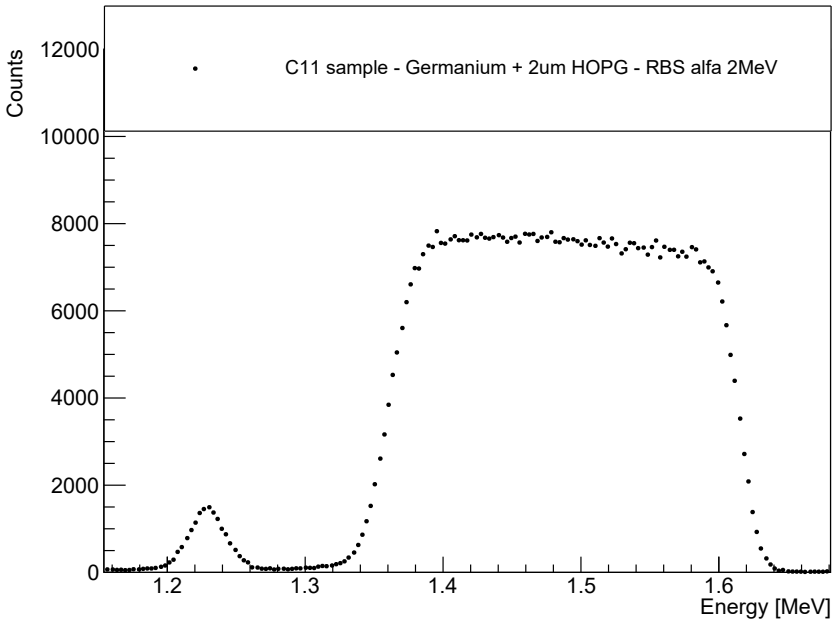

FIGURE 6.34: RBS spectrum of the target system C11, measured with a 2 MeV alpha beam, detected at 160° degree. The peak on the left of the target contribution is related to the Chromium buffer.

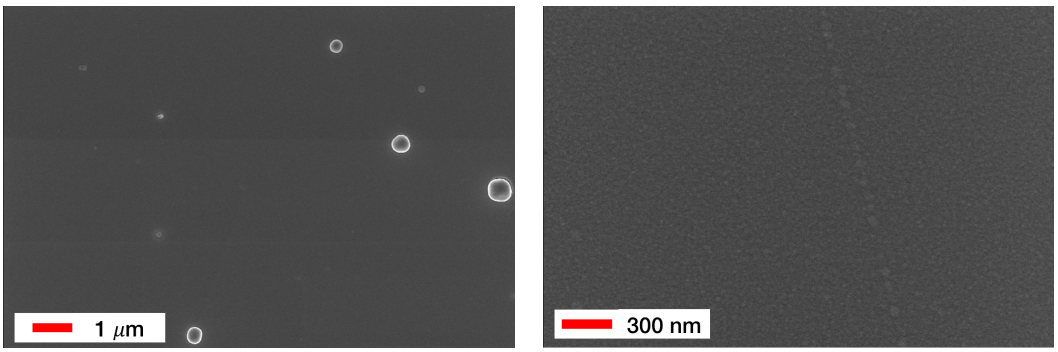

FIGURE 6.35: FESEM images of the sample C11, acquired with magnification 25k and 100k.

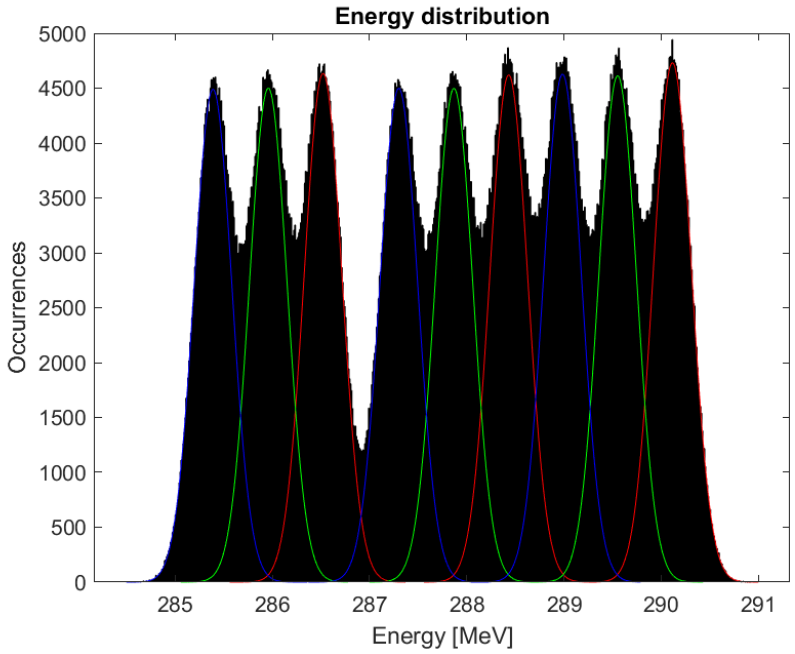

FIGURE 6.36: Energy distribution of the ^{20}O ejectiles of the DCE reaction $^{76}Ge(^{20}Ne,^{20}O)^{76}Se$, using as target system the prototype C11.

used.

Chapter 7

Results and Future Research

7.1 Main Results

This PhD research has been aimed to design a complete and efficient characterization procedure to analyse the NUMEN target systems. This study must be framed in the context of the evaluation of the Experiment energy resolution, to which different effects related to the target system contribute, as energy dispersion and straggling. The outlined characterization procedure will be used as standard procedure in the target laboratories of the NUMEN experiment, to accurately analyse the target systems of NUMEN Phase 4.
The NUMEN target system that has been designed will be used during the Phase 4 of the Experiment, when very intense ion beams will be used and therefore the targets will have to be heat resistant. The cooling system specifically designed for the NUMEN targets is based on the use of substrates made of Highly Oriented Pyrolytic Graphite that, thanks to its high in-plane thermal conductivity, can quickly transfer the heat generated by the beam from the target center to its extremities, where a cooled down frame holds the target system.
The target thickness will vary between 300 and 600 nm, depending on the isotope, while the HOPG substrate will be around 2 μm thick.
In order to evaluate the target contributions to the overall energy resolution, a Monte Carlo simulation has been implemented to estimate the capability of discrimination between DCE products exiting in different energy states.
This characterization procedure includes different analysis techniques, exploiting low energy ion beams and microscopy instruments. In particular, Rutherford Backscattering and Alpha Particle Transmission techniques have been exploited to get quantitative information on the target systems, while Field Emission Scanning Electron Microscopy and Atomic Force Microscopy, together with Energy Dispersion X-Ray measurements, have been used to qualitatively analyse the samples.
The characterization method has been experimented on the first prototypes of target systems, in particular the Tin, Tellurium and Germanium ones.
The target will be deposited on the HOPG substrate by Electron Beam Physical Vapor Deposition technique. In some cases, to facilitate the adhesion between the HOPG substrate and the target layer, a buffer will be used.
Concerning the studied target elements, the best deposition parameters have been searched.
For Tellurium and Germanium, there isn't necessity of a buffer and the substrate can be at room temperature during the target evaporation.
For the Tin deposition, the substrate must be heated at around 100° degree, even if the exact temperature value depends on the temperature reader mechanism inside the evaporator. Also a buffer is necessary to get a target deposition as uniform as possible.

This pioneering study led to the optimization of data acquisition and analysis with the different characterization techniques. Concerning the low energy ion beams techniques, specific codes have been implemented to calculate the sample thickness features starting from the ion energy distribution. These codes will be used during the NUMEN phase 4 to perform an accurate analysis of the thickness distribution of the target systems before they are submitted to the cyclotron ion beam.
The Alpha Particle Transmission technique can study both the average thickness and the thickness uniformity of target deposition and substrate, through the comparison between the analysis of the substrate alone and the analysis performed on the entire target system. The thickness non-uniformity evaluation can be achieved using an alpha particle detector with a very good energy resolution: silicon detectors can easily fulfil this requirement.
The Rutherford Backscattering technique can be used to evaluate the average thickness of each layer composing the target system, including the buffer. Moreover, it can perform the elemental analysis of the sample, revealing the elements of each layer.
The microscopy techniques, as Field Emission Scanning Electron Microscopy and Atomic Force Microscopy, can qualitatively analyse the sample surface topography, allowing a qualitative immediate evaluation of the deposition uniformity. AFM can provide qualitative estimations of the superficial thickness uniformity. With the detection of the X rays, by EDX, also the elemental analysis of the sample can be performed.
All these different type of studies have been employed to characterize the first produced NUMEN target prototypes. The Monte Carlo simulation has been used to understand if the thickness features of the prototypes are suitable to preserve a good overall energy resolution. The results show that the Tellurium and Germanium prototypes have a thickness uniformity good enough to fulfil the strict requirements on the energy resolution. Instead, the Tin depositions thickness non-uniformity is still not satisfactory, since does not allow to distinguish among the energy levels of the DCE products. More studies have to be done in this direction.

7.2 Future Research

Even if a big portion of the R&D study on the NUMEN target systems for the Phase 4 has been already done, much remains to be done.
The most has to be achieved on the deposition of the target system prototypes.
First of all, the deposition process of the Tin target must be studied in more details, to understand if a better thickness uniformity can be reached. If not, the target thickness will have to be reduced, to minimize in this way energy dispersion and straggling.
Then, the deposition processes of many other target elements have to be studied, as ^{76}Se, ^{12}C, ^{48}Ti and ^{116}Cd.
It must be also reminded that the deposition processes, after being optimized by depositing the natural isotopes, have to be repeated with the isotopes required to get the DCE reactions. This further step will require more attention to avoid wasting the costly elements.
Concerning instead the development of a complete characterization procedure suitable to study in all the details the NUMEN target system, the most important steps have been fully studied in this PhD research.

It is fundamental to know with very high precision not only the elemental composition of the target, but also its thickness and its thickness uniformity, before submitting the target system to the ion beams in DCE cross-section measurements.
Thanks to the research described in this Thesis, now the NUMEN Project can rely on a fully designed method that will provide quantitative, accurate and in some cases also redundant information of the entire target system, whose each part will be precisely characterized. Each type of the described techniques will be used to get as much as possible reliable data. The sequence of operations to characterize the targets will be followed, during the experiment, as outlined in this PhD thesis. The results obtained with each analysis tool will be compared, where and when possible, with the results obtained with the other techniques; this process will allow to reach a full 360° degree characterization of the NUMEN target systems.

In conclusion, this research will allow the NUMEN Project to understand if a produced target system is suitable for the Project aims. By choosing target systems with good thickness uniformity and whose characteristics are well know, it will be possible to guarantee a good energy resolution in the measurements of the DCE ejectile energies, by minimizing all the effects related to the target system that could bring uncertainties.
This research related to the target system, together with all the developments related to the NUMEN measurements acquisition and analysis, will be decisive to reach the NUMEN scientific goals. The measurements of the Double Charge Exchange reactions will be useful, as described in the first Chapters of this Thesis, to help the scientific community in the fascinating research of the neutrino's nature.

Appendix A

Two-bodies kinematics: massive particle scattering

A particle with mass m_1 and absolute value of the relativistic three-impulse p_i is supposed to scatter with a particle with mass m_2 that is at rest.
In the following, a reference system with the x axis along the three-impulse direction will be used. $\bar{p}_3$ and $\bar{p}_4$ are the three-impulses of the two particles after the scattering, whose masses will be m_3 and m_4. $\bar{p}_1$, $\bar{p}_3$ and $\bar{p}_4$ lie in the same plane. θ_3 and θ_4 are the angles between, respectively, $\bar{p}_3$ and $\bar{p}_4$ with the x axis. The first components of the four-impulses are called E_1, E_2, E_3 and E_4, being the respective energies.
Before using the first principle of the relativistic dynamics, it is important to remind the equations that determine the initial state as function of the masses and of the absolute value of the initial three-impulse, that are supposed as known. The four-impulses are indicated with the capital letters, while the subscripts i and f are used for the known quantities before and after the scattering.

$$\begin{aligned} E_1^2 &= m_1^2 + p_1^2 \\ E_2^2 &= m_2^2 \\ E_i^2 &= (E_1 + E_2)^2 \end{aligned} \tag{A.1}$$

The four-impulses are:

$$\begin{aligned} P_1 &= (E_1, p_1, 0, 0) \\ P_2 &= (E_2, 0, 0, 0) \\ P_i &= (E_i, p_1, 0, 0) \end{aligned} \tag{A.2}$$

where the components of the four-impulses are energies. Analogously, for the final state:

$$\begin{aligned} P_3 &= (E_3, p_3 cos\theta_3, p_3 sen\theta_3, 0) \\ P_4 &= (E_4, p_4 cos\theta_4, p_4 sen\theta_4, 0) \\ P_f &= (E_f, p_3 cos\theta_3 + p_4 cos\theta_4, p_3 sen\theta_3 + p_4 sen\theta_4, 0) \end{aligned} \tag{A.3}$$

Remarks about the coordinates
Equations A.1 and A.2 are written in the Cartesian reference system. Equations of A.3 are using the spherical coordinates and the azimuthal angle is taken zero, due to the planar feature of the scattering. Therefore both θ_3 and θ_4 range from 0 to π.

Now, the first principle of the relativistic dynamics can be used for the equivalence $P_i = P_f$ of the initial and final total four-impulses:

$$\begin{aligned} E_i = E_3 + E_4 = \sqrt{m_3^2 + p_3^2} + \sqrt{m_4^2 + p_4^2} \\ p_1 = p_3 cos\theta_3 + p_4 cos\theta_4 \\ p_3 sen\theta_3 = p_4 sen\theta_4 \end{aligned} \tag{A.4}$$

From the third equation of A.4 it can be observed that θ_3 and θ_4 have opposite signs. After some algebraic passages:

$$\begin{aligned} (E_i - \sqrt{m_3^2 + p_3^2})^2 = m_4^2 + p_4^2 \\ (p_1 - p_3 cos\theta_3)^2 = p_4^2 cos^2\theta_4 \\ p_3^2 sen^2\theta_3 = p_4^2 sen^2\theta_4 \end{aligned} \tag{A.5}$$

$$\begin{aligned} E_i^2 + m_3^2 + p_3^2 - 2E_i\sqrt{m_3^2 + p_3^2} - m_4^2 = p_4^2 \\ p_1^2 - 2p_1 p_3 cos\theta_3 + p_3^2 = p_4^2 \\ p_3 sen\theta_3 = p_4 sen\theta_4 \end{aligned} \tag{A.6}$$

$$\begin{aligned} E_i^2 + m_3^2 + p_3^2 - 2E_i\sqrt{m_3^2 + p_3^2} - m_4^2 = p_1^2 - 2p_1 p_3 cos\theta_3 + p_3^2 \\ p_4 = \sqrt{p_1^2 - 2p_1 p_3 cos\theta_3 + p_3^2} \\ p_3 sen\theta_3 = p_4 sen\theta_4 \end{aligned} \tag{A.7}$$

$$\begin{aligned} E_i^2 + m_3^2 - 2E_i\sqrt{m_3^2 + p_3^2} - m_4^2 = p_1^2 - 2p_1 p_3 cos\theta_3 \\ p_4 = \sqrt{p_1^2 - 2p_1 p_3 cos\theta_3 + p_3^2} \\ p_3 sen\theta_3 = p_4 sen\theta_4 \end{aligned} \tag{A.8}$$

$$\begin{aligned} \frac{E_i^2 + m_3^2 - m_4^2 - p_1^2}{2E_i} + \frac{2p_1}{2E_i} p_3 cos\theta_3 = \sqrt{m_3^2 + p_3^2} \\ p_4 = \sqrt{p_1^2 - 2p_1 p_3 cos\theta_3 + p_3^2} \\ p_3 = sen\theta_3 = p_4 sen\theta_4 \end{aligned} \tag{A.9}$$

Defining:

$$\begin{aligned} d \equiv \frac{E_i^2 + m_3^2 - p_1^2 - m_4^2}{2E_i} \\ \beta_i \equiv \frac{p_i}{E_i} \end{aligned} \tag{A.10}$$

The equations of A.9 become:

$$\begin{aligned} d + \beta_i p_3 cos\theta_3 &= \sqrt{m_3^2 + p_3^2} \\ p_4 &= \sqrt{p_1^2 - 2p_1 p_3 cos\theta_3 + p_3^2} \\ p_3 sen\theta_3 &= p_4 sen\theta_4 \end{aligned} \tag{A.11}$$

$$\begin{aligned} p_3^2(1 - \beta_i^2 cos^2\theta_3) - 2d\beta_i cos\theta_3 \cdot p_3 + m_3^2 - d^2 = 0 \\ p_4 = \sqrt{p_1^2 - 2p_1 p_3 cos\theta_3 + p_3^2} \\ p_3 sen\theta_3 = p_4 sen\theta_4 \end{aligned} \tag{A.12}$$

Defining:

$$\begin{aligned} c &\equiv m_3^2 - d^2 \\ b &\equiv d\beta_i cos\theta_3 \\ a &\equiv 1 - \beta_i^2 cos^2\theta_3 \geq 0 \end{aligned} \tag{A.13}$$

The final result is:

$$\begin{aligned} a p_3^2 - 2b p_3 + c = 0 \\ p_4 = \sqrt{p_1^2 - 2p_1 p_3 cos\theta_3 + p_3^2} \\ p_3 sen\theta_3 = p_4 sen\theta_4 \end{aligned} \tag{A.14}$$

$$\begin{aligned} p_3 &= \frac{b \pm \sqrt{b^2 - ac}}{a} \\ p_4 &= \sqrt{p_1^2 - 2p_1 p_3 cos\theta_3 + p_3^2} \\ \theta_4 &= arcsen\left(\frac{p_3}{p_4} sen\theta_3\right) \end{aligned} \tag{A.15}$$

A.1 Discussion of the solution

From the first of the equations of A.15, it is possible to observe that there are two possible values for p_3, and consequently for p_4 and θ_4, provided that both solutions give p_3 positive.
The discriminant of the second of the equations of A.15 is always positive:

$$p_1^2 - 2p_1 p_3 cos\theta_3 + p_3^2 = (p_1 - p_3)^2 + 2p_1 p_3(1 - cos\theta_3) \geq 0 \tag{A.16}$$

Therefore a value of p_4 exists for each positive value of p_3.
Concerning the discriminant of the first of the equations of A.15, it is possible to observe that there are two cases:
Case 1: $c < 0$
Since $a > 0$ (see A.14), the discriminant is positive and greater than b^2: therefore

the negative solution of p_3 is not acceptable. There is always one and only one kinematical solution of the reaction, dependent on the θ_3 angle, the initial masses and impulse and final masses.
Case 2: $c > 0$
In this case there is the possibility of a negative discriminant, which excludes the existence of any solution for the reaction. To better discuss this case, it is useful to write explicitly the discriminant as a function of all the parameters and impose it be positive:

$$b^2 - ac = m_3^2 \cdot \beta_i^2 \cdot cos^2\theta_3 - (m_3^2 - d^2) \geq 0 \tag{A.17}$$

$$cos^2\theta_3 \geq \frac{m_3^2 - d^2}{m_3^2 \cdot \beta_i^2} \tag{A.18}$$

$$cos\theta_3^{max} = \sqrt{\frac{m_3^2 - d^2}{m_3^2 \cdot \beta_i^2}} \tag{A.19}$$

$$\theta_3^{max} = arccos\sqrt{\frac{m_3^2 - d^2}{m_3^2 \cdot \beta_i^2}} \tag{A.20}$$

Therefore in this case there is a maximum angle θ_3^{max} over which there is no solution for the reaction. Below θ_3^{max}, there are two solutions in p_3, p_4 and θ_4, which correspond to the same exit angle θ_3 of the mass m_3.
It must be remarked that p_4 depends on both the angle θ_3 and the initial momentum p_3.

$$\begin{aligned} p_3(+) &= \frac{b + \sqrt{b^2 - ac}}{a} \\ p_4(+) &= \sqrt{p_1^2 - 2p_1p_3(+)cos\theta_3 + p_3^2(+)} \\ \theta_4(+) &= arcsen\left(\frac{p_3(+)}{p_4(+)}sen\theta_3\right) \end{aligned} \tag{A.21}$$

$$\begin{aligned} p_3(-) &= \frac{b - \sqrt{b^2 - ac}}{a} \\ p_4(-) &= \sqrt{p_1^2 - 2p_1p_3(-)cos\theta_3 + p_3^2(-)} \\ \theta_4(-) &= arcsen\left(\frac{p_3(-)}{p_4(-)}sen\theta_3\right) \end{aligned} \tag{A.22}$$

Bibliography

[1] Chung Wook Kim, "Neutrinos in Physics and Astrophysics", Routledge, 1993.

[2] Macioce, V., "Ecco la scoperta che mette in crisi Einstein", IlGiornale.it, 22-09-2011. Web, 24-08-2020. https://www.ilgiornale.it/news/ecco-scoperta-che-mette-crisi-einstein.html.

[3] Pontecorvo, B., "Mesonium and anti-mesonium", Zh. Eksp. Teor. Fiz., vol. 33, pp. 549-551, 1957.

[4] Balantekin, A. B., et al., "Neutrino oscillations", Progress in Particle and Nuclear Physics, 71, 150-161, 2013.

[5] Stoica, S., et al., "New Calculations phase space factors involved in double-β decay", Phys. Rev. C 88, 037303, 2013.

[6] Otsuka, T., et al., "Shell model description of interacting bosons", Phys. Lett. B, 76(2), 139-143, 1978.

[7] Vogel, P., "Nuclear structure and double beta decay", J. Phys. G: Nucl. Part. Phys., 39 124002, 2012.

[8] Fukuda, S. et al., "The Super-Kamiokande detector", Nucl. Inst. and Meth. in Phys. Res. A, 501 (2-3): 418-462, 2003.

[9] Ackermann, K.-H. et al., "The GERDA experiment for the search of $0\nu\beta\beta$ decay in ^{76}Ge", Eur. Phys. J. C, 73:2330, 2013.

[10] Ardito, R. et al, "CUORE: A Cryogenic Underground Observatory for Rare Events", arXiv:hep-ex/0501010, 2005.

[11] GERDA Collaboration, "The Physics of GERDA", 2010. Web, 24-08-2020. https://www.mpi-hd.mpg.de/gerda/physics.html.

[12] Cuore Collaboration, "detectors", cuore.lngs.it, 2020. Web, 24-08-2020. https://cuore.lngs.infn.it/en/about/detectors.

[13] Lenske, H., et al., "Theory of single-charge exchange heavy-ion reactions", Phys. Rev. C 98, 044620, 2018.

[14] Cappuzzello, F., et al., "The NUMEN project: NUclear Matrix Elements for Neutrinoless double beta decay", Eur. Phys. Jour.A, 54(5), 2018.

[15] Barea, J., et al., "Limits on Neutrino Masses from Neutrinoless Double-β Decay", Phys, Rev. Lett., 109(4), 2012.

[16] Lutostansky, Yu. S., "Giant Gamow-Teller Resonance: 40 Years after the Prediction" Physics of Atomic Nuclei, 74(8), 1176-1188, 2010.

[17] Auerbach, N., et al., "Pion double charge exchange and the nuclear shell model", Phys. Rev. Lett., 59(10), 1076-1079, 1987.

[18] Mordechai, S., et al., "Giant dipole resonances built on isobaric analog states in pion double charge exchange", Phys. Rev. Lett., 60(5), 408-411, 1988.

[19] Auerbach, N., "Double Charge Exchange Reactions and Double Beta Decay", Jour. of Phys.: Conf. Ser., 1023, 012032, 2018.

[20] Brendel, C., et al., "Quasi-elastic nucleon transfer and single charge exchange in $^{48}Ti + ^{42}Ca$ collisions", Nucl. Phys. A, 477(1), 162-188, 1988.

[21] Lenske, H., et al., "Reaction mechanism of heavy-ion charge-exchange scattering at intermediate energies", Phys. Rev. Lett., 62(13), 1457-1460, 1998.

[22] Bohlen, H. G. et al., "The mechanism of the $(^{12}C,^{12}N)$ charge exchange reaction on ^{12}C between 30 and 100 MeV/u", Nucl. Phys. A, 488, 89-94, 1988.

[23] Annakkage, T. et al., "Isovector giant resonances in ^{6}He, ^{12}B, ^{90}Y, ^{120}In and ^{208}Tl observed in the $(^{7}Li,^{7}Be)$ charge-exchange reaction", Nucl. Phys. A, 648(1-2), 3-44, 1999.

[24] Von Oertzen, W., "Excitation of isovector modes in heavy ion induced charge exchange reactions", Nucl. Phys. A, 482(1-2), 357-372., 1988.

[25] Naulin, F. et al., "Mass of ^{18}C from the double-charge-exchange reaction $^{48}Ca(^{18}O,^{18}C)^{48}Ti$, Physical Review C, 25(2), 1074-1075, 1982.

[26] Blomgren, J. et al., "Search for double Gamow-Teller strength by heavy-ion double charge exchange", Phys. Lett. B, 363, 34-38, 1995.

[27] Drake, D. M. et al., "Exotic Heavy-Ion reactions on ^{40}Ca: $(^{14}C,^{14}O)$ double charge exchange and $(^{14}C,^{15}O)$ rearrangement transfer", Phys. Rev. Lett., 45 22, 1765-1769, 1980.

[28] Kisamori, K. et al., "Candidate resonant tetraneutron state populated by the $^{4}He(^{8}He,^{8}Be)$ reaction", Phys. Rev. Lett., 116, 052501, 2016.

[29] Sagawa, H. et Uesaka, T., "Sum rule study for double Gamow-Teller states", Phys. Rev. C, 94, 064325, 2016.

[30] Cappuzzello, F. et al., "Heavy-ion double charge exchange reactions: a tool towards $0\nu\beta\beta$ nuclear matrix elements", Eur. Phys. J. A, 51 11, 145, 2015.

[31] Thompson, I. J., "Coupled Reaction Channels Calculations in Nuclear Physics", Computer Physics Reports, vol. 7, 4, 167-212, 1988.

[32] Frank, A., et al., "Commutator algebra for the microscopic interacting boson model with nondegenerate orbits", Phys. Rev. C, 26(4), 1661-1666, 1982.

[33] Otsuka, T., et al., "Nuclear shell model and interacting bosons", Nucl. Phys. A, 309(1-2), 1-33, 1978.

[34] Barea, J., et al., "Nuclear matrix elements for double-β decay", Phys. Rev. C, 87(1), 2013.

[35] NUMEN TDR, submitted.

[36] Rifuggiato, D., et al., Proc. Int. Conference on Cyclotron and their Applications, 2013. https://accelconf.web.cern.ch/Cyclotrons2013/papers/moppt011.pdf

[37] Cappuzzello, F., et al., "The MAGNEX spectrometer: Results and perspectives", Eur. Phys. J. A 52, 167, 2016.

[38] Cappuzzello, F., et al, "Measuring the ions momentum vector with a large acceptance magnetic spectrometer", Nucl. Instr. and Meth. in Phys. Res. A, 638(1), 74-82, 2011.

[39] The Editors of Encyclopaedia Britannica, "Bessel function", Britannica.com, 1998. Web, 2020-08-21. https://www.britannica.com/science/Bessel-function.

[40] Calabrese, S., et al., "First Measurement of the ^{116}Cd(^{20}Ne,^{20}O)^{116}Sn Reaction at 15 A MeV", Acta Physica Polonica B, 49, 275, 2018.

[41] Spatafora, A., et al, "$^{20}Ne + ^{76}Ge$ elastic and inelastic scattering at 306 MeV", Phys. Rev. C, 100(3), 2019.

[42] Brown, K. L., et al., "Faraday-Cup Monitors for High-Energy Electron Beams", Rev. of Sc. Inst., 27(9), 696-702, 1956.

[43] Oliveira, J. R. B., et al.,"First comparison of GEANT4 hadrontherapy physics model with experimental data for a NUMEN project reaction case", Eur. Phys. J. A, 56:153, 2020.

[44] Cavallaro, M., et al., "The low-pressure focal plane detector of the MAGNEX spectrometer", Eur. Phys. Jour. A, 48(5), 2012.

[45] Calanna, A., "High-intensity extraction from the Superconducting Cyclotron at LNS-INFN", Il Nuovo Cimento C, 40, 101, 2017.

[46] Sartirana, D., et al., "Target Manipulation in Nuclear Physics Experiment with Ion Beams", in: Zeghloul S., et al., Advances in Service and Industrial Robotics, RAAD 2020, Mechanisms and Machine Science, vol 84. Springer, Cham, 2020.

[47] Cavallaro, M., et al., "The low-pressure focal plane detector of the MAGNEX spectrometer", Eur. Phys. Jour. A, 48(5), 2012.

[48] "A GEM of a Detector", CERN Courier, 1998-11-28. Web, 2020-09-08. http://cerncourier.com/cws/article/cern/27921.

[49] Ciampi, C., et al, "Nuclear fragment identification with ΔE-E telescopes exploiting silicon carbide detectors", Nucl. Instr. and Meth. in Phys. Res. A, 925, 60-69, 2019.

[50] Cirrone, G. A. P., et al., "Clinical and Research Activities at the CATANA Facility of INFN-LNS: From the Conventional Hadrontherapy to the Laser-Driven Approach", Frontiers in Oncology, 7, 2017.

[51] Oliveira, J. R. B., et al., "First comparison of GEANT4 hadrontherapy physics model with experimental data for a NUMEN project reaction case", Eur. Phys. Jour. A, 56(5), 2020.

[52] Bragg, W. H., "On the α particles of radium, and their loss of range in passing through various atoms and molecules", Phil. Mag. 10 (57): 318, 1905.

[53] Bohr, N.,"On the Theory of the Decrease of Velocity of Moving Electrified Particles on passing through Matter", Phil. Mag. 25 (145): 10, 1913.

[54] Iazzi, F., et al, "A new cooling technique for targets operating under very intense beams", WIT Transactions on Engineering Sciences, 116, 61-70, 2017.

[55] Pinna F., "Study and production of special targets for DCE reactions with $0\nu\beta\beta$-decay final states in the NUMEN Experiment", Physics Ph.D. Thesis, Politecnico di Torino, 2019.

[56] Greene, J. P., et al., "Rotating target wheel system for super-heavy element production at ATLAS", Nucl. Instr. and Meth. in Phy. Res. A, 521.1, 214-221, 2004.

[57] Santagati, G., et al, "Post-stripper study for the (^{20}Ne, ^{20}O) double charge exchange reaction at zero degrees with the MAGNEX spectrometer", Jour. of Phys. Conf. Series, 1056, 1, 2018.

[58] optigraph.eu, "Physical characteristics". Web, 2020-12-21, http://www.optigraph.eu/basics.html.

[59] Westwood, W. D., "Sputter Deposition", AVS Education Committee Book Series. 2, 2003.

[60] Harsha, K. S. S, "Principles of Physical Vapor Deposition of Thin Films", Elsevier, 2004.

[61] Seltzer, S. M. and Berger, M.J., "Energy Loss Straggling of Protons and Mesons Studies in Penetration of Charged Particles in Matter", Nuclear Science Series 39, Nat. Academy of Sciences, Washington DC, 1964.

[62] Pinna, F., et al., "Evaluation of target non-uniformity and dispersion effects on energy measurement resolution in NUMEN experiment", Phys. Scripta, 95 9, 094002, 2020.

[63] De Waele, A. T. A. M., "Basic operation of cryocoolers and relate thermal machines", Jour. of Low Temperature Physics, 164 5, 179, 2011.

[64] "COMSOL Modeling Software". COMSOL.com. Comsol, Inc.. Web, 9-11-2020. www.comsol.com

[65] Pinna, F., et al, "Tests of a cooling system for thin targets submitted to intense ions beams for the NUMEN experiment", Acta Physica Polonica B, 3, 51, 2020.

[66] Rubin, S., Passell, T. O., & Bailey, L. E., "Chemical analysis of surfaces by nuclear methods", Analytical Chemistry, 29(5), 736-743, 1957.

[67] Bird, R. C., Williams, J. S., "Ion beams for materials analysis", Elsevier, 1990.

[68] Ziegler, J. F., "Stopping of energetic light ions in elemental matter", Journal of Applied Physics 85, 1249, 1999.

[69] Fano, U., "Penetration of Protons, Alpha Particles, and Mesons", Annu. Rev. Nucl. Sci. 13, 67, 1963.

[70] Crispin, A., and Fowler, G.N., "Density Effect in the Ionization Energy Loss of Fast Charged Particles in Matter", Rev. Mod. Phys. 42, 290, 1970.

[71] Fano, U., "Studies in Penetration pf Charged Particles in Matter", Nuclear Science Report No. 39 (U.S. National Academy of Sciences, Washington DC), pp. 1-338, 1964.

[72] Bloch, F., "Bremsvermogen von Atomen mit mehreren Elektronen", Ann. Phys. 16, 285, 1933.

[73] Northcliffe, L. C., "Energy Loss and Effective Charge of Heavy Ions in Aluminum", Phys. Rev. 120, 1744, 1960.

[74] Ziegler, J. F., "SRIM: The stopping and range of ions in matter (2010)", Nucl. Inst. and Meth. in Phys. Res. B 268, 1818-1823, 2010.

[75] Biersack, J. P., and Haggmark, L. G., "A Monte Carlo computer program for the transport of energetic ions in amorphous targets", Nucl. Instr. and Meth., 174 (1-2), 257-269, 1980.

[76] Geiger, H., "The Scattering of the α-Particles by Matter", Proceedings of the Royal Society of London A. 83 (565): 492-504, 1910.

[77] "Rutherford's Nuclear World: The Story of the Discovery of the Nucleus", American Institute of Physics, history.aip.org, Web, 16-11-2020, https://history.aip.org/history/exhibits/rutherford/sections/alpha-particles-atom.html.

[78] Choppin, G. et al., "Chapter 9 - Detection and Measurement Techniques" in "Radiochemistry and Nuclear Chemistry" (Fourth Edition), Academic Press, 239-295, 2013.

[79] "SIMNRA Computer simulation of RBS, ERDA, NRA, MEIS and PIGE by Matej Mayer", IPP. Web, 10-12-2020, https://home.mpcdf.mpg.de/ mam/.

[80] "ROOT: analyzing petabytes of data, scientifically.", CERN. Web, 10-12-2020, https://root.cern/.

[81] "Pompe rotative volumetriche a doppio stadio RV", EDWARDS, edawardsvacuum.com. Web, 19-11-2020, https://www.edwardsvacuum.com/it/our-products/oil-sealed-pumps/rv-rotary-vane.

[82] "428 Radiation Detector Bias Supply", ORTEC, ortec-onlin.com. Web, 10-12-2020, https://www.ortec-online.com/products/electronics/power-supplies-and-nuclear-instrument-module-nim-bins/428.

[83] "142A/B/C Preamplifiers", ORTEC, ortec-online.com. Web, 19-11-2020, https://www.ortec-online.com/products/electronics/preamplifiers/142a-b-c.

[84] "575A Amplifier", ORTEC, ortec-online.com. Web, 18-11-2020, https://www.ortec-online.com/products/electronics/amplifiers/575a.

[85] "MAESTRO Multichannel Analyzer Emulation Software", ORTEC, ortec-online.com. Web, 18-11-2020, https://www.ortec-online.com/products/application-software/maestro-mca.

[86] Skwarnicki F., "A study of the radiative CASCADE transitions between the Upsilon-Prime and Upsilon resonances", Physics Ph.D. Thesis, DESY F31-86-02, Appendix E, 1986.

[87] Salapaka, S. and Salapaka, M.,"Scanning Probe Microscopy", IEEE Control Systems Magazine, 28 (2), 65-83, 2008.

[88] afmworkshop.com, "Measuring and Analyzing Force-Distance Curves with Atomic Force Microscopy". Web, 2020-11-22, https://www.afmworkshop.com/images/news2019/01/Measuring-and-understanding-force-distance-curves-v2.pdf.

[89] Gross, L., et al., "The Chemical Structure of a Molecule Resolved by Atomic Force Microscopy", Science, 325 (5944), 1110-1114, 2009.

[90] Ohnesorge, F., "True atomic resolution by atomic force microscopy through repulsive and attractive forces", Science, 260 (5113), 1451-6, 1993.

[91] Reimer, L., "Scanning Electron Microscopy: Physics of Image Formation and Microanalysis", Meas. Sci. Technol. 11 1826, 2000.

[92] Capirossi, V., et al., "Study, fabrication and test of a special cooling system for targets submitted to intense ion beams", NIM A, 954, 161122, 2020.

[93] Capirossi, V., et al, "Thickness and Uniformity Characterization of Thin Targets for Intense Ion Beam Experiments", Acta Phys. Polon. B 51, 661, 2020.

[94] Capirossi, V., "Characterization of first prototypes of thin targets for the NUMEN Experiment", Il Nuovo Cimento, submitted.

Acknowledgements

Sono felice di avere tante persone da ringraziare perché partecipi, anche se in modi diversi, a questa avventura del dottorato.
La fortuna professionale piú grande che ho avuto, probabilmente, é stata quella di avere incontrato il Professore Felice Iazzi come tutor in questi tre ultimi anni. Non penso di essere in grado di trovare le parole adatte per esprimere la mia gratitudine per tutto quello che mi ha insegnato (spesso forse senza neanche accorgersene, e non solo di Fisica) e per la passione per questo "strano" mestiere che mi ha trasmesso. Quindi Felice, grazie infinite, per tutto.
Ringrazio Federico Pinna, collega di target ma anche di ricerca di specialitá culinarie locali in trasferta, per tutto l'aiuto e il sostegno che mi ha sempre offerto.
Il terzo ringraziamento professionale va alla Collaborazione del Progetto NUMEN, in cui ho trovato un clima stimolante e fertile dove crescere.

Penso infine che questa pagina non sia il posto piú adatto per i ringraziamenti piú intimi alla mia piccola tribú di affetti.
Poche righe quindi per gli amici che so leggeranno questa pagina (dicendo "il resto della Tesi lo vorrei leggere ma so che non capisco niente"): ragazzi, grazie per avermi tenuto la mano per tutta la strada, senza il vostro tifo e sostegno sarebbe stato tutto infinitamente piú difficile.
Per Lorenzo, penso sempre di piú che parole non servano (a parte "Sí ora ho finito la tesi, vado a mettere a posto il caos che ho lasciato in casa").
Mamma, papá, Carlo: senza di voi, non sarei.